8-8-2014

Excitatory Post Synaptic Potentials in Dendritic Spines on Basal Dendrites of L5 Pyramidal Neurons

Erika A. Hoyos-Ramirez
University of Connecticut, hoyosramirez@uchc.edu

Excitatory Post-Synaptic Potentials in Dendritic Spines on Basal Dendrites of L5 Pyramidal Neurons

Erika Hoyos-Ramirez, PhD

University of Connecticut, 2014

Excitatory postsynaptic potentials (EPSPs) occur when the neurotransmitter glutamate binds to postsynaptic receptors located on specialized/pleomorphic structures called dendritic spines, which are attached to dendrites through spine necks. These potentials constitute the input signals that neurons must process in order to maintain proper brain function, but due to the small size of spines, direct measurement of these potentials at their site of origin has remained elusive. In this study, we combine voltage-sensitive dye recording with glutamate-uncaging to directly measure the amplitude and duration of unitary EPSPs in single spines in cortical layer 5 pyramidal neurons from mouse brain slices. Our findings indicate that EPSPs in the spines that resemble miniature EPSPs at the soma are always less than 20 mV, and last on average 15 ms. In the same spines, we also determined the diffusional coupling of the spine with the parent dendrite to estimate the spine neck resistance (R_{neck}). We show that large R_{neck} enhances the EPSP amplitude within the spine through passive mechanisms, but at the same time, increases the amount of attenuation of the synaptic input at the soma. These findings are recapitulated with a morphologically realistic computational model of a L5 pyramidal neuron from which we can also predict the unitary synaptic conductances associated with these EPSPs.

Moreover, since the propagation of the EPSP from the spine to the soma is also determined by the dendritic morphology, we performed detailed simulations to assess how the spine neck and the dendritic resistance combined can facilitate or prevent the generation of sodium dendritic spikes from the synchronous activation of synaptic input. We find from these simulations that distal spines with small R_{neck} are more likely to generate sodium spikes if the synaptic conductance is large enough, and the distribution of voltage-gated sodium channels (VGSCs) is homogeneous throughout the dendrite. These sodium spikes backpropagate into the spines, and are largely dependent on the density of VGSCs within the parent dendrite, but not within the spine head. The implications of these observations for dendritic input integration and future experiments to test these predictions are discussed.

Excitatory Post-Synaptic Potentials in Dendritic Spines on Basal Dendrites of L5 Pyramidal Neurons

Erika Hoyos-Ramirez

B.S., Universidad de Antioquia, 2008

A Dissertation

Submitted in Partial Fulfillment of the

Requirements for the Degree of Doctor of Philosophy

at the

University of Connecticut

2014

APPROVAL PAGE

Doctor of Philosophy Dissertation

Excitatory Post-Synaptic Potentials in Dendritic Spines on Basal Dendrites of L5 Pyramidal Neurons

Presented by

Erika Hoyos-Ramirez, B.S.

Major Advisor _____

Dr. Leslie M. Loew

Associate Advisor _____

Dr. Srdjan Antic

Associate Advisor _____

Dr. Ji Yu

Associate Advisor _____

Dr. John Carson

University of Connecticut

2014

Acknowledgements

I am especially grateful to my advisor Dr. Leslie Loew for giving me the opportunity to be his student and to learn under his guidance. He is not only a great scientist, but also a great human being, an example of dedication, humility, and hard work for all of us. I am also very grateful to Dr. Corey Acker, who played a fundamental role in making this project possible.

Dedication

To my family and my wonderful husband, who are an infinite source of support and motivation. They fill my life with happiness, and give me the strength to fight the hardest battles.

Table of Contents

List of Figures and Tables

List of Abbreviations

EPSPs: Excitatory postsynaptic potentials.

L5: Layer 5.

R_{neck}: Spine neck resistance.

VGSCs: Voltage-gated sodium channels.

VSDI: Voltage sensitive dye imaging.

Glu-uncaging: Glutamate uncaging.

AMPAR: α-amino-3-hydroxy-5-methyl-4-isoxazolepropionic acid receptor.

NMDAR: N-methyl-D-aspartate receptor.

VGCCs: Voltage-gated calcium channels.

LVA: Low-voltage activated.

HVA: High-voltage activated.

SK2: Voltage-independent/Ca^{2+}-dependent K^+ channel.

Kv4.2: Voltage-gated K^+ channels.

RhoA: Ras homolog gene family, member A.

Rac1: Ras-related C3 botulinum toxin substrate 1.

Cdc42: Cell division control protein 42 homolog.

Ras: Rat sarcoma.

GTP: Guanosine-5'-triphosphate.

GDP: Guanosine-5'-diphosphate.

ROCK: Rho-associated protein kinase.

WAVE: Wasikott-Aldrich syndrome protein family Verprolin homologous proteins.

Arp2/3: Actin-related protein 2/3 complex.

Tiam1: T-cell lymphoma invasion and metastasis 1, a Rac-specific guanine nucleotide exchange factor.

α1-chimerin: Rac GTPase-activating protein.

p250Gap: Rho GTPase-activating protein.

MAPK: Mitogen-activated protein kinase.

PP1: Protein phosphatase 1.

PSD: Postsynaptic density.

PSD-95: Postsynaptic density protein 95.

CREB: cAMP response element-binding protein.

BDNF: Brain-derived neurotrophic factor.

AD: Alzheimer's disease.

LTP: Long-term potentiation.

CaMKII: Ca^{2+}/calmodulin-dependent protein kinase II.

PKA: Protein kinase A.

PKC: Protein kinase C.

TARPs: Transmembrane AMPAR regulatory proteins.

LTD: Long-term depression.

GABA: Gamma-aminobutyric acid.

IPSP: Inhibitory postsynaptic potential.

$[Ca^{2+}]_i$: Intracellular Ca^{2+} concentration.

APs: Action potentials.

R_h: Spine head membrane resistance.

R_d or R_{dend}: Dendritic input resistance.

R_{spine}: Input resistance of the spine.

I_{syn}: Synaptic current.

g_{syn}: Synaptic conductance.

E_{syn}: Reversal potential of the synapse.

V_s: Spine voltage.

V_d: Dendritic voltage.

FRAP: Fluorescence recovery after photobleaching.

uEPSPs: Glutamate uncaging-evoked excitatory post-synaptic potentials.

MNI-glutamate: 4-Methoxy-7-nitroindolinyl-caged-L-glutamate.

ACSF: Artificial cerebrospinal fluid.

VSD: Voltage-sensitive dye.

DIC: Infrared differential interference contrast.

bAP: Backpropagating action potential.

τ_{eq}: Equilibration time constant.

PSF: Point spread function.

R_a: Cytoplasmic resistivity.

Tau: Decay time constant.

VGKC: Voltage-gated K^+ channels.

AIS: Axon initial segment.

R_L: Longitudinal resistance.

Chapter 1

Introduction

Dendritic spines constitute the postsynaptic sites of excitatory synaptic input in many mammalian brain regions that play fundamental roles in learning and behavior. Spines are highly plastic, and can act as chemical and possibly electrical compartments capable of modulating synaptic efficacy (*1*), input integration and neuronal plasticity. Structural abnormalities in dendritic spines have been found in patients and animal models of neurodegenerative and developmental disorders, such as Alzheimer's disease, autism and mental retardation (*2*). Understanding how spines influence brain function by means of their biophysical properties and dynamics will help elucidate how neurons process information, and store memory, as well as help identify potential therapeutic targets for diseases caused by abnormal spine physiology.

1.1 Dendritic Spines

Dendritic spines are small pleomorphic membrane protrusions that emanate from the dendrites of mature neurons in many brain regions, including pyramidal neurons of the neocortex and the hippocampus, medium spiny neurons of the striatum and Purkinje cells of the cerebellum. The morphology of spines consists of a spine head, whose volume can range between 0.005-1 μm^3, and a spine neck that is variable in diameter and length (*3*). Spines are usually classified into

three types based on their morphology: thin, mushroom, and stubby. This morphological diversity plays an important role in brain function, since the spine shape allows the compartmentalization of biochemical signals, and possibly also of electrical signals, which provide synapses with specific biochemical properties associated with their synaptic input, and long-term plasticity (*4*). The transfer of synaptic potentials from the spine to the dendritic shaft, and to the soma, is likely to be effected by the spine shape. Given that very narrow necks could potentially act as electrical resistors, they could have dualistic effects on synaptic potentials. On one hand, narrow spine necks could increase the amount of voltage attenuation traveling from the spine to the dendrite, but on the other hand, they could also facilitate the activation of voltage-gated channels within individual spine heads. This will make spines behave as electrical amplifiers (*5*). In the research presented here, we investigate these questions by means of voltage sensitive dye imaging (VSDI) in singles dendritic spines, coupled with 2-photon glutamate uncaging (glu-uncaging). We combine these techniques with compartmental modeling, in order to study the role of the spine neck resistance in shaping synaptic voltages traveling from the spine to the dendrite, and to the soma.

Spines appear early during development, and their formation is part of the establishment of neural circuits (*6*). There is strong evidence suggesting that spines form from thin membrane protrusions called filopodia that can form transiently on dendrites. Time-lapse imaging in neuronal cultures and brain slices

has shown that the highly dynamic filopodia initiate contacts with presynaptic axons, and could occasionally transform into spines if they receive synaptic input (*7-10*). Nevertheless, observations that dendritic spines can form directly from dendritic shafts without the initial filopodia have also been made (*9*).

The dynamics of spine formation and elimination vary with the age. *In vivo* imaging studies have demonstrated that at early postnatal ages spines are highly dynamic and start to accumulate rapidly (*11*). As animals mature into adulthood, the spine turnover rate decreases, and a process called spine pruning takes place, where the overall number of synapses is reduced to leave only the more efficient synaptic configurations (*12-14*). Although at a slower rate, the process of spine formation and elimination persists during adulthood (*15*), and it is thought that this process is balanced so that the global number of spines is stabilized (*16*).

A positive correlation between spine stability and spine size has been found, although this correlation is not absolute. Imaging of dendritic spines in the mouse neocortex (postnatal day 14-511) over days to months showed that thin spines could appear and disappear within days, whereas most thick spines persisted for months (*17*). This observation, together with evidence that the percentage of stable spines increases with age (*18*) have led Kasai et al (*19*) to propose that persistent spines are the result of an activity-dependent enlargement.

The molecular composition of spines is rich in synaptic receptors, ion channels, actin cytoskeleton, and signaling molecules, such as small GTPases, kinases and phosphatases (Figures 1.1 and 1.2). In L5 pyramidal neurons, upon release from the presynaptic terminal, glutamate binds to α-amino-3-hydroxy-5-methyl-4-isoxazolepropionic acid receptor (AMPARs) and N-methyl-D-aspartate receptor (NMDARs). AMPARs mediate the fast component of the synaptic transmission by allowing the influx of Na^+ and Ca^{2+}, and efflux of K^+, that leads to the membrane depolarization called excitatory postsynaptic potential (EPSP). NMDARs are also nonselective cation channels, but are blocked by extracellular Mg^{2+} at resting membrane potentials. This block is relieved when the membrane depolarizes either by a backpropagating action potential (bAP), or by the opening of AMPARs. Opening of NMDARs is responsible for the slower component of the EPSP that triggers intracellular signaling pathways by allowing the influx of Ca^{2+} (*20*). Spines also have voltage-gated Ca^{2+} channels (VGCCs), and possibly, voltage-gated Na^+ channels (VGSCs) as well (*21-23*) (Figure 1.1).

The synaptic activity of VGCCs and VGSCs has been most extensively studied in the apical dendrites of CA1 hippocampal neurons. Due to their larger size compared to basal and oblique dendrites, apical dendrites are more accessible to dendritic patching. The voltage-dependent properties of Na^+ and T-type Ca^{2+} channels predict that EPSPs of 10 to 20 mV would activate these channels (*24*). Dendritic patching of the apical dendrite in CA1 neurons at distances greater than 100 μm from soma has shown the presence of at least two distinct types of

Ca^{2+} channel activity (*25*). The low-voltage activated (LVA), small conductance (~9 pS) channel, and the high voltage-activated (HVA), moderate conductance (~15 pS) channel, which showed a pharmacological profile similar to the R-type Ca^{2+} channels. The HVA L-type Ca^{2+} channel activity was also found at distances within 100 μm from soma.

A systematic pharmacological study of VGCCs from apical dendrites of CA1 pyramidal neurons from juvenile mice (postnatal day 15-18) (*21*) has shown that Ca_v3 T-type, $Ca_v1.2$ or $Ca_v1.3$ L-type, and $Ca_v2.2$ N-type VGCCs contribute to the action potential-evoked Ca^{2+} transients in dendrites and spines; however, the $Ca_v2.3$ R-type VGCC seemed to be selectively localized or activated in the spine, but not in the apical dendrite. Glutamate uncaging-evoked Ca^{2+} signals in the spine mediated by the opening of the $Ca_v2.3$ R-type VGCC were also observed in this study, for somatic EPSP amplitudes that were in the upper range of miniature EPSPs (~1 mV).

Opening of VGSCs in the apical dendrites of CA1 neurons has been observed upon synaptic activation of the Schaffer collaterals, which produced dendritic EPSPs of 15 to 20 mV in amplitude (*25*). In the basal dendrites of L5 pyramidal neurons it has been shown that increasing the stimulation strength of clustered synaptic input can eventually lead to dendritic nonlinear amplification by the generation of Na^+ and NMDA spikes (*26, 27*). Although these results show that EPSPs from spatiotemporally clustered inputs can open voltage-gated channels

in the dendrites of pyramidal neurons, it remains to be demonstrated whether activation of a single synapse under physiological conditions leads to the activation of these active conductances within individual dendritic spines.

Several K^+ channels have been found in spines. The voltage-gated K^+ channel Kv4.2, a channel that carries a transient I_A current, has been found evenly distributed on dendrites and spines of CA1 hippocampal neurons (*28*). The voltage-independent/Ca^{2+}-dependent K^+ channel (SK2) has also been found in spines of hippocampal pyramidal neurons. Ca^{2+} influx through NMDARs or R-type VGCCs activates SK channels, which rapidly restore the resting membrane potential in the spine (*21*). By repolarizing the membrane, SK channels downregulate NMDARs and VGCCs. Blocking SK channels or genetically deleting them increases the dendritic excitability, and enhances the ability of spines to undergo long-term potentiation due to the increased activity of the NMDAR signaling pathway (*29*).

Dendritic spines rely on the dynamics of the actin cytoskeleton to generate the force at the plasma membrane required to maintain their shape, and to dynamically regulate it with synaptic activity (*30, 31*) (Figure 1.2). Parallel actin filaments are found in the spine neck, while a network of short cross-linked branched filaments are present in the spine head (*32-35*). AMPAR and NMDAR signaling can control actin polymerization in the spine through the activation/inhibition of small GTPases such as Ras homolog gene family,

member A (RhoA), Ras-related C3 botulinum toxin substrate 1 (Rac1), cell division control protein 42 homolog (Cdc42) and rat sarcoma protein (Ras) (*36-39*) (Figure 1.2). By switching between the guanosine-5'-triphosphate (GTP) and guanosine-5'-diphosphate (GDP)-bound states, these GTPases can change the activity of specific actin binding proteins that control actin polymerization. In general, while RhoA inhibits, Rac and Cdc42 promote the growth of spines. However, there is extensive crosstalk between these pathways. RhoA can activate the Rho-associated protein kinase (ROCK), which leads to the phosphorylation of ADF/cofilin, thereby inactivating actin-depolymerization and stabilizing actin filaments. On the other hand, Cdc42 and Rac1 can lead to the activation of the WAVE (Wasikott-Aldrich syndrome protein family Verprolin homologous proteins) families of proteins, such as N-WASP and WAVE1, which play a key role in maintaining actin polymerization, and underlie the activity-dependent enlargement of spine heads through the recruitment of the Arp2/3 complex (actin-related protein 2/3 complex), an actin nucleation factor with ability to form branches in the actin cytoskeleton (*40*).

Several other proteins have been found to cause the elongation of spines downstream of the NMDAR signaling pathway. When overexpressed in cultured cortical neurons, Debrin A was shown to positively modify the length of spines (*41*), which is likely mediated mainly through its interaction with F-actin, but also with other proteins, such as profilin, myosin, gelsolin, and Ras (*42, 43*). Cortactin is another protein downstream of NMDAR signaling that is concentrated in

dendritic spines of cultured hippocampal neurons, and its overexpression can cause elongation of spines likely through its interaction with F-actin and the Arp2/3 complex (*44*).

Given that many neurological disorders associated with memory loss and behavioral disorders are often caused by abnormalities in synaptic connectivity, it is not surprising to find morphological alterations in dendritic spines in brain tissue from patients affected by Alzheimer's disease (AD), schizophrenia, mental retardation, and autism. Patients with AD show synapse and dendritic spine loss in the hippocampus and throughout the cortex (*45*). Animal models of AD carrying mutations in genes involved in the beta amyloid metabolism show deficits in working memory, and spine loss in hippocampal and cortical pyramidal neurons (*46*). Moreover, postmortem brain tissue from patients with mental retardation shows a reduced number of spines but normal spine morphology, whereas an increase in immature elongated spine density has been observed in tissue from patients with autism and fragile X syndrome (*47, 48*).

Interestingly though, while spine abnormalities are found in neurodegenerative disorders, increased spine formation has been observed in neuronal tissue recovering from injury. For example, 2-photon chronic imaging used to study synaptic function in pathological conditions has shown an increase in spine formation in peri-infarct dendrites (*49*), and retinal lesions have been shown to induce spine remodeling in the visual cortex (*50*). Thus, it is possible that by

targeting the right pathways involved in synaptic transmission within spines, new therapies could be developed to overcome the loss of synapses during brain tissue damage.

1.2 Role in Synaptic Plasticity and Input Integration

Synaptic Plasticity

Plasticity, the capacity to change in response to stimulus and experience, constitutes one of the most fundamental properties of the brain. It is plasticity that allows the brain to act as a memory storage and information-processing device, recognize sensory patterns, refine body movements, predict the external world, and recover from injury (*51*). At the cellular level, plasticity is embedded in physiological and structural interactions, and dendritic spines lie at the heart of them.

It became evident that spines played an important role in plasticity when changes in synaptic strength were accompanied by stable morphological changes in spines (*52*), and the later observation that motor learning and sensory stimulation could induce the formation of new spines (*53, 54*). This, together with the observation that large spines can persist for long periods of time, whereas thin and small spines are more transient (*17, 55*), support the proposition that large spines could be the structural form of memories, and that smaller spines could allow the acquisition of new memories by the formation of new synapses (*56*).

Different forms of synaptic plasticity have been discovered experimentally depending on the frequency and duration of the synaptic stimulation, which leads to the activation of particular signaling pathways. For example, high frequency synaptic stimulation, or glutamate uncaging, in the hippocampus and the neocortex, triggers an NMDAR-dependent form of plasticity called long-term potentiation (LTP), characterized by a long-lasting increase in the somatic EPSP amplitude. This form of plasticity is mediated by several kinases including Ca^{2+}/calmodulin-dependent protein kinase II (CaMKII), protein kinase A (PKA), and protein kinase C (PKC), that become activated by the rise in intracellular Ca^{2+} through the NMDARs (*2*). These kinases induce the phosphorylation of AMPARs and the transmembrane AMPAR regulatory proteins (TARPs), which increase both the trafficking of AMPARs at the synapse and the AMPAR single channel conductance (*57-59*). This addition of AMPARs at the synapse is accompanied by an immediate (<1 min) increase in the spine head volume, and an enhanced postsynaptic response to further stimulation (*52, 59, 60*). While the initial expansion of the spine head is NMDAR-dependent, the long-lasting expansion depends on the activation of CaMKII (*61*).

In contrast to LTP, another form of synaptic plasticity has also been found called long-term depression (LTD), which can be induced by low-frequency (1-5 Hz) stimulation of the synapse, and is characterized by a decrease in the amplitude of the somatic EPSPs. Induction of LTD also depends on the activation of NMDARs, however, the resulting magnitude and duration of the Ca^{2+} influx

triggers phosphatases, such as calcineurin and protein phosphatase 1 (PP1), instead of kinases. These phosphatases dephosphorylate AMPARs leading to their downregulation and removal from the synapse (*62*). Shrinkage of the spine after LTD induction has been observed, and is mediated by the actin-severing protein cofilin (*63*).

Input Integration

The function of spines during input integration is just now beginning to be elucidated experimentally, and will strongly depend on their biophysical properties, such as channel composition and spine neck resistance. These parameters are difficult to measure experimentally due to the small size of spines that makes them inaccessible to classical electrophysiology. Much more is known about the role of dendrites in input integration, which has been shown to also depend on the dendritic morphology, distribution of channels, and spatio-temporal pattern of the synaptic input.

The dendritic morphology of pyramidal neurons is complex, and allows for the spatial segregation of inputs into specific dendritic subcompartments, such as basal, apical and tuft dendrites (Figure 1.3). Cable theory, a mathematical formulation that allows the quantification of electric current along passive dendritic cables, predicts that in the absence of active (voltage-gated) conductances, a temporal sequence of excitatory inputs will produce a response at the soma that will depend on the dendritic input location (*64*).

Different modes of dendritic integration, linear, sublinear and supralinear have been observed experimentally. In hippocampal and neocortical brain slices, activation of hundreds of unitary inputs by synaptic stimulation have been shown to sum linearly at the soma, requiring the activation of voltage-gated mechanisms that could counteract the local shunting predicted by cable theory (*65, 66*). The authors in favor of this linear mode of summation suggest that even though dendrites are capable of non-linear behavior, due to the presence of voltage-gated channels and their ability to fire dendritic spikes, they are tuned to sum input linearly, and maintain the importance of individual inputs at the soma (*67*).

This view contrasts with other studies, which have shown that input summation can be highly nonlinear under certain conditions (*26, 68-71*). Nettleton et al (*68*) showed in L5 pyramidal neurons that two synaptically evoked AMPA-mediated EPSPs, one coming from layer I and the other coming from layer III-V, could be summed supralinearly at the soma if both inputs were activated simultaneously or if the soma was hyperpolarized. This summation could become linear if the Na^+ and Ca^{2+} postsynaptic conductances were blocked, or the time between stimuli increased from 0 to 30 ms. Furthermore, Schiller et al (*69*) showed that coactivation of clustered inputs on basal dendrites of L5 pyramidal neurons initiated local dendritic NMDA spikes that resulted in somatic depolarizations of up to ~6 mV in amplitude and ~64 ms in duration, resulting in more than 200% somatic voltage amplification. Similar NMDA spikes have also been found in the

distal tuft dendrites of the same neurons (*72*). In addition, a recent study showed that glutamate excess in the extracellular space, achieved through repetitive synaptic stimulation or glutamate iontophoresis, could generate NMDA spikes that were restricted to the stimulation site, but that further stimulation could produce characteristic plateau potentials that spread throughout the entire dendritic branch (*70*). These highly non-linear plateau potentials showed sublinear summation at the soma, suggesting that the activation of extrasynaptic NMDARs allows for signal compression in cortical circuits.

These conflicting results of linear versus non-linear dendritic integration have been somewhat captured in a theoretical model known as the “two-layer model of synaptic integration”, which suggests that inputs are first processed within separate dendritic compartments, each governed by their own sigmoidal thresholding nonlinearity, and whose outputs are linearly combined at the soma to determine the cell response (*73, 74*). The closest experimental validation of this model is one in which focal extracellular synaptic stimulation was applied at two different dendritic locations, and the responses were measured at the soma (*75*); this study showed that nearby inputs on the same branch summed sigmoidally, where the stimulus intensity determined whether summation was sublinear or supralinear, and that inputs on different branches summed linearly.

The effect of the spatiotemporal pattern of synaptic input in determining the mode of dendritic integration has been demonstrated in several studies. For example,

Losonczy et al (*76*) showed that asynchronous input delivered to radial oblique dendrites of CA1 pyramidal neurons produced somatic depolarizations that summed linearly, while highly synchronized inputs exhibited supralinear summation of somatic voltage responses. Similarly, by doing whole-cell dendritic recordings, Gasparini et al (*77*) showed that when synaptic input arrives asynchronously (within 10-100 ms all in the same dendrite) or highly distributed in space (7-10 uncaging events over 150 µm of dendrite), the dendritic arbor performs a linear integration; in contrast, if synaptic input is synchronous (within 1-3 ms all in the same dendrite) and spatially clustered (7-10 uncaging events over 20 µm of dendrite), the dendritic compartment receiving the input performs a highly nonlinear integration.

Another important aspect of dendritic integration is the role of the inhibitory input. Dendritic inhibition caused by GABAergic interneurons could exert nonlinear shunting effects on the excitatory potential. A study that looked at this (*78*), used iontophoretic application of glutamate and GABA in hippocampal slices, and compartmental modeling, to show that the somatic responses to a pair of coactivated excitatory and inhibitory inputs could be predicted by a simple rule: the sum of the EPSP, the inhibitory postsynaptic potential (IPSP), and a nonlinear component that is proportional to their product (k*EPSP*IPSP). Here, k reflects the strength of the shunting effect. This simple rule provides a quantitative basis for analyzing inhibition domains on pyramidal cells produced by specific innervations of inhibitory interneurons.

To what extent dendritic spines influence input integration is still an opened question. Spines could affect the dendritic summation in several ways: (1) by increasing the total membrane capacitance of the dendrite which could slow down the time course of synaptic inputs and increase the time window for input integration (*67, 79*); (2) by changing the spine neck resistance which could modulate the amount of attenuation, and the amount of depolarization experienced by neighboring spines; (3) by allowing the activation of voltage-gated channels which could amplify synaptic input, and the resulting depolarization at the dendrite. Indirect evidence of this latter mechanism has been shown in a recent study in CA1 hippocampal neurons, where the large neck resistance (R_{neck} = ~500 MΩ) measured through a combination of glutamate uncaging, Ca^{2+} imaging, dendritic patching, and compartmental modeling, suggested that spines could encourage nonlinear input integration by allowing the activation of voltage-gated conductances (*80*).

1.3 Biochemical Compartmentalization in Spines

There is extensive experimental evidence demonstrating that spines can compartmentalize intracellular Ca^{2+} signals, and thus provide a synapse specific biochemistry associated with synaptic activity, and long-term plasticity (*4*). Ca^{2+} influx into spines occurs through the activation of ionotropic glutamate receptors and VGCCs. NMDARs are particularly permeable to Ca^{2+}. Typically, the spine is first depolarized by the activation of AMPARs upon binding to glutamate, which

releases the Mg^{2+} block of NMDARs. Opening of NMDARs leads to Ca^{2+} influx, and further depolarization. If the depolarization is high enough, it can lead to the activation of VGCCs. It has been shown in hippocampal slices that subthreshold synaptic stimulation leads to a NMDAR-dependent rise in intracellular Ca^{2+} levels $[Ca^{2+}]_i$ that is restricted to the spine; however, if the stimulus intensity was high enough, the $[Ca^{2+}]_i$ rise could spread throughout the dendritic tree in a NMDAR-independent fashion (*81, 82*). Furthermore, protocols that pair action potentials with synaptic stimulation, an alternative method used for LTP induction, have shown an NMDAR-dependent supralinear rise in $[Ca^{2+}]_i$ can also be restricted to the stimulated spine (*83, 84*). Although the spine morphology plays a key role in the compartmentalization of $[Ca^{2+}]_i$, as has been demonstrated by the positive correlation between the spine neck length and the decay time constant of $[Ca^{2+}]_i$ signals within the spine head (*85*), other mechanisms can contribute as well. Particularly, extrusion mechanisms such as Ca^{2+} pumps can quickly remove the $[Ca^{2+}]_i$ from the spine cytosol before it has time to diffuse into the dendrite.

The role of the spine neck in regulating the diffusional coupling between the spine and the parent dendrite has been explored in several studies, which show that the amount of coupling can be regulated by pre- and postsynaptic activity. Studies in hippocampal slices have shown that pairing glu-uncaging evoked EPSPs with postsynaptic action potentials can increase the diffusional isolation of the spine (*86*). Moreover, long depolarizations, or bursts of action potentials (APs), have also been shown to increase the diffusional isolation of the spines,

through a process that is mediated by Ca^{2+} influx (*87*).

In contrast to the well compartmentalized synaptic $[Ca^{2+}]_i$ signals in individual spines, small GTPases exhibit a more variable behavior. Using cultured hippocampal slices and glu-uncaging it has been shown that Ras can spread out of the target spine into the dendrite, and neighboring spines, up to 10 µm away (*88*). Moreover, by using 2-photon glu-uncaging to induce a long-term increase in the spine head volume associated with LTP, Murakoshi et al (*89*) showed that while both RhoA and Cdc42 are activated, Cdc42 remains in the stimulated spine, and RhoA diffuses and spreads up to 5 µm away. Thus, it seems that Ras and RhoA can carry synaptic signals from spine to spine, whereas Cdc42 does not.

The morphology of spines also plays a key role in confining the glutamate receptors at the synapse, preventing their lateral diffusion throughout the plasma membrane (*90*). This could play a critical role in the synaptic response, since modeling studies have shown that clustering of AMPARs at the postsynaptic density (PSD) can determine their opening probability (*91*); given that the area of the AMPAR activation upon glutamate release has similar dimensions to the millimolar glutamate concentration surrounding a vesicle release site, receptors that are not well aligned with the presynaptic release site are unlikely to open. Experiments have shown that TARPs link the AMPARs with PSD-95 (postsynaptic density protein 95), one of the most abundant PSD scaffold

proteins (*58, 92*), and that this association with TARPs can double their single channel conductance (*93*). The spatial compartmentalization of NMDARs also plays a key role in the direction of plasticity. For example, whereas activation of extrasynaptic NMDARs leads to dephosphorylation of the CREB and LTD, activation of synaptic NMDARs promotes phosphorylation of CREB and LTP (*94, 95*). CREB stands for cAMP response element-binding protein, and is a cellular transcription factor that regulates the expression of genes such as *c-fos, BDNF* (brain-derived neurotrophic factor), and other neuropeptides important in the maintenance of the late phase of LTP.

1.4 Electrical Compartmentalization in Spines

Extensive theoretical studies have predicted that the electrical behavior of spines depends strongly on the intracellular resistance of the spine neck (R_{neck}). In principle, a large R_{neck} would produce a large input impedance at the spine head, and as a consequence, synaptic input would be expected to produce a large local EPSP in the spine. However, this would also mean more attenuation at the parent dendrite and the soma. More detailed discussions of the physiological significance of this amplification/attenuation effect of larger R_{necks} will be provided in Chapter 2, as well as some of the experimental evidence that suggests that spines behave as electrical compartments. In this section, we will discuss the theoretical approaches that have been used to model spines as a resistor-capacitor circuit.

Theoretical Approaches

The biophysical properties governing the behavior of passive spines have been studied extensively using theoretical models that approximate the spine to an equivalent circuit. A simplified electrical model of such a spine is shown in Figure 1.4 (*1, 96*). Any current injected into the spine must flow either across the spine head membrane resistance (R_h) or through the axial resistance of the spine neck (R_{neck}) and along the dendritic input resistance (R_d). However, given that the membrane area of the spine is so small (< 1 μm^2), R_h can be assumed to be infinite, and therefore, the input resistance of the spine R_{spine} can be well approximated to the sum of R_{neck} and R_d. An important consequence of this high R_h and low capacitance of the spine caused by their small size, is that dendritic voltage pulses will be able to invade the spine without significant voltage attenuation, whereas EPSPs will attenuate as they travel from the spine towards the dendrite.

The current flowing across the synapse at the spine head (I_{syn}) can be expressed as:

$$I_{syn} = g_{syn} (E_{syn} - V_s)$$

Where g_{syn} is the synaptic conductance, E_{syn} is the reversal potential of the synapse, and V_s is the voltage in the spine. By applying Ohm's law, it is possible to solve for V_s and the voltage in the dendrite (V_d), so that:

$$V_s = g_{syn} R_{spine} E_{syn} / (1 + g_{syn} R_{spine})$$

$$V_d = g_{syn} R_d E_{syn} / (1 + g_{syn} R_{spine})$$

From these two equations it follows that in the limit where g_{syn} is small relative R_{spine}, the synapse acts as a current source of amplitude $g_{syn}E_{syn}$, and the dendritic voltage is independent of R_{neck}. In this limit, the EPSP attenuation factor will depend solely on the difference in the input resistances between the spine and the dendrite, so that $V_d / V_s = R_d / R_{spine}$. However, if g_{syn} is large relative R_{spine}, V_s approaches E_{syn}, and V_d converges to R_dE_{syn}/R_{spine}. In this limit, the synapse acts as a voltage source E_{syn}, and changes in R_{neck} can affect the amount of current entering the spine and reaching the dendrite (*1*).

This theoretical analysis of passive spines was the foundation for understanding their structural and electrical properties, in the absence of voltage-gated channels. However, with the discovery of active conductances present in dendrites (*97-99*) it became clear that spines could act as electrical amplifiers by allowing the compartmentalization of voltage, and an R_{neck} dependent increase in the EPSP amplitude that could facilitate the activation of fast voltage-gated Na^+ and Ca^{2+} channels (*5, 100-102*). Computational models of spines that incorporated the formulation of the action potential kinetics (*100*) showed that in active spines, the increase in the spine EPSP amplitude was non-linear with

respect to gradual increments in g_{syn}. Moreover, while in passive spines successive increments in R_{neck} led to linear increments in the spine EPSP, and gradual decrements in the dendritic EPSP, this was not the case for active spines. When R_{neck} reached 400 MΩ in those simulations, the spine fired an action potential that resulted in a larger dendritic EPSP compared to that produced by the passive spine.

Experimental evidence for electrical compartmentalization in spines is just now beginning to emerge with the main difficulty being the inaccessibility of spines to classical electrophysiology. Growing amounts of experimental data based on Ca^{2+} and voltage imaging in spines is starting to suggest that spines can indeed behave as electrical compartments (see Chapter 2). Nevertheless, none of these studies have been able to directly measure the EPSP in individual spines in relation to the spine neck resistance. This is one of the aims of this study, where we will combine glu-uncaging and VSDI in spines to measure the amplitude and dynamics of unitary EPSPs in single spines, as well as their attenuation at the soma. This technique will be complemented with fluorescence recovery after photobleaching (FRAP) to estimate the R_{neck} from the same spines from which the EPSP is measured. Our experiments demonstrate that proximal spines in the basal dendrites of L5 pyramidal neurons act as electrical compartments, with EPSP amplitudes always less than 20 mV for EPSPs that resemble miniature EPSPs at the soma. We show that R_{neck} enhances the EPSP amplitude within the spine mainly through passive mechanisms, and that large R_{necks} do increase

the amount of somatic attenuation of synaptic input. By simulating the experimental results using a morphological realistic model of a L5 pyramidal neuron, we were able to recapitulate the experimentally observed spine to soma amplitude ratio, as well as estimate the amplitude and duration of these EPSPs in the parent dendrite. From these simulations, it was also possible to estimate the unitary synaptic conductances associated with these spine EPSPs. In the last chapter, this model will be used to explore the interplay between R_{neck} and the dendritic resistance in the generation of dendritic spikes.

Figures

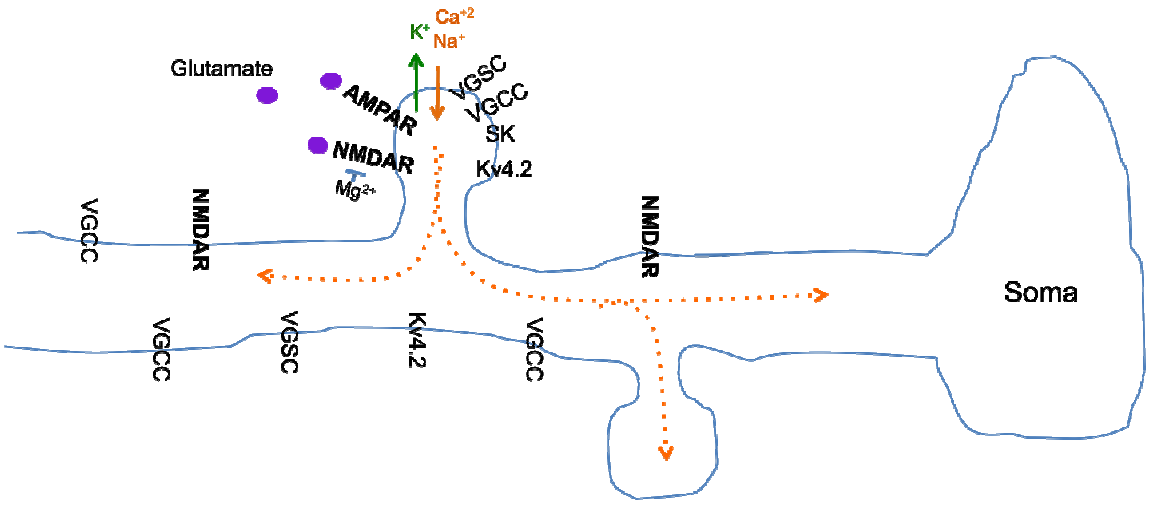

Figure 1.1. Channel composition of dendritic spines in L5 pyramidal neurons. Glutamate molecules (purple circles) bind to AMPARs and NMDARs. At resting potentials, NMDARs are blocked by Mg^{2+}. AMPARs and NMDARs are permeable to Na^{+}, Ca^{2+} and K^{+}. This current flow depolarizes the spine membrane causing the EPSP, which travels through the neck to reach the dendrite and the soma (dotted orange arrows). Other channels present in the spine and the dendrite are VGSC: voltage-gated sodium channels, VGCCs: voltage-gated calcium channels, SK: Ca^{2+}-depended K^{+} channels, Kv4.2: voltage-gated K^{+} channels.

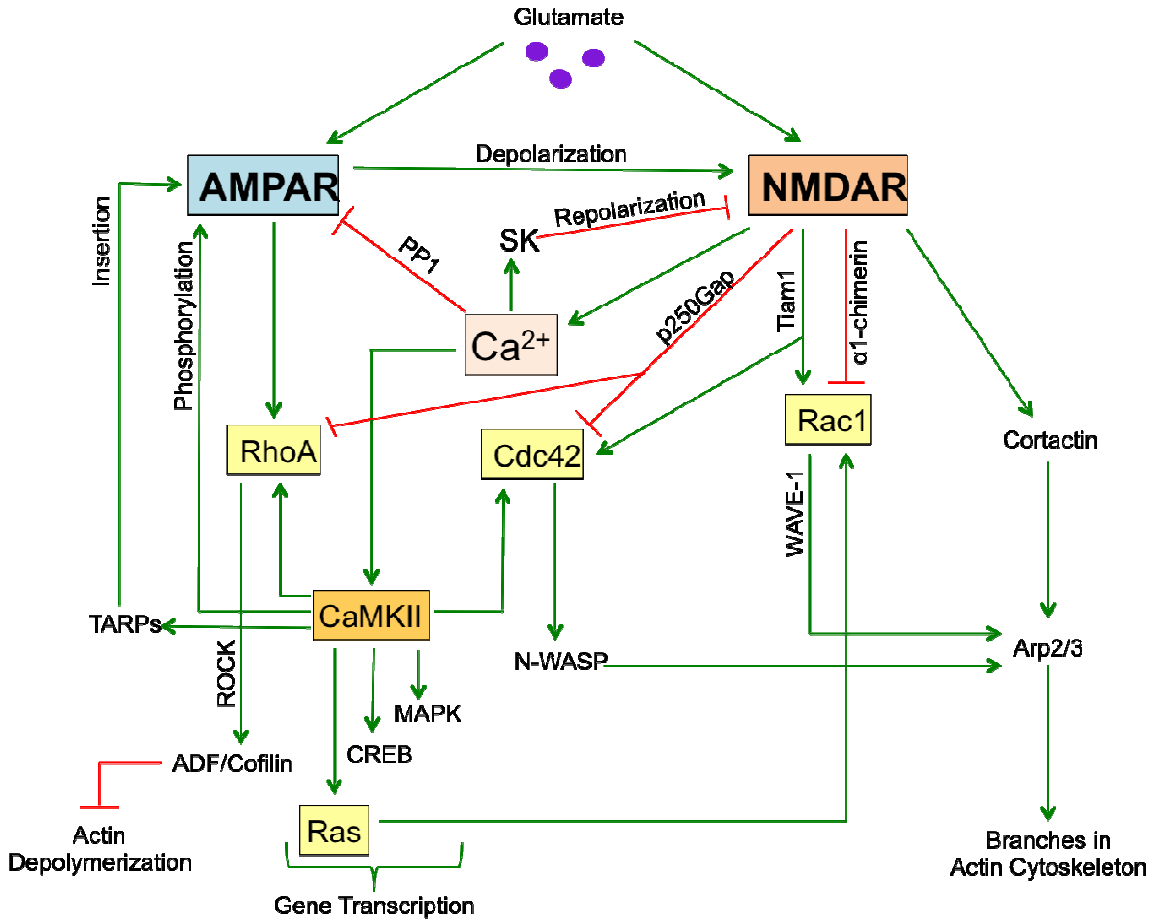

Figure 1.2. Interplay between signaling pathways activated by AMPARs and NMDARs in dendritic spines of pyramidal neurons. Green arrows indicate activation, and red blunted arrows indicate inhibition. The mechanism or protein mediating the interaction is shown next to the arrow.

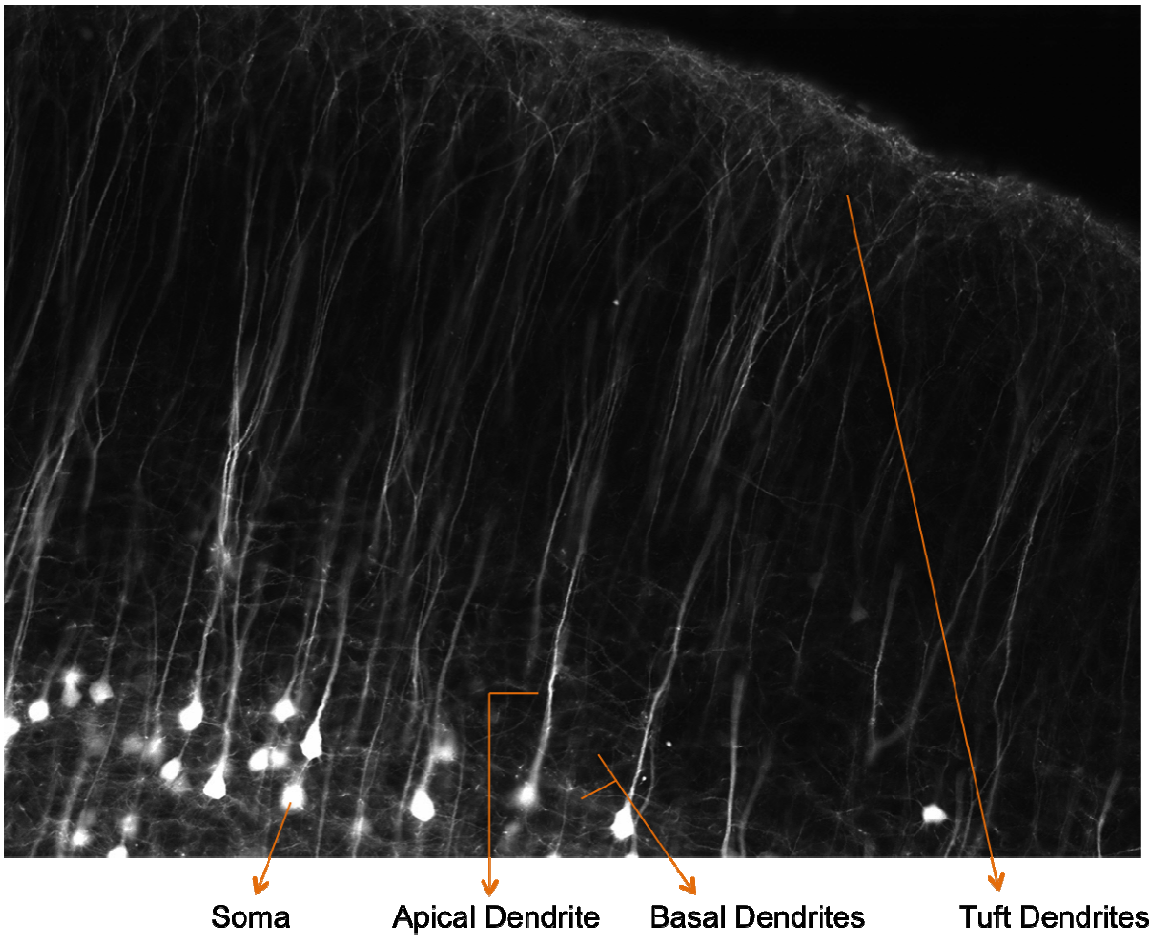

Figure 1.3. Dendritic morphology of L5 pyramidal neurons in the mouse neocortex. Confocal image of a collapsed z-stack taken from the neocortex of the Thy1 transgenic mouse. In this transgenic, GFP expression is driven by the Thy1 promoter, and occurs mainly in L5 pyramidal neurons. This is a sagittal fixed brain slice 100 µm thick. The different dendritic compartments: basal, apical and tuft are shown by the arrows.

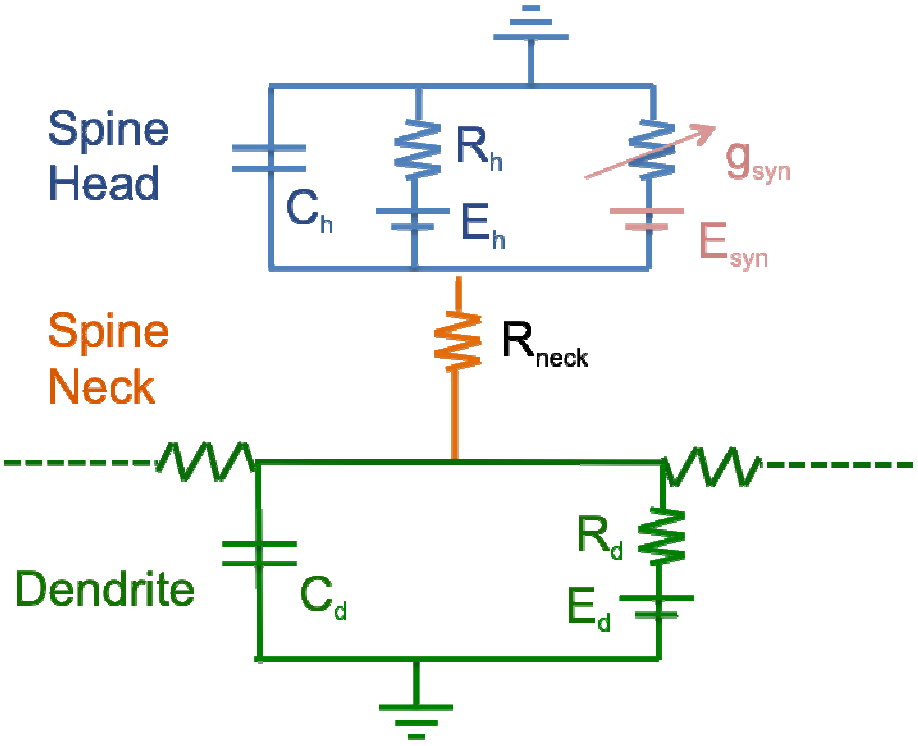

Figure 1.4. Electrical model of a passive spine. Blue denotes the spine head compartment, orange the spine neck, and green the dendrite. C_h, R_h and E_h are the membrane capacitance, membrane resistance, and reversal potential in the spine head, respectively. g_{syn}: synaptic input conductance at the spine head, E_{syn}: synaptic reversal potential. R_{neck}: spine neck resistance. C_d, R_d and E_d are the membrane capacitance, membrane resistance, and reversal potential at the dendrite, respectively. Figure based on (*1*).

Chapter 2

Excitatory Post-Synaptic Potentials Measured in Dendritic Spines of L5 Pyramidal Neurons

Authors: Erika Hoyos, Corey D. Acker, Leslie M. Loew

2.1 Introduction

Dendritic spines are the sites of excitatory post-synaptic input in many mammalian brain regions, including the neocortex. They are pleomorphic membrane protrusions connected to the dendrite through a spine neck that is variable in diameter and length. It has been previously shown that spines can compartmentalize Ca^{2+} signals, and thus provide synapse specific biochemical properties associated with long-term plasticity (*4, 90, 103, 104*); spines are also likely to play a key role in the transfer of synaptic potentials to the dendritic shaft and the soma, and the extent of this electrical compartmentalization is just now beginning to be elucidated experimentally (*105*). This represents a fundamental question in neuroscience since the postsynaptic responses to synaptic input, as well as the likelihood that a synapse will undergo long-term plasticity, will largely depend on the interplay between biochemical and electrical signals within individual dendritic spines.

Theory predicts that the electrical behavior of spines depends strongly on R_{neck} (*4, 5, 105*). In principle, a large R_{neck} would produce a large input impedance at the spine head, and as a consequence, synaptic input would be expected to produce a large local EPSP in the spine. However, this would also mean more attenuation at the parent dendrite. Several not mutually exclusive hypotheses for the physiological significance of this seemingly dualistic effect of R_{neck} have been previously suggested: 1. R_{neck} could provide a partial electrical isolation of the synaptic input from other synapses, which could lead to a more linear summation of different inputs in the dendrite; 2. R_{neck} could be a variable used for controlling the effectiveness of synaptic inputs; 3. R_{neck} could facilitate the activation of voltage-gated channels within the spine, causing non-linear local amplification of synaptic responses; 4. the voltage attenuation at the dendrite caused by R_{neck} could make neurons responsive only to combinations of synchronous stimulus or to stimulus of certain amplitudes (*4, 5, 105*).

A growing body of experimental data suggests that spines can indeed behave as electrical compartments. For example, synaptic stimulation through glutamate uncaging can lead to differential activation of VGCCs in the spine and the parent dendrite, suggesting that the spine head is not isopotential with the dendrite when it receives synaptic input (*106*). More recently, it was shown through glutamate uncaging, calcium imaging and dendritic patching, and assuming that the calcium influx is proportional to the local voltage, that the amplitude ratio of the uncaging-evoked excitatory post-synaptic potentials (uEPSPs) between the

spine and the parent dendrite could be as high as 45 for apical trunk spines of CA1 pyramidal neurons (*80*); in that study, the amplitude ratio was also used to estimate R_{neck}. A more direct measurement of voltage in spines through VSDI has shown that synaptic responses to large-scale (more than one synapse) synaptic stimulation are larger in the spine head than in the parent dendrite (*107*). Taken together, this evidence strongly suggests that R_{neck} can filter electrical signals that travel from the spine to the dendrite; however, this is not the case for signals traveling from the dendrite into the spine. Using VSDI, it was recently shown that slow and fast electrical signals propagate from the parent dendrite into the spine without significant voltage attenuation, even for spines with widely different neck lengths (*108*).

Although direct measurements of R_{neck} remain elusive, previous studies have estimated the value of R_{neck} through the measurement of the diffusional coupling between the spine and the dendrite (*86, 87, 109*). Since the electromobility of ions in the cytosol is proportional to their diffusivity, the diffusion time constant of a cytosolic dye through the spine neck and the cytoplasmic resistivity can be used to estimate R_{neck} (*109*). The advantage of using this method is that it is independent of the EPSP amplitude and the detection threshold of voltage signals. Studies in hippocampal slices that have looked at the diffusional coupling between the spine and the dendrite have shown that it can change dynamically with synaptic activity, and that pairing uEPSPs with postsynaptic APs can increase the diffusional isolation of spines (*86*). Moreover, long depolarizations,

or bursts of APs, have also been shown to increase the diffusional isolation of spines, a process that is mediated by Ca^{2+} influx (*87*). Using a protocol that allowed the estimation of a fractional Ca^{2+} transient that is proportional to the size of synaptic EPSPs, Grunditz *et al* (*87*) found a positive correlation between the spine head depolarization, estimated from the voltage dependent activity of NMDA receptors, and diffusional resistance. But none of these studies have been able to directly measure the EPSP in individual spines in relation to the spine neck resistance.

Our laboratory has previously developed single-voxel 2-photon VSDI to measure voltage changes directly from single spines in acute brain slices (*110, 111*). In the present study, we combine this method with 2-photon MNI-glutamate uncaging and FRAP, in order to measure the voltage responses in individual spines to unitary synaptic stimuli, and to study the effect of R_{neck} on the uEPSP amplitudes. Our results show a linear relation between the amplitude of the uEPSP measured at the spine and R_{neck}. These data provide experimental evidence for previous theoretical predictions that large R_{neck} can enhance the EPSPs locally (*112-114*). However, our directly measured spine voltage responses are generally of lower amplitude than previous estimates inferred from restricted diffusion through the neck or spine calcium influx (*80, 86, 87, 106*). Our experimental results were recapitulated in a compartmental model of a L5 pyramidal neuron, which could also reproduce the spine to soma uEPSP amplitude ratio observed experimentally. These results suggest that R_{neck} is the

primary determinant of the amplitude of the EPSP measured in the spine and also determines the attenuation of the EPSP measured at the soma.

2.2 Methods

2-Photon Microscopy

Voltage sensitive dye imaging, glutamate uncaging, and FRAP experiments were performed on a custom two-photon microscope based on a previously described setup (*110*). One Chameleon Ultra II (Coherent, Inc) was used for long wavelength excitation at 1060nm, while a Chameleon XR (Coherent, Inc) was used for uncaging at 750nm. Laser power was modulated with two EOMs (350-80LA-BK with 302RM Driver, Conoptics, Inc). A 900nm LP (long pass) dichroic (Thorlabs, Inc) and a 710nm LP excitation filter (Chroma Technology Corp) were used in the long and short wavelength, respectively, excitation light paths. Light paths were combined using a 900nm LP dichroic (Thorlabs, Inc) and passed through a 710nm LP dichroic (Chroma Technology Corp) for excitation/emission separation inside a modified Zeiss Axioskop 2 FS mot upright microscope (Carl Zeiss AG) equipped with a 40X 1.0 NA water-immersion objective lens. In an added, non-descanned epifluorescence pathway, one "green" excitation channel used a 540/25nm bandpass combined with a 655nm SP (short pass, both from Semrock, Inc) filter, while a "red" excitation channel used a 680nm SP filter (Semrock, Inc). Epifluorescence excitation channels were separated by a 575nm LP dichroic (Chroma Technology Corp). Red fluorescence was also collected in trans-fluorescence pathway as previously described (*110*). Two x,y galvanometer

(galvo; 3mm on 6515H, with 671HP servos, Cambridge Technology Inc.) systems were used to separately control the positioning of the uncaging and recording lasers in a custom scan head. Laser scanning was controlled by ScanImage ver. 3.8 (Vijay Iyer; Pologruto et al., Biomedical Engineering Online, 2003) with customizations necessary for control of two sets of galvos and "single-voxel" recordings (*110*).

Electrophysiology and Dye Loading

CD1 mice (postnatal day 17-30) were anesthetized by inhalation of isoflurane, and decapitated according to an animal protocol approved by the Center for Comparative Medicine, University of Connecticut Health Center. Coronal brain slices (300 μm thick) were cut from the frontal lobes using a vibrating tissue slicer perfused with ice-cold oxygenated (95% O_2/5% CO_2) artificial cerebrospinal fluid (ACSF). ACSF contained (in mM): 127 NaCl, 25 $NaHCO_3$, 25 D-glucose, 3.5 KCl, 1.25 NaH_2PO_4, 1 $MgCl_2$, 2 mM $CaCl_2$, pH 7.4, osmolarity 306. Slices were incubated in a submerged holding chamber in ACSF at 35℃ for 25 min and subsequently maintained at room temperature (~22℃). Somatic whole-cell recordings were made at room temperature in a recording chamber perfused with oxygenated ACSF prepared the day of the experiment. L5 pyramidal neurons were visually identified using infrared differential interference contrast (DIC) optics. Cells that were ~35 μm deep from the surface of the slice were selected for patching to minimize scattering of emitted photons, and to optimize penetration of the MNI-glutamate. Whole-cell recording pipettes (9-12 MΩ) were

tip filled with intracellular solution containing (in mM): 135 K-gluconate, 7 NaCl, 10 HEPES, 2 $MgCl_2$, 2 Na_2-ATP, 0.3 Na_2-GTP, pH 7.2 adjusted with KOH (1M), osmolarity 275. Pipettes were back-filled with intracellular solution containing 3 mM of voltage-sensitive dye di-2-AN(F)EPPTEA (*115*). Passive transfer of the VSD into the neuron was monitored at the soma by exciting the dye at 1060 nm (0.7 mW). As soon as the soma fluorescence was bright (usually after ~10 min), the loading pipette was pulled out. The dye-filled neuron was left undisturbed for about 1 hour to allow diffusion of the VSD throughout the dendritic arbor. After this, the neuron was repatched with a pipette containing 150 µM of Alexa Fluor 488 dye (Life Technologies) dissolved in intracellular solution for the FRAP experiment. All recordings were made using a patch-clamp amplifier (Axopatch 200B, Axon Instruments) in current clamp mode with voltage low-pass filtered at 2 kHz.

Glutamate Uncaging

MNI (4-methoxy-7-nitroindolinyl)-glutamate (MNI-glu) (Tocris) was applied through a broken extracellular pipette located 40 µm from the surface of the slice, close to the target dendrite. The pipette contained MNI-glu (15 mM) and Alexa Fluor 488 (10 µM) dissolved in fresh ACSF. For experiments in the presence of the NMDAR antagonist, 500 µM of D-AP5 (Tocris) was added to this solution. The fluorescence from the extracellular Alexa Fluor 488 allowed estimation of the size of the uncaging pulse, and the relative concentration of the MNI-glu in the vicinity of the target spine. L5 pyramidal neurons filled with the VSD where

visualized with 2-photon excitation at 1060 nm, and bright proximal spines on basal dendrites that were well isolated from neighboring spines and the dendrite were targeted for uncaging. EPSPs at the soma were evoked by 0.5 ms uncaging pulses at 0.1 Hz. An interleaved protocol consisting of uncaging and control (no-uncaging) trials was used for noise analysis and determination of detection thresholds. MNI-glu photolysis was done at 750 nm to minimize the bleedthrough of the uncaging laser into the VSD channel, using average powers of 30-35 mW measured after the objective. The experiment was terminated if any signs of photodamage were observed, such as drastic changes in the spine morphology often associated with persistent depolarization at the soma.

Data Analysis

All the data analysis was done using custom code written in MATLAB. Single-voxel optical recordings of the VSD fluorescence (5 MHz sampling rate) in the spine were low-pass filtered with a frequency cut off of 0.5 kHz for uncaging and interleaved control trials, and 2 kHz for action potentials. The MATLAB built-in-function filtfilt was used, which yields a zero-phase distortion of the original signal. This procedure was done after the 0.5 ms uncaging artifact was removed from the optical recordings. Usually between 7-30 uncaging trials and corresponding interleaved control trials were averaged. The photobleaching of the VSD was subtracted from the averaged sweep by fitting it to a linear function using the MATLAB curve fitting toolbox. After this, a moving average of 5 ms bins (2.5 ms bin shift) was run over the uncaging and control sweeps, and from this, a

detection threshold for a “significant” optical uEPSP was determined, which was equal to the mean VSD fluorescence plus 2x the standard deviation ($F_m + 2\sigma_{5ms}$) from the control trials. If the average fluorescence for each 5 ms interval following uncaging was more than this threshold, then the optical signal had a 95% chance of being significant.

Optical uEPSPs above the detection threshold were fitted by an arbitrary function that described the transition of channels from the closed to the opened state:

$$Closed_1 \overset{k_1}{\rightarrow} Opened \overset{k_2}{\rightarrow} Closed_2$$

$$N_1 + N_o + N_2 = N_T$$

Where N_T is the total number of channels, which is the sum of the channels that are in the *Closed₁* (N_1), *Opened* (N_o) and *Closed₂* (N_2) states, and k_1 and k_2 are the rate constants. The ΔF/F over time of the VSD fluorescence in the spine for the uncaging trials will be equal to the number of channels that are in the *Opened* state, which is described by :

$$\Delta F/F(t) = N_o(t) = k_1 N_T (e^{-k_2 t} - e^{-k_1 t}) / k_1 - k_2$$

Using the MATLAB curve fitting toolbox parameters were found that best fitted the bleach-subtracted ΔF/F optical EPSP, and from these fits the amplitude and duration (FWHM) of the EPSP in the spine were measured.

To determine the amplitude of the backpropagating action potential in the spine, 4 to 10 optical recordings were averaged; to eliminate the trial-to-trial temporal jitter in the peak of the AP, spike-triggered averaging was used as in (*116*). The amplitude of the spike-triggered averaged optical AP in the spine was determined as the amplitude of the peak over background fluorescence.

Estimating the spine neck resistance

R_{neck} was estimated based on the previously described (*109*) relationship between cytoplasmic resistivity and diffusion time constants in the spine:

$$R_{neck} = R_a \times \tau_{eq} \times D_{Alexa488} / Vol_{head}$$

Where R_a is the cytoplasmic resistivity, taken to be 150 Ω cm (*80, 117, 118*); τ_{eq} is the equilibration time constant of Alexa Fluor 488 in the spine head measured through the FRAP experiment; $D_{Alexa488}$ is the diffusion coefficient of Alexa Fluor 488 in the cytoplasm, 380 $\mu m^2/s$ (*119*); Vol_{head} is the volume of the spine head, which we measured from the z-stacks of the Alexa 488 fluorescence taken at 770 nm.

Image Analysis and Spine Head Volume

All distances and spine volumes were determined from the z-stacks of the Alexa 488 fluorescence using ImageJ software. Two methods were used to measure

the spine head volume: 3D convolution and total integrated fluorescence. *3D Convolution Method:* This method consisted of convolving the point spread function (PSF) of the microscope with the spine shape to find the spine head volume. The PSF of focal volume for 2-photon excitation at 770 nm was measured using the z-stacks of 200 nm subresolution fluorescent beads. The MetroloJ plugin of the Fiji application in ImageJ was used to find the full-widths at half-maximum (FWHM) of the fluorescence profiles in the x, y and z. The PSF half widths were 0.422 µm in x, 0.526 µm in y, and 1.16 µm in z. The pixel size was 34.32 pixels/µm, and 0.3 µm/frame. Using the Gaussian PSF 3D ImageJ plugin (http://www.optinav.com/Convolve_3D.htm), a gaussian PSF was generated that had the same xyz dimensions as the experimental PSF: horizontal, vertical and depth peak widths in pixels of (34.32*0.422)/2, (34.32*0.526)/2 and (1.16/0.3)/2, respectively. To find the spine shape, the z-stack of the spine head was segmented using the 3D segmentation tool available in Virtual Cell (www.nrcam.uchc.edu); this segmented stack was scaled to the ratios of the PSF half widths: x-scale = 1, y-scale = 0.8, z-scale: 0.36. Eroding and dilating the segmented-scaled z-stack yielded different spine shapes, each of which was convolved with the 3D gaussian PSF using the Convolve 3D plugin in ImageJ. Typically a 1-3 erosions was enough to find the correct shape, which corresponds to the one that when convolved, resulted in a peak correlation coefficient equal to the dilution ratio between the spine and the parent dendrite. This dilution ratio (maximum fluorescence in the brightest ROI in the spine / maximum fluorescent in the brightest ROI in the parent dendrite) was measured

from the maximum fluorescence collapsed z-stack, after the outliers were removed and the image was smoothed (a filter that replaces each pixel with the average of its 3 x 3 neighborhood) using ImageJ. The volume of this shape was measured in Virtual Cell using the pixel size. *Total Integrated Fluorescence Method:* The maximum fluorescence collapsed z-stack of the spine and the parent dendrite was scaled using the xyz pixel size, and after removing the outliers and smoothing the image as mentioned before, the integrated density (area x mean gray value) in the spine head was measured. To calculate the spine head volume, the integrated density in the spine was divided by the maximum fluorescent in the brightest ROI of the parent dendrite.

Simulations

Simulations were performed using the NEURON 7.3 simulation environment (*120*), based on a morphologically realistic model of a L5 pyramidal neuron described previously (*118*). The passive electrical properties of the model consisted of membrane capacitance, axial resistivity and membrane resistivity of 1 μF cm^{-2}, 150 Ω cm, and 30,000 Ω cm^2, respectively. A leak conductance with density of 0.33 pS μm^{-2} was distributed throughout the soma and the dendrites. The resulting input resistance at the soma was 30 MΩ. The resting membrane potential was -70 mV. The active properties of the model were as described in (*118*), and consisted of voltage-gated sodium, potassium and calcium channels, and calcium-gated potassium channels. An active spine, with the same membrane properties as the dendrite, was attached to a basal dendrite through a

spine neck. In all simulations, the spine head and the spine neck were each treated as single compartments. The basal dendrite where the spine was attached was divided into segments of 10 μm in length each. The dendritic diameter of the segment at the base of the neck was set to the average dendritic diameter for 10 μm measured from the Alexa 488 z-stacks of the spine and parent dendrite. The spine head diameter, distance from soma, and spine neck resistance that was measured in the experiment were also input to the model (Experiment section in Table 1). An exponential synapse, with a reversal potential of 0 mV, was connected to the spine head through the NetCon function in NEURON. This produced a change in conductance with two parameters: a maximum conductance (g_{syn}) and a decay time constant (tau). This synaptic conductance represents the AMPAR conductance, and all other possible conductances associated with the spine uEPSP. Simulations lasted for 200 ms, with a 0.05 ms time step. The exponential synapse was activated at 80 ms. For each spine, simulations were run for hundreds of combinations of g_{syn} and tau, and the time series of membrane voltage in the spine, parent dendrite and soma were recorded for each simulation. The resulting amplitude and duration (half-width) of the spine EPSP for each combination of g_{syn} and tau were calculated in MATLAB based on these time series. The combination of parameters (g_{syn} and tau) that reproduced best the spine uEPSP amplitude and duration measured experimentally was considered as the best fit (Model section Table 1, and Figure 2.8). The resulting EPSP amplitude and duration at the soma and the dendrite was then calculated for this set of parameter values from the time series.

2.3 Characteristics of uncaging-evoked EPSPs in single spines

In order to study the amplitude and dynamics of uEPSPs in single spines, we constructed a 2-photon imaging system (see Methods) that allowed us to simultaneously perform 2-photon MNI-glutamate uncaging and record voltage responses from single spines, while measuring somatic responses through the patch pipette (Figure 2.1A). The VSD that we used in this study, di-2-AN(F)EPPTEA (aka PY3243) (*115*), is a fluorinated hemicyanine intracellular dye optimized for 2-photon excitation. Previous work in our laboratory has shown that exciting this dye at 1060 nm with single-voxel excitation (stationary laser spot) results in single sweep signal to noise ratio of 6 for optical recording of backpropagating action potential (bAP) in spines from acute brain slices (*110*). The current experiment consisted of first measuring the bAP in the target spine and at the soma for calibration purposes, and then interleaving uncaging with non-uncaging (control) trials (Figures 2.1B and 2.1C). These control trials are used for noise estimates and threshold detection for optical uEPSPs. Since we wanted to study synaptic responses under basal conditions, uncaging was done at 0.1 Hz to avoid potentiation or depression of the post-synaptic response. The uncaging power was increased until a reliable uEPSP in a typical physiological range of ~0.5 mV was observed from the electrical recording at the soma. We also positioned the uncaging spot at various locations around the spine to search for an optimal uncaging position, presumably corresponding to a site close to a

synapse. The spatial precision of uncaging was demonstrated by uncaging away from the optimum targeting position (where clear uEPSPs were evoked at the soma), and observing no response or a small slow rise in the somatic uEPSPs (Figure 2.2A).

In order to calibrate the optical uEPSP signals in the spine we used the amplitude of the spine's bAP (Figures 2.2B-2.2E). Action potentials were elicited through the somatic patching pipette by current injection, while the VSD signal at the spine was recorded (Figure 2.1B, and Figure 2.2B). To minimize the effect of dendritic filtering, we focused on proximal spines (< 170 µm from soma) on basal dendrites. The data for n=52 spines from 34 different cells is summarized in Figure 2.2C. Across the 52 different measurements, the mean amplitude of the AP at the soma was 92 ± 10 mV, the mean amplitude of the optical AP in the spine was 20.6 ± 4.7 % ΔF/F, and the mean distance of the spines to the soma was 58.96 ± 27.6 µm. The attenuation of the bAP's amplitude with distance in the basal dendrites of L5 pyramidal neurons has been previously studied; using VSD imaging from dendrites within a similar developmental time window as the one in this study (postnatal day 17 to 30), Acker at al (*116*) reported a length constant of bAP attenuation of 400 µm. A shorter length constant of 138 µm has also been reported using dendritic patching for dendrites later in development (postnatal day 36 to 53) (*27*). Here, we calculate the VSD sensitivity for each spine (% ΔF/F per mV) based on both of these previously reported length constants (Figure

2.2E); the corrections associated with these calibrations are small for the most proximal spines.

The main challenge of measuring uEPSPs in single spines is to overcome the signal-to-noise ratio of optical recordings. This ratio will not only depend on the size of the uEPSP in the spine, but also on the amount of VSD that is in the spine's plasma membrane as opposed to its internal membranes. Spines with high internal membrane content will have higher background VSD fluorescence, which will make the delta ΔF/F of the VSD dye smaller. We performed a noise analysis that allowed us to establish a reliable detection threshold for a "significant" optical uEPSP. For this analysis, we used the control trials, where no uncaging pulse was applied (see Methods, and Figures 2.4A and 2.4B); the photobleaching rate and noise between uncaging and control trials did not differ significantly. We established a detection threshold from the control trials that was equal to the mean VSD fluorescence plus 2x the standard deviation over a 5ms running average ($F_m + 2\sigma_{5ms}$). Thus in the uncaging trials, only transients that crossed this threshold and that occurred immediately following the uncaging event were counted as measurable optical uEPSPs. The optical uEPSPs that crossed this detection threshold were fit to an alpha-like function (see Methods) from which we determined the uEPSP's amplitude (Figure 2.3A, left panel) and duration (half-width) (Figure 2.3C) in the spine. Thus, the amplitude of 22 spine uEPSPs ranged from 4 to 18 mV with a mean of 10 mV. The duration of these spine uEPSPs ranged between 5 – 22 ms, with a mean duration of 11 ± 6 ms.

This analysis also allowed us to establish a minimum voltage that could have been reliably measured for those optical signals that were below our threshold criterion. For those recordings where the optical signal did not cross the F_m + $2\sigma_{5ms}$ detection threshold, we used $2\sigma_{5ms}/F_m$ as the minimum ΔF/F reliably detectable for a 5 ms interval (Figure 2.4B). We converted this threshold to voltage using the spine's bAP calibration, and this constitutes a minimum uEPSP amplitude that could have been reliably recorded in the spine; in other words, the spine uEPSP amplitude for the below-threshold recordings had to be less than this voltage (Figure 2.3A, right panel). On average, the minimum ΔF/F that we could reliably detect in the spine was 1.8 % (Figure 2.4B).

All of the data for the 52 spines we analyzed can be displayed as a cumulative uEPSP amplitude histogram (Figure 2.3B); these amplitudes could be as low as ~5 mV, and did not exceed ~20 mV. We did not observed a strong correlation with spine distance from the soma (up to 165 μm) in the amplitude of the spine uEPSP, nor in the spine to soma amplitude ratio, which was on average 22 (Figure 2.3D).

Because both the spine EPSP and soma EPSP amplitudes depend on the AMPA receptor currents evoked by uncaged glutamate, one should anticipate a direct relationship between these measured parameters. However, when we compared the spine and soma uEPSP amplitudes across all the multiple cells (Figure 2.3A)

we do not see an obvious correlation. A number of factors can combine to obscure a correlation, such as coincident spontaneous excitatory or inhibitory activity at other spines in the dendritic tree, variable dendritic filtering and variability in R_{neck}. As previously mentioned, we focused on proximal spines with 80% of the spines located < 75 µm from soma; therefore, we do not expect variability in dendritic filtering to be significant over such short distances (cf. Fig. 2.3D). We do, however, anticipate a strong connection between R_{neck} and the attenuation of the EPSP between the spine and the soma.

2.4 The spine neck resistance correlates with uEPSP amplitude in the spine

In order to study the effect of R_{neck} on the amplitude of the spine uEPSPs, we combined 2-photon VSDI, MNI-glu uncaging and FRAP of cytosolic Alexa Fluor 488. The FRAP experiment allows the measurement of the Alexa 488 equilibration time constant (τ_{eq}), which is determined by the diffusion barrier of the neck. Upon photobleaching, the Alexa 488 dye has to diffuse from the dendrite through the neck to replenish the fluorescence in the spine; a neck that is too narrow, or too long, or occluded with internal membranes will delay this process, and effectively increase the spine neck resistance. For these experiments, we filled the L5 pyramidal neurons with both VSD di-2-AN(F)EPPTEA and Alexa 488. After completing a complete set of measurements on a given spine to determine the spine and soma uEPSP, as described in the previous section, we applied a 0.5 ms pulse at 770nm on the target spine to

bleach the Alexa 488 (Figure 2.5A). The recovery of the Alexa488 fluorescence was monitored in the green channel for 600-1000 ms, and was fit to a single exponential from which the τ_{eq} was calculated. The histogram of τ_{eq} for n=33 spines (from multiple cells) from which we could evoke uEPSPs at the soma is shown in Figure 2.6A.

R_{neck} can be estimated from the relationship between $\tau_{eq,}$ the Alexa 488 diffusion coefficient, cytoplasmic resistivity and the spine head volume (*109*) (see Methods for details). Because the spine head is close to the resolution limit of the microscope, we developed an image-processing algorithm, which does not assume a given spine shape, to measure the spine volume from the Alexa488 z-stacks taken at 770 nm. This method is described in Figures 2.6C and 2.6D, and Methods. Briefly, it involves convolving the point spread function (PSF) of the microscope with a set of 3D binary images derived from the original spine image to find the best fit to the original spine intensity distribution (*121*); the volume could then be determined from this optimal 3D binary image. We contrasted this method with an alternative one that uses the total integrated fluorescence in the spine head to measure its volume, and observed that in most cases both methods agree quantitatively (Figure 2.6E).

Using the spine head volume, the Alexa 488 τ_{eq}, and a cytoplasmic resistivity of 150 Ω·cm (*80, 117, 118*) (see Methods), we estimated the R_{neck} for 33 spines from which we could evoke somatic uEPSPs (Figure 2.5B). Although the largest

value was over 1000 GΩ, the vast majority of the 33 spines had necks with resistance under 500 MΩ (mean=324; SD=217; median=250 MΩ). No correlation was found between somatic uEPSP and R_{neck} (Figure 2.5C) or between distance and R_{neck} for up to 170 µm from soma (Figure 2.6F). However, a strong positive correlation was found between spine uEPSP amplitude and R_{neck} (Figure 2.5D, Spearman's correlation $\rho = 0.83$, p-value = $4x10^{-4}$, n=14 spines). Furthermore, there was a weaker but still significant linear correlation between the uEPSP attenuation from spine to soma and R_{neck} (Figure 2.5E); the origins of the attenuation will be further discussed in the context of modeling results in the next section.

The positive correlation between spine uEPSP amplitude and R_{neck} (Figure 2.5D) may be due to a combination of passive and active (voltage-gated) mechanisms. To explore the possible contribution of the voltage-gated NMDAR to this enhancement, we performed four experiments in the presence of the competitive NMDA antagonist D-AP5 (500 µM applied through the extracellular pipette) (magenta points in Figures 2.5C, 2.5D and 2.6B). The presence of the drug did not show a strong effect in the amplitude of the uEPSPs in the spine or the soma, nor in the relation between spine uEPSP and R_{neck}. This suggests that if there are active conductances mediating the enhancement of the spine uEPSP by high R_{necks}, activation of NMDARs is not a major contributor. The possible involvement of other voltage-gated channels, such as voltage-gated sodium channels cannot be ruled out and should be further investigated. However, the absence of any

obvious positive curvature in the correlation of Figure 2.5D argues against the involvement of voltage dependent amplification of the spine EPSP. That R_{neck} is sufficient to produce the correlation shown in Fig 3D is corroborated by modeling results described in the following section.

2.5 Simulations of spine uEPSPs: synaptic conductance and uEPSP attenuation

We used NEURON (*120*) simulations of a morphologically realistic model of a L5 pyramidal neuron (*118*). We adapted the model of Hu et al. (*118*) to explore three questions: 1) what are the synaptic conductances associated with the spine uEPSPs that we have measured; 2) how strongly does variable R_{neck} contribute to the variation of uEPSP amplitude measured in the spine? and 3) what is the role of R_{neck} in the uEPSP attenuation at the soma and the dendrite. The model consisted of the target spine attached to a basal dendrite through a spine neck, and an exponential conductance transient at the spine head membrane to simulate synaptic activation. We used the model to predict the somatic potentials produced by the uEPSPs measured in each of the spines studied in the previous section (Figure 2.5). The dendritic diameter at the base of the neck, spine distance from soma, spine head diameter and spine neck resistance were all input to the model using the experimental data for each individual spine (Experiment section of Table 1).

When activated, the exponential synapse produces a change in conductance in the spine head that is governed by two parameters: maximum conductance (g_{syn}), and decay time constant (tau). A parameter search was done to find the best combination of g_{syn} and tau that could reproduce the amplitude and the duration of the experimental uEPSP in each spine (Figure 2.7A, and Figure 2.8). From these simulations, the range of values that could reproduce the experimental results were between 0.4 – 1.2 nS (mean 0.8 ± 0.2, n=14 spines) for the synaptic conductance, and 5 – 23 ms (mean 10 ± 6 ms, n=14 spines) for the decay time constant tau (Model section in Table 1). Although g_{syn} was the result of a fit to the uEPSP measured at the spine, the values are comparable to the values reported in the literature from voltage clamp recordings of miniature excitatory post synaptic currents (*122-124*), thus supporting the validity of the model.

Figure 2.7B shows an example of the voltage spread along the dendritic cable 2 ms after the activation of the exponential synapse on the target spine #11 in Table 1. The simulated uEPSP at the soma was a direct prediction of the model for each spine and is compared to the experiment in Figure 2.7C. How the spine to soma amplitude ratio depends on R_{neck} is plotted in Figure 2.7D; the same positive correlation was observed as in the experiments (Figure 2.5E) and the model, showing that large R_{neck} does increase the amount of uEPSP attenuation at the soma. Figure 2.7E compares the spine to soma uEPSP amplitude ratio in the experiments versus the model; a remarkably similar mean ratio of 23 was

obtained in both cases (23.4 in the experiments and 22.7 in the model), however, a broader range was observed in the experiments (SD in the experiments = 13, SD in the model = 8.5), which could be due to cell-to-cell variability present in the experiments, and not in the model. Overall, the strong correspondence of the predicted spine to soma attenuation with the experimentally measured values further suggests that the model captures the key biophysical mechanisms of the system. We can conclude from this that the lack of correlation between the spine and soma uEPSP (Figure 2.3A) is due to the variability in how the input current at the spine is processed as the resultant voltage signal propagates to the soma. This variability is largely accounted for by the variable experimentally-derived features - dendritic diameter at the base of the neck, spine distance from soma, spine head diameter and spine neck resistance – that are explicitly included in the model calculations for each of the model simulations.

We then used the simulations to estimate the amplitude and duration of uEPSPs in the parent dendrite in comparison to the measured uEPSP in the corresponding spine. The dendritic amplitude at the base of the neck ranged between 1.5 – 8.7 mV (mean 3.8 ± 2.1 mV, n=14 spines), with durations between 7- 31 ms (mean 15 ± 7, n=14 spines) (Table 1). In these simulations, the average voltage drop (ΔV) between the spine and the dendrite was 8.6 ± 3.8 mV, whereas the average ΔV from dendrite to soma was 3.2 ± 2.1 mV. This shows that most of the voltage drop occurs through the spine neck, demonstrating that

the spine is an electrical compartment and emphasizing the important role of the spine neck resistance.

2.6 Discussion

In this study, we used 2-photon glutamate uncaging with voltage-sensitive dye recording to directly measure the characteristics of uncaging-evoked EPSPs in proximal (< 170 µm from soma) spines on basal dendrites of cortical L5 pyramidal neurons. We investigated their amplitude and duration in the spine, as well as their attenuation at the soma. By combining this technique with FRAP of a cytosolic dye in the same spine, we were able to estimate the spine neck resistance and study the role of the spine neck in the amplitude and attenuation of these uEPSPs. We believe this is the most direct study of these 2 key variables

Glutamate uncaging has been widely used to evoke unitary (single synapse) post-synaptic responses that resemble miniature EPSPs at the soma (*125*). mEPSPs are the postsynaptic responses to probabilistic quantal release, and are usually < 1 mV in amplitude at the soma for these cells (*126*); we were careful, by adjusting the intensity of the uncaging laser, to make sure that the somatic uEPSPs that we evoked were in the range of physiologically observed mEPSPs (Figure 2.3).

We succeeded in measuring (Figure 2.3) uEPSP amplitudes that ranged between 4 to 18 mV (mean = 10 mV) in 22 single spines of different sizes and morphologies. In addition, there were 30 experiments that showed uEPSPs in the soma, but had signals in the spine that were below our detection limit; therefore, the actual average spine uEPSP is likely to be significantly lower than 10mV (Fig. 2.3A, right panel and Figure 2.3B). The half width of uEPSPs in the spines ranged between 5 to 22 ms (Fig. 2.3C), significantly faster than somatic EPSPs and also contrasting with glu-evoked spine Ca^{2+} signals that typically last for ~50 ms or longer (*21, 104*).

The diffusional relaxation time in spines has been previously measured using FRAP or photoactivation experiments, but has led to different conclusions as to whether R_{neck} could be large enough to make the spine an electrical as well as a biochemical compartment (*86, 109*). To use such measurements to determine the diffusional (and therefore the electrical) resistance of the neck also requires an estimate of the volume of the spine head, which is challenging because the spine head is typically near the resolution limit of the 2-photon microscope. To solve this problem, we devised an analysis and calibration of the 3D 2-photon images of the spines (Figure 2.6). Using FRAP measurements of cytosolic Alexa 488 combined with these measurements of the spine head volume, and assuming a cytoplasmic resistivity of 150 Ω·cm, we estimate R_{neck} values (Fig. 2.5B) with an average of 324 MΩ for 33 spines. These large R_{neck} values support previous theoretical hypotheses that spines can act as high-impedance input

compartments (*5, 96*), although the large variability from our estimates suggest that not all spines behave in the same way.

Therefore, to directly assess the influence of R_{neck} on the spine uEPSP, we measured the R_{neck} in a subset of 14 spines from which we could also determine uEPSP. We observed a significant positive correlation between the spine uEPSP and the spine R_{neck} (Figure 2.5D), which corroborates previous theoretical predictions that large neck resistances can enhance the EPSP within the spine head (*127*). Due to the lack of any obvious positive curvature in the correlation indicative of activation of positive feedback through voltage-dependent channel opening, we believe that this dependence of the EPSP amplitude by R_{neck} is mainly mediated by passive mechanisms, at least for R_{necks} up to ~440 MΩ. Moreover, in a few experiments performed in the presence of the NMDAR blocker D-AP5, we did not observe an apparent effect of the drug on the spine uEPSP amplitudes, nor on its relation to the spine R_{neck}. This suggests that NMDARs did not contribute substantially to the enhancement of the spine EPSP by large R_{neck}, at least within the ranges of amplitudes measured here.

Based on the experimentally measured amplitude and duration of the spine uEPSPs, the estimated R_{neck} for each spine, and the dendritic diameter at the base of the neck, we were able to recapitulate the uEPSP dynamics in the spine and its attenuation at the soma using a morphologically realistic model of a L5 pyramidal neuron (Figure 2.7 and Table 1). From these simulations, we found

that the average synaptic conductance associated with these uEPSPs is 0.8 ± 0.2 nS for the 14 spines for which we were also able to measure R_{neck}. Somatic voltage-clamp recordings in hippocampal slices of unitary mEPSCs have been used to estimate a g_{Syn} ranging from 0.2 to 2 nS (*124*). Thus, we feel that the g_{syn} values estimated from the experimentally derived spine uEPSPs are realistic.

The attenuation ratio of the spine to soma uEPSP is a model prediction that can be directly compared to the experimental data. We found that the average attenuation ratio was nearly identical for the model and the experimental data: 22 vs. 23, respectively. We also found a correlation between the attenuation ratio and R_{neck} in both the experiments (Fig. 3E) and model (Fig. 4D); the linear fits had remarkably similar slopes, 0.05 and 0.06 (ratio/MΩ), respectively, although the experimental correlation showed significantly more scatter, presumably due to cell to cell variability. Overall, the model predictions and the experimental results produce a self-consistent picture, further supporting our conclusion that active processes are not required to explain the uEPSPs measured in single spines.

From the model it was also possible to assess the uEPSP amplitudes at the parent dendrite adjacent to the target spine. The mean dendrite to soma amplitude ratio that we found was 7.2 ± 4.5 for positions that are on average 70 µm from soma. This average ratio agrees with previous measurements of unitary synaptic events made through dendritic patching at similar locations on the basal

dendrites of L5 pyramidal neurons (*27*). By comparing the voltage drop between the spine and the parent dendrite, and between the dendrite and the soma, we found that most of the attenuation of the EPSP occurs when it travels through the spine neck. Taken together, our results show that spines can act as electrical compartments capable of electrically isolating the synaptic input from other synapses, as well as controlling the effectiveness of charge transfer from the synapse into the dendrite and the soma.

To summarize, our results for spine EPSPs and neck resistances are in the low end of the range of values estimated by more indirect approaches (*80, 86, 87, 106*). It is clear that the spine can serve as an electrical compartment, but the amplitudes that we measure for the EPSP in the spine that produce miniature somatic EPSPs are insufficient to produce active amplification of the voltage signal. On the other hand, inputs to several neighboring spines may be integrated in the adjacent dendrite to produce local spikes that can feed back to activate voltage dependent channels in the spines. The approaches described in this paper can be extended to explore these intriguing possibilities.

AUTHOR CONTRIBUTIONS

EH designed and performed the experiments and wrote the manuscript; CDA designed and performed the experiments and reviewed the manuscript. LML designed the experiments and wrote the manuscript.

ACKNOWLEDGEMENTS

We are grateful to Dr. Ping Yan who prepared and supplied the VSD used in this work. We thank Dr. Boris Slepchenko, Dr. Ann Cowan, Dr. Igor Novak and Frank Morgan for useful discussions. Dr. Srdjan Antic provided helpful comments on the manuscript. This work was supported by National Institutes of Health grants R01 EB001963 and P41 GM103313.

Figures

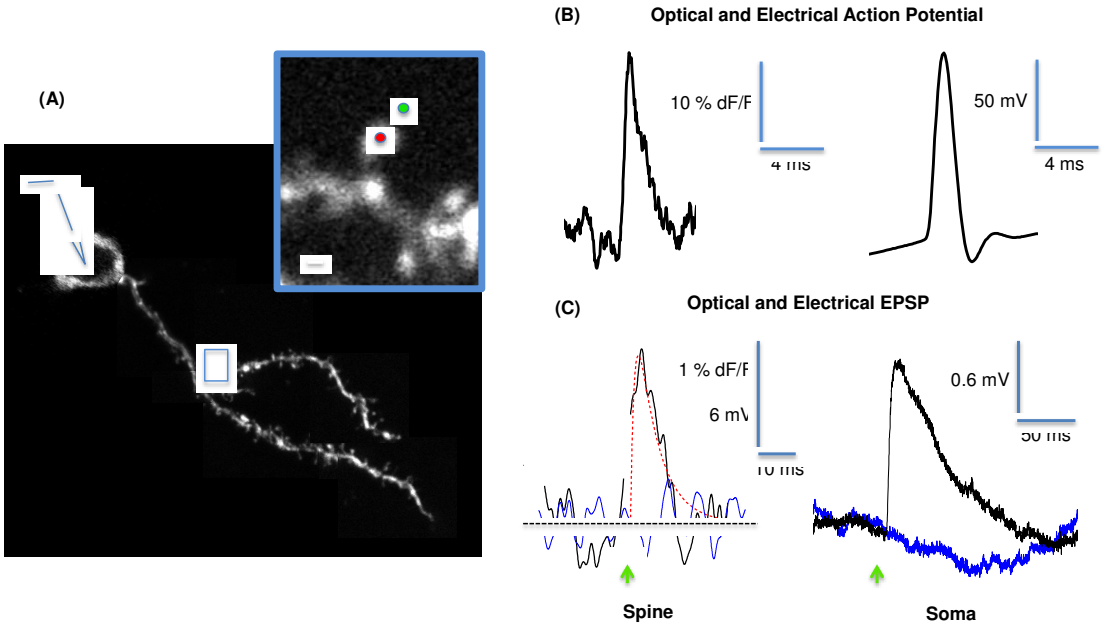

Figure 2.1. Simultaneous 2-photon voltage-sensitive dye imaging (VSDI) and MNI-Glutamate uncaging in a single spine. (A) Z-stack of a basal dendrite from a L5 pyramidal neuron filled with the VSD di-2-AN(F)EPPTEA (aka PY3243) and whole-cell patched at the soma. *Inset*: Single spine showing the targeting positions for the uncaging laser (green dot, 0.5 ms uncaging pulse at 750 nm), and for the VSD excitation laser (red dot, set at 1060 nm). Scale bar: 0.5 µm. (B) Action potential evoked by somatic current injection (400 pA for 35 ms) recorded optically (left) in the spine, and electrically at the soma (right). Traces are average of n=6 action potentials. (C) *Left:* VSD fluorescence over time in the same spine as in (B) for uncaging (black line) and interleaved control trials (blue line), where no uncaging pulse was applied. Green arrow represents the uncaging time. The 0.5 ms long uncaging artifact was removed from the

recordings offline (see Methods). Red dotted line corresponds to the fit of the optical uncaging EPSP (uEPSP, see Methods). *Right:* Corresponding electrical signal at the soma for the uncaging (black), and control trials (blue). The optical and electrical recordings are average of n=30.

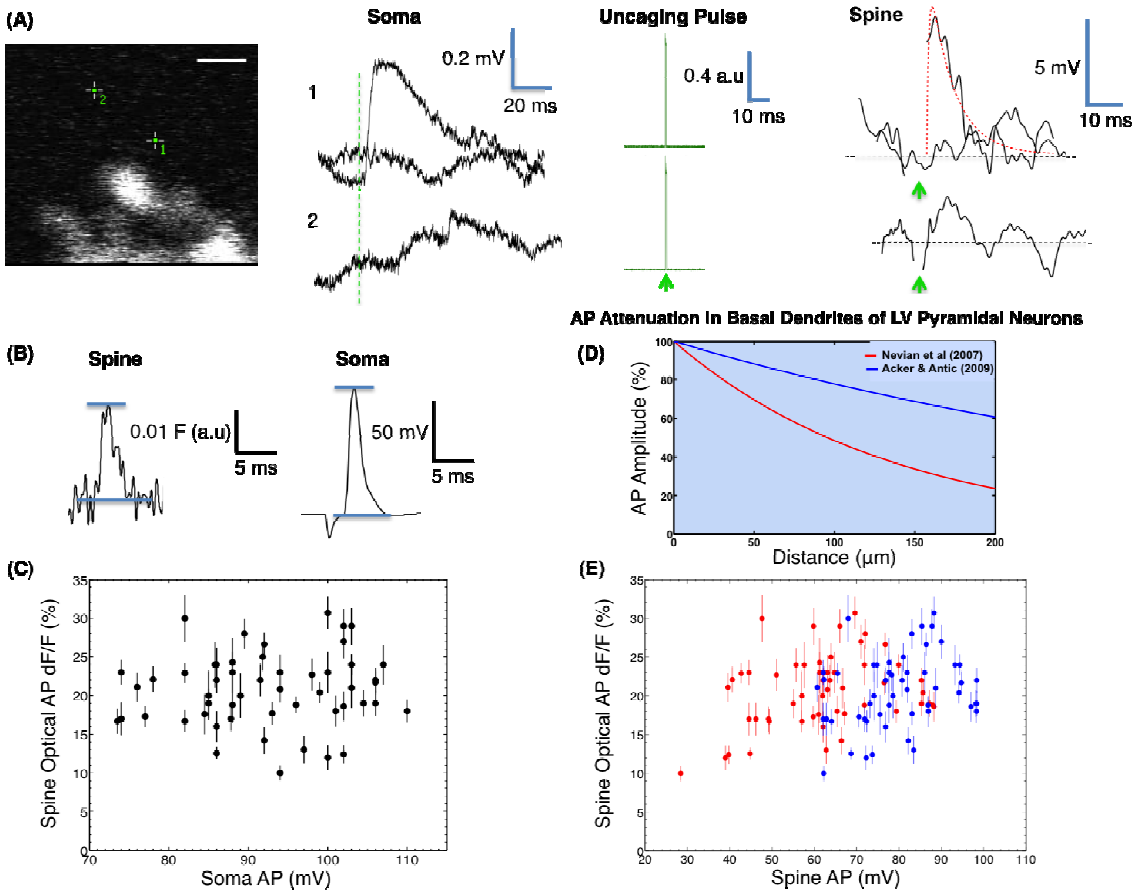

Figure 2.2. Uncaging targeting and calibration of optical uEPSPs in single spines. (A) Representative spine showing the response to glutamate uncaging from two different targeting positions, 1 and 2. Scale bar in the image is 1 µm. Top and bottom panels correspond respectively to uncaging from 1 (n=26) and 2 (n=10). From left to right the traces correspond to: average electrically recorded somatic responses to the uncaging pulses (uncaging time denoted with green dotted line). The average response to control pulses, where the uncaging beam was off, is also shown on the top panel. The next traces show the intensity of the uncaging pulse measured as the fluorescence of the extracellular Alexa488

(green channel) that was applied along with the MNI-Glutamate via an extracellular pipette (see Methods). The right most traces show the VSD fluorescence (red channel) in the spine head during uncaging and control trials (top), and during uncaging only (bottom). The uncaging time is denoted by the green arrow. Red dotted line is the fit of the optical uEPSP. (B) *Left:* VSD fluorescence over time for a representative spine showing the amplitude of the optical action potential (AP), which was measured as the difference between base line and peak value. *Right:* corresponding electrical AP recorded at the soma. Both traces are average of n=6 APs. (C) Summary of the data for n=52 spines from 34 different cells, showing the amplitude of the optical AP in each spine (ΔF/F) as a function of the AP amplitude at the soma. Error bars correspond to the mean std of the binned time course (0.5 ms bins, 120 ms recording time); each time course was an average of 5 to 10 APs. All experiments were done at room temperature. (D) Attenuation of the back-propagating AP as a function of distance from soma in basal dendrites of L5 pyramidal neurons. Two different length constants of bAP attenuation have been previously reported: Acker *et al (116)* reported a length constant of 400 μm (blue), and Nevian *et al* (*27*) reported a steeper attenuation constant of 138 μm (red). (E) AP amplitude in each spine in mV (x-axis) calculated based on the distance of the spine from the soma, the amplitude of the somatic AP, and the two different reported attenuation length constants shown in (D). From this amplitude and the amplitude of the optical AP (y-axis), we determine the VSD sensitivity (ΔF/F per mV) in each spine.

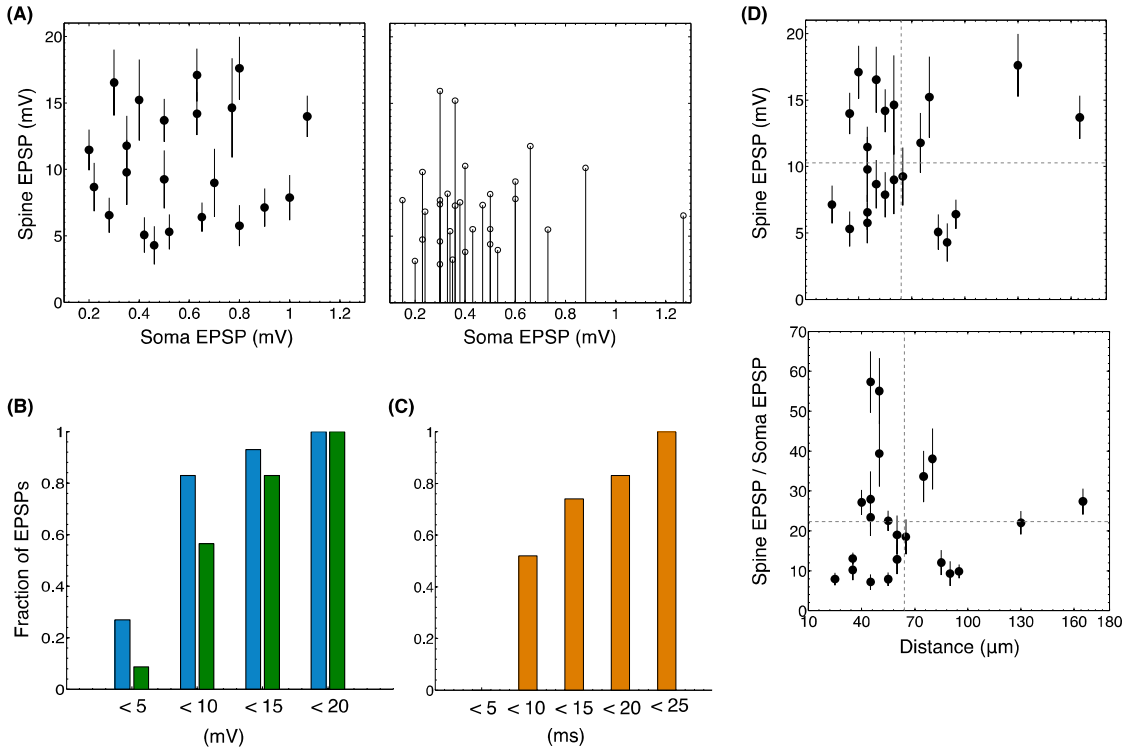

Figure 2.3. Uncaging EPSPs (uEPSPs) in single spines. (A) *Left:* Scatter plot showing the amplitude of uEPSPs in the spine versus the soma for the optical uEPSPs above the $F_m + 2\sigma_{5ms}$ detection threshold. Error bars correspond to mean standard deviation from time-series data. *Right:* Stem plot showing the $2\sigma_{5ms}/F_m$ amplitude in mVs for optical uEPSPs that failed to exceed the detection threshold (see text and Figures 2.4A and 2.4B). Both panels combined correspond to n=52 spines across 34 different cells. Optical uEPSPs in this figure were calibrated using an attenuation length constant for the bAP of 400 µm. uEPSPs calibrated based on an attenuation length constant of 138 µm are shown in Figure 2.4. (B) Cumulative histogram of the spine uEPSP amplitudes for recordings above the $F_m + 2\sigma_{5ms}$ detection threshold (green, n=22 spines) and

below (blue, n=30 spines) the $F_m + 2\sigma_{5ms}$ detection threshold. (C) Cumulative histogram of the spine uEPSP half-widths for recordings above detection threshold. (D) Spine uEPSP amplitude (*Top*) and spine to soma amplitude ratio (*Bottom*) as a function of spine distance from soma, for the n=22 spines where the optical uEPSP crossed the detection threshold. Dotted lines indicate mean values.

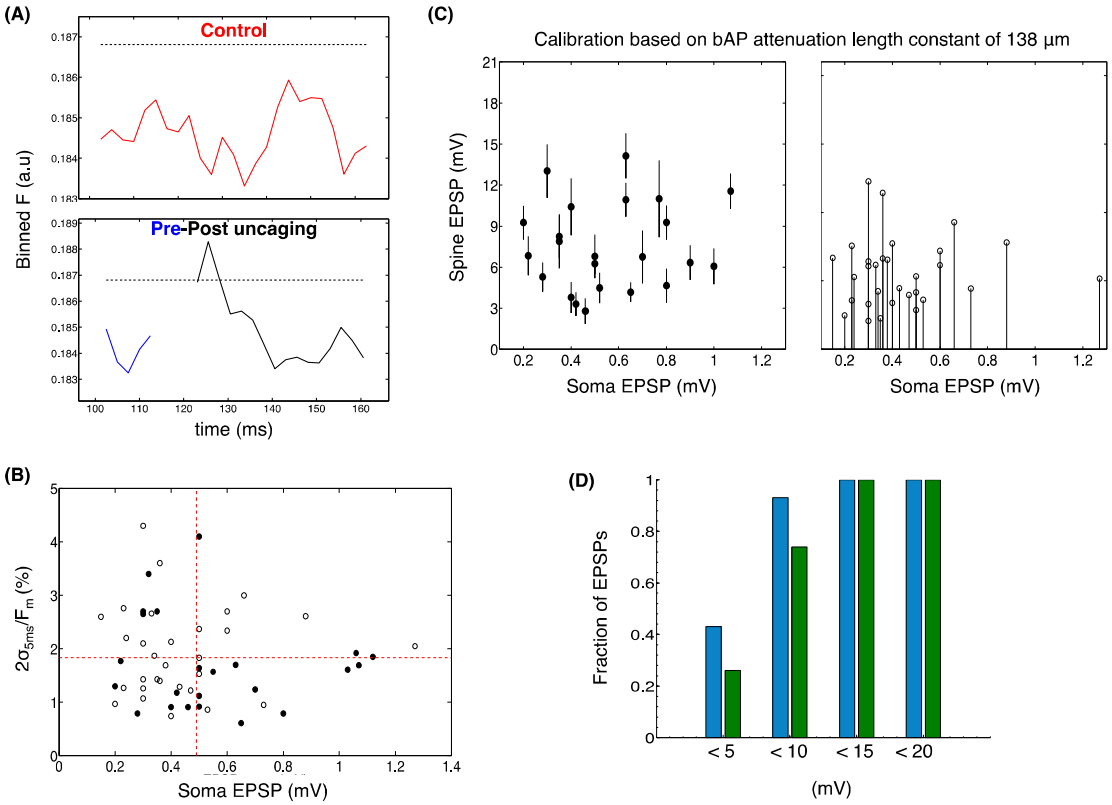

Figure 2.4. Noise analysis and uncaging EPSPs (uEPSPs) in single spines calibrated using a bAP attenuation length constant of 138 µm. (A) VSD fluorescence over time for a representative spine. Top trace corresponds to control trials (where no uncaging pulse was applied), and bottom trace to the interleaved uncaging trials (where a 0.5 ms uncaging pulse at 750 nm was applied). For this particular case, each time course (control and pre-post uncaging) is an average of 5 sweeps. Traces are binned with a moving average of 5 ms. Dash line shows the detection threshold for an optical uEPSP, defined by the mean fluorescence plus 2x the standard deviation (F_m + $2\sigma_{5ms}$) from control trials. (B) $2\sigma_{5ms}/F_m$ (y-axis) from control trials for the n=52 spines from

which an uEPSP at the soma could be evoked (x-axis). $2\sigma_{5ms}/F_m$ represents the minimum ΔF/F reliably measured in each spine. Filled and unfilled dots correspond, respectively, to optical uEPSPs that crossed and did not cross the $F_m + 2\sigma_{5ms}$ detection threshold. Red dotted lines correspond to mean values. (C) Scatter and stem plots (as in Figure 2.3) of the spine uEPSP amplitude calibrated based on a bAP attenuation length constant of 138 μm (*27*). (D) Cumulative histogram spine uEPSP amplitudes calibrated using a length constant of bAP attenuation of 138 μm. Blue and green bars correspond, respectively, to measurements below (n=30 spines) and above (n=22 spines) the detection threshold.

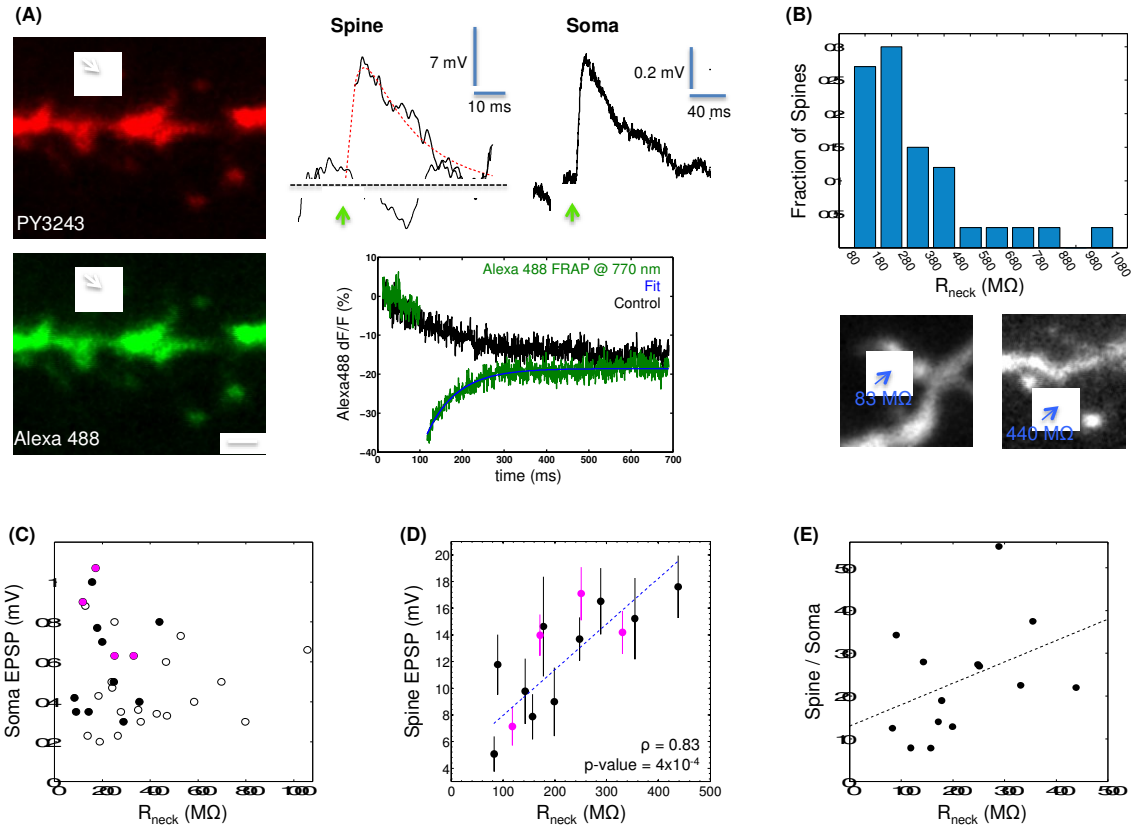

Figure 2.5. Effect of R_{neck} on the Spine uEPSP Amplitude. (A) *Left:* Collapsed z-stack (taken at 770 nm) of a dendritic segment from a cell filled with both PY3243 and cytosolic Alexa488. The arrow points at the target spine for simultaneous glutamate uncaging and VSDI (red channel), and for subsequent FRAP of Alexa488 at 770 nm (green channel). Scale bar= 1 µm. *Right Top:* Optical VSD signal in the spine for uncaging and control trials, and corresponding somatic uEPSP (n=10). *Right Bottom:* FRAP experiment in the same spine, showing the recovery of the Alexa488 fluorescence after a 0.5 ms photobleaching pulse (green trace, n=1). Black trace corresponds to control, where no photobleaching pulse was applied, and blue trace to the exponential fit of the fluorescence

recovery. (B) *Top:* Histogram of estimated R_{necks} for n=33 spines from which somatic uEPSPs could be evoked. *Bottom:* z-stacks of two representative spines showing the difference in morphology and the estimated R_{necks}. (C) Soma uEPSP versus R_{neck} for the n=33 spines in (B). Filled and unfilled dots correspond, respectively, to measurements above and below the detection threshold for an optical uEPSP. Black dots correspond to experiments in the absence of drugs, and magenta dots to experiments in the presence of 500 μM of D-AP5 in the extracellular pipette. (D) uEPSP amplitude in the spine versus R_{neck} for those spines where the optical uEPSP crossed the detection threshold (n=14). Error bars correspond to the mean standard deviation. Blue dotted line is the weighted linear regression $y = 0.034*x + 4.5$ (Adjusted $R^2 = 0.62$). (E) Spine to soma uEPSP amplitude ratio for the spines in (D). Black dotted line corresponds to the linear fit $y= 0.05*x + 13$ (Adjusted $R^2 = 0.1$).

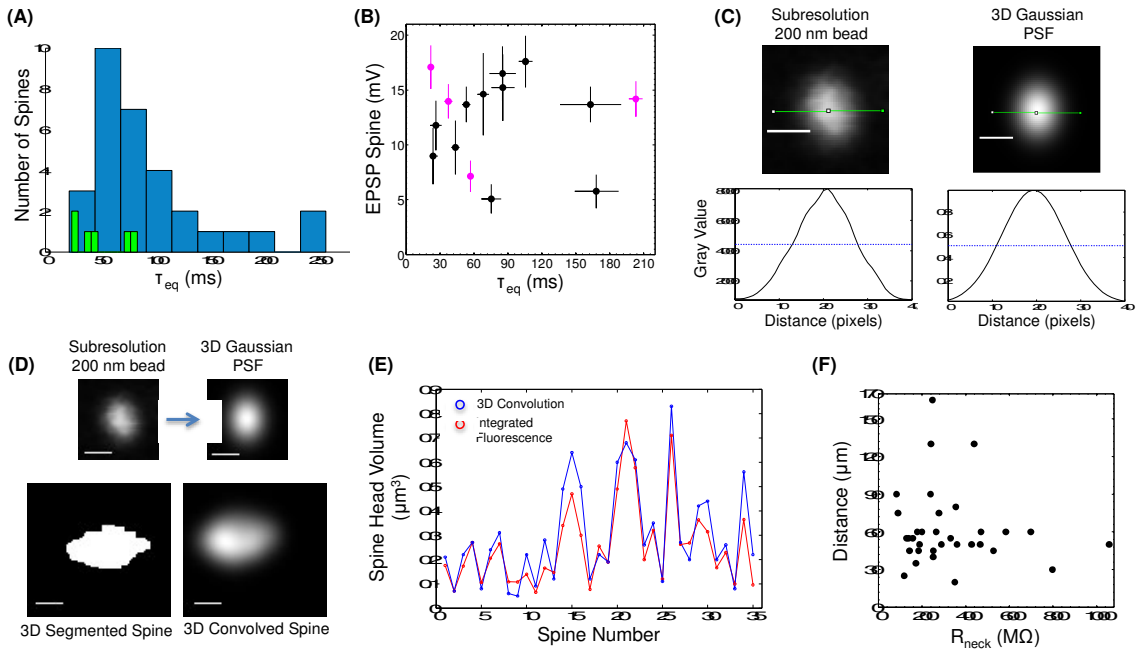

Figure 2.6. FRAP equilibration time constants and spine head volume measurement. (A) Histogram of Alexa488 equilibration time constants (τ_{eq}) for mushroom-like spines (blue bars, n=27/33) and stubby spines (green bars, n=6/33). (B) Spine uEPSP amplitude versus τ_{eq} for the n=14 spines where the optical uEPSP crossed the detection threshold. Magenta dots correspond to experiments in the presence of D-AP5. Error bars correspond to 95% confidence interval in the exponential fit of the FRAP signal (x-axis), and mean std of the VSD signal (y-axis). (C) *Top left:* z-stack of a 200 nm subresolution fluorescent bead, from which the PSF of the microscope at 770 nm was measured. The PSF half widths were 0.422 μm in x, 0.526 μm in y, and 1.16 μm in z. *Top right:* 3D Gaussian PSF generated with the same xyz dimensions as the experimental PSF (see Methods). Scale bar = 0.5 μm. Green line shows the ROIs from which the fluorescence profiles shown under each image were measured. The blue

dotted line in these profiles corresponds to the half-width. (D) Description of the 3D convolution method used to measure the spine head volume (see Methods). All images are collapsed z-stacks. *Top left:* z-stack of a 200 nm subresolution fluorescent bead, from which the PSF of the microscope at 770 nm was measured. The PSF half widths were 0.422 µm in x, 0.526 µm in y, and 1.16 µm in z. *Top right:* 3D Gaussian PSF generated with the same xyz dimensions as the experimental PSF. *Bottom left:* z-stack of the segmented spine head, and scaled to the ratios of the PSF half widths: x-scale = 1, y-scale = 0.8, z-scale: 0.36. *Bottom right:* z-stack of the convolved spine head resulting from doing 3D convolution between the segmented-scaled z-stack of the spine and the 3D Gaussian PSF. Scale bar 0.5 µm. (E) Comparison of the spine head volume measured with two different methods (see Methods) for n=35 spines: total integrated fluorescence (red) and 3D convolution (blue). (F) Relationship between R_{neck} and distance from soma for the 33 spines from which somatic uEPSPs could be evoked.

Table 1. NEURON Simulations of Spine uEPSP

	Experiment						Model			
Spine #	**Distance (µm)**	**Spine Head Diameter (µm)**	**R_{neck} (MΩ)**	**Spine EPSP Amplitude (mV)**	**Spine EPSP FWHM (ms)**	**Dendritic Diameter (µm)**	**Synaptic Conductance (nS)**	**Synaptic tau (ms)**	**Dendritic EPSP Amplitude (mV)**	**Dendritic EPSP FWHM (ms)**
1	25	1.0	118	7	10	0.9	0.9	9	1.5	24
2	35	0.7	171	14	7	0.8	1.2	8	4.1	12
3	40	0.6	251	17	7	0.6	1.1	7	3.3	11
4	45	0.7	143	10	8	0.7	0.8	8	2.7	12
5	50	0.8	289	16	6	0.7	0.9	5	2.6	8
6	55	1.0	331	14	9	0.7	0.8	11	1.5	21
7	55	0.8	157	8	20	0.8	0.6	20	2.7	31
8	60	0.9	178	15	10	0.6	1.1	11	4.3	14
9	60	0.6	199	9	7	0.8	0.7	8	2.4	11
10	75	0.8	90	12	6	0.8	0.9	5	6.3	7
11	80	0.7	354	15	7	0.7	0.6	8	3.4	10
12	90	0.7	83	5	6	0.7	0.5	5	3.3	7
13	130	0.8	438	18	15	0.8	0.7	15	6.5	18
14	165	1.2	248	14	22	0.7	0.4	23	8.7	23
Mean ± std	69 ± 38	0.8 ± 0.2	218 ± 106	12 ± 4	10 ± 5	0.7 ± 0.1	0.8 ± 0.2	10 ± 6	3.8 ± 2.1	15 ± 7

Table 1. The Experiment section of the table shows the experimental parameters that were input to the model for the simulation of the uEPSP in each of the 14 spines in Figure 2.5. The parent dendrite in the model was divided into 10 μm long segments; the dendritic diameter of the segment at the base of the neck was set to the average dendritic diameter for 10 μm measured from the Alexa 488 z-stacks of the spine and parent dendrite. The Model section shows the output of the model from the simulation of each spine, using the best combination of g_{syn} and tau that could reproduce the spine uEPSP amplitude and duration.

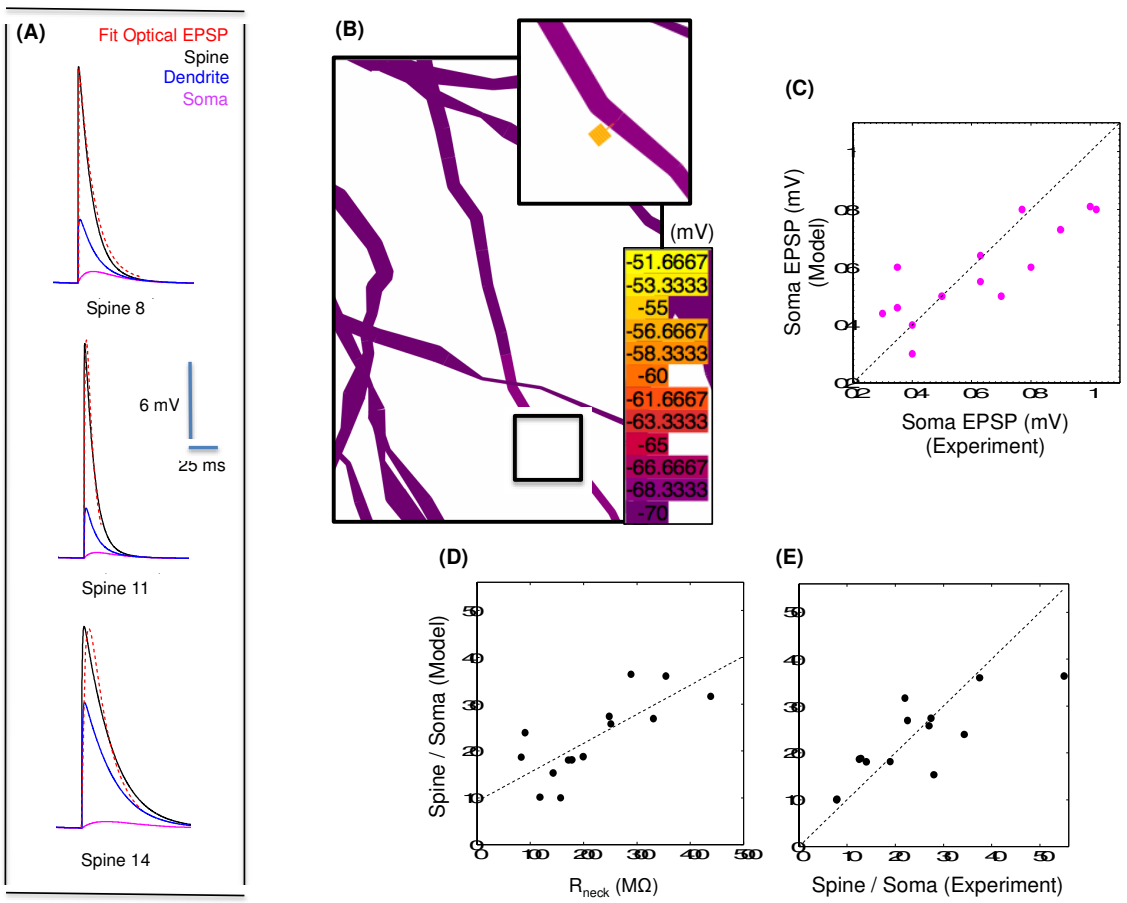

Figure 2.7. Model simulations. A morphologically realistic multi-compartmental model of a L5 pyramidal neuron was used (see Methods, model based on Hu *et al (118)*). The passive electrical properties of the model were R_m: 30,000 Ω cm^2, C_m: 1 μF cm^{-2}, and R_i: 150 Ω cm. The resulting somatic input resistance was 30 MΩ. (A) Three different examples showing the time course of membrane voltage in 3 different compartments (spine, parent dendrite and soma) before and after activation of an exponential synapse on spines #8, #11 and #14 in Table 1. The red dotted trace corresponds to the fit of the optical uEPSP in the spine. The dendritic voltage is recorded at the base of the neck. (B) Representative example of a simulation showing the target spine connected to a basal dendrite through

the spine neck. The heat map corresponds to the membrane voltage 2 ms after the activation of the exponential synapse on spine #11 in Table 1. (C) Somatic uEPSP in the experiments versus that predicted by the simulations for the n=14 spines in Figure 2.5. (D) Spine to soma uEPSP amplitude ratio predicted by the model versus the spine R_{neck} for the same spines as in panel (C). Black dotted line corresponds to the linear fit y=0.06*x+9.3 (Adjusted R^2 = 0.6). (E) Spine to soma uEPSP amplitude ratio in the experiments versus the model for the same spines as in panels (C) and (D).

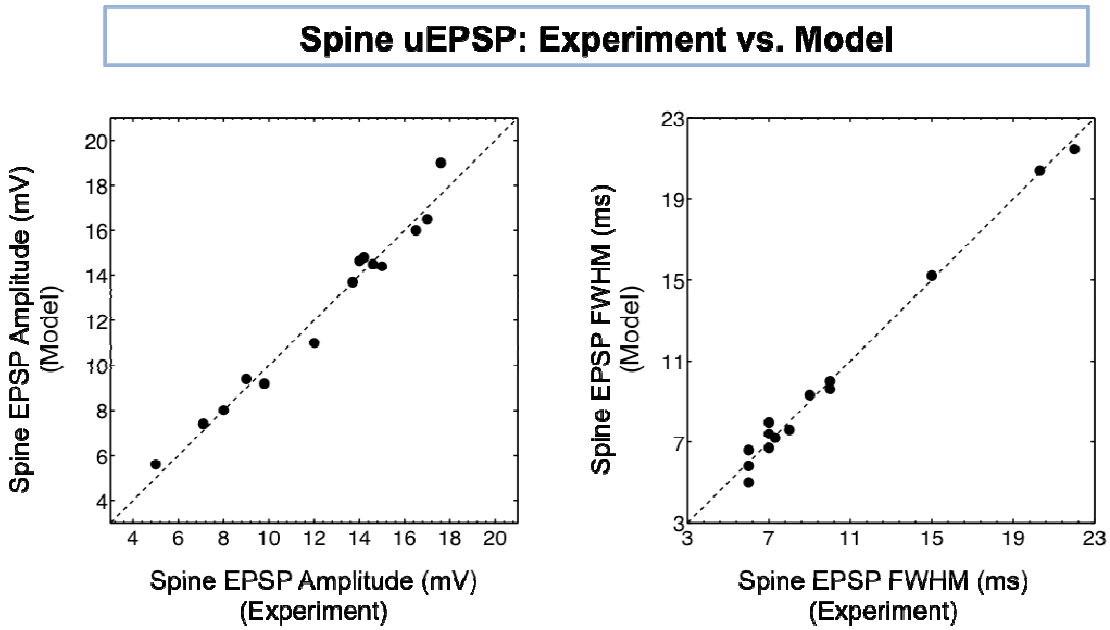

Figure 2.8. Spine uEPSP in the experiment versus the model. Plots showing the fit of the spine uEPSP amplitude (*left*) and duration (*right*) by the model, after a parameter search for the best combination of g_{syn} and tau that could reproduce the uEPSP in each of the 14 spines in Table 1.

Chapter 3

Modeling EPSPs in Single Spines: Interplay between Spine Neck and Dendritic Resistance

3.1 Introduction

In the previous chapter we saw that it was possible to simulate the uEPSP in the spine by using a compartmental model of a realistic morphology of a L5 pyramidal neuron. In those simulations, it was important to take into consideration the dendritic diameter in order to correctly simulate the EPSP amplitude ratio between the spine and the soma. In this chapter, we expand on this interaction between the spine neck resistance (R_{neck}) and the dendritic resistance (R_{dend}) in order to study how they both affect the EPSP amplitude and attenuation locally, and at the soma. We start with simulations of a single spine, and then we look at multiple clustered spines receiving synchronous synaptic input.

3.2 Compartmental Modeling of Spine EPSPs in L5 Pyramidal Neurons using NEURON

The NEURON simulation environment (*120*) allows the construction of morphologically realistic quantitative models of neurons, in order to study the spatial spread of membrane currents. It numerically solves the cable equation

developed by Rall, which is the mathematical description of the relationship between current (*I*) and voltage (*V*) in thin dendrites in one dimension (*128*):

$$\frac{\partial^2 V}{\partial x^2} = \frac{\partial V}{\partial t} + I(V,t)$$

The spatial discretization employed by NEURON reduces this partial differential equation to a set of connected compartments, producing a family of ordinary differential equations of the form:

$$\sum_k \frac{v_k - v_j}{R_{jk}} = c_j \frac{dv_j}{dt} + i_{ion_j}$$

In this set of equations, the net transmembrane current leaving compartment *j* is equal to the sum of the axial currents entering the compartment. The right hand side of the equation is the sum of the capacitive and ionic components, where c_j is the capacitance of the compartment, and i_{ionj} includes all currents through membrane ion channels. The left hand side of the equation is the sum of the axial currents that enter the compartment from all its neighbors, where v_k is the voltage in the neighboring compartment, and R_{jk} is the longitudinal resistance connecting both compartments.

It is possible to specify 3D geometries in NEURON based on anatomical reconstructions of real neurons. NEURON divides this morphology into sections

connected to each other, each with its own anatomical and biophysical properties. Several morphologically realistic models based on Neurolucida reconstructions of L5 pyramidal neurons have been published. All of these models incorporate passive and active conductances found in these cells, such as leak conductance, VGSCs, VGCCs, voltage-gated K^+ channels (VGKC), and calcium-gated potassium channels. The general approach is to generate a biophysical model of each type of channel, and incorporate it into the neuron model with a given density, so that it reproduces the experimentally observed behavior. For example, Nevian et al (*27*) found that the sodium dendritic spikes evoked by direct current injection on basal dendrites, as well as the bAP profile could be best fit by a model that incorporated nonhomogeneous distributions of VGSCs, such as a linear (proximal-distal) decaying gradient or a hot spot, combined with a homogeneous distribution of voltage-gated potassium channels. A similar distribution of VGSCs on basal dendrites was found in the best-fit model of the bAP decay by Acker et al (*116*), however in this model a nonuniform (increasing) distribution of the A-type potassium conductance was also predicted. The discrepancy between these two models could be attributed to the difference in the amount of attenuation of the bAP with distance that they reported.

An alternative model of a L5 pyramidal neuron that takes into consideration two distinct types of VGSCs found in these cells has also been previously published (*118*). Here, the low-threshold Na_v 1.6 channel is dominant in the axon, and distal axon initial segment (AIS), whereas the high-threshold Na_v 1.2 channel is present

in the soma, dendrites and proximal AIS. This is based on the observation that Na_v 1.6 channels determine the lowest threshold for the AP initiation at the distal AIS, whereas activation of Na_v 1.2 channels promotes the AP backpropagation. In this model, the density of the Na_v 1.2 conductance in the somatodendritic compartment is set to 80 pS μm^{-2}, and the density of the Na_v 1.6 in the axon and nodes of Ranvier is set to 300 pS μm^{-2} and 1600 pS μm^{-2}, respectively. This model also includes the fast voltage-gated K^+ current I_{Kv} (20 pS μm^{-2} in the soma, 10 pS μm^{-2} in dendrites, and 1500 pS μm^{-2} in the axon), the slow non-inactivating K^+ current I_{km} (0.3 pS μm^{-2} in soma and dendrites), the high-voltage activated Ca^{2+} current I_{Ca} (0.3 pS μm^{-2} in soma and dendrites), and the Ca^{2+}-dependent K^+ current I_{KCa} (3 pS μm^{-2} in soma and dendrites). The density of the background leak conductance is 0.33 pS μm^{-2}, and the reversal potential of this leak current is -70 mV. Other passive electrical properties are: membrane capacitance, axial resistivity and specific membrane resistivity of 1 $\mu F\ cm^{-2}$, 150 Ω cm, and 30,000 $\Omega\ cm^2$, respectively. Since this model specifically implements the biophysical properties of the VGSCs found in L5 pyramidal neurons, such as voltage-dependence and kinetics, it will be used in this chapter as in Chapter 2 to study the interplay between the spine neck and the dendritic axial resistances on the propagation of the EPSP from the spine to the parent dendrite and the soma. To gain insight on the contribution of these resistances alone, in the first set of simulations the density of the Na_v 1.2 channel conductance will be constant throughout the basal dendrite (80 pS μm^{-2}). In the last section of this chapter, the

effect of a gradient in the Na_v 1.2 channel density along the basal dendrite will be studied for clustered spines receiving synaptic input synchronously.

To simulate a spine, a compartment corresponding to the spine head with a specified diameter is attached to a basal dendrite through a compartment called the spine neck (Figure 3.1). Unless otherwise stated, the densities of the passive and active conductances in the spine head and the neck are identical to those of the parent dendrite. In all simulations, the spine head and the neck are each treated as single compartments, but the basal dendrite to which they are connected is divided into segments of 10 µm in length each. In this way, it is possible to calculate the longitudinal resistance of the parent dendrite along the 10 µm long segment at the base of the neck (see below). An exponential synapse with a reversal potential of 0 mV is connected to each spine head through the NetCon function in NEURON, which allows a connection between a source (the stimulus) and a target (the spine). This synapse generates a change in conductance in the spine head governed by two parameters: a maximum synaptic conductance (g_{syn}) and a decay time constant (tau). Based on typical durations of the spine uEPSPs experimentally measured in the previous chapter, the decay time constant for the simulated synapse here will be set to 15 ms. The effect of increasing values of g_{syn}, between 0.2 to 10 nS, will be tested for spines with different neck resistances, and located at different locations on the dendrite. Simulations will run for 200 ms with 0.05 ms time steps, and the exponential synapse will be activated at 80 ms. All simulations will be run in NEURON, and

for each simulation, the time series of membrane voltage in each compartment spine, parent dendrite and soma, will be saved for analysis using custom code written in MATLAB.

3.3 Interplay between the Spine Neck and the Dendritic Resistance

Unlike axons, dendrites become progressively narrower with distance from the soma. This tapering of the dendrite makes distant regions have larger dendritic longitudinal resistances than more proximal ones. Consider the dendrite as a cylindrical conductor of length l and radius *r* (Figure 3.2A). The current flow (I_L) from point 2 to point 1 will be determined by Ohm's law, such that:

$$I_L = (V_2 - V_1) / R_L$$

Where V_2 and V_1 is the voltage at each location, and R_L is the longitudinal resistance. In dendrites, R_L is proportional to the cytoplasmic resistivity (R_a) and the dendritic length (l), and is inversely proportional to the cross sectional area in the following relationship:

$$R_L = R_a \, l / \pi r^2$$

Thus, when dendrites taper with distance, *r* becomes smaller, and R_L increases. As a consequence, the impedance mismatch between the spine and dendrite will

be smaller at distal locations, and therefore, these spines will be more isopotential with the parent dendrite.

The schematic in Figure 3.2B is meant to illustrate the cases that will be studied here with the simulations. A single spine will be connected to a basal dendrite through a spine neck. Based on the experimental results in Chapter 2, R_{neck} will vary between 80-1000 MΩ. The spine will be connected either proximally (50 µm) or more distally (130 µm) from the soma. Given that the parent dendrite has been divided into segments of 10 µm in length each, and that the spine is placed at the center of the segment, the longitudinal dendritic resistance (R_{dend}) at the base of the neck for each location can be calculated:

$$R_{dend\ (50\ \mu m)} = \frac{1}{2}\frac{150 * 10^4\ \Omega\ \mu m * 10\ \mu m}{\pi * (1.3\ \mu m)^2} = 1.4\ M\Omega$$

$$R_{dend\ (130\ \mu m)} = \frac{1}{2}\frac{150 * 10^4\ \Omega\ \mu m * 10\ \mu m}{\pi * (0.48\ \mu m)^2} = 10\ M\Omega$$

Here, 1.3 µm and 0.48 µm correspond to the dendritic radius of the parent segment at 50 µm and 130 µm from soma, respectively. Note that a decrease in radius of ~1/3 produces an increase in R_{dend} of about an order of magnitude. However, R_{dend} alone relative to R_{neck} is not enough to calculate the dendritic voltage from the spine voltage. Due to the presence of voltage-gated conductances in the dendrite, as well as the spine, it is necessary to run a full

simulation of the entire circuit in order to properly calculate the dendritic voltage, which could have a strong component from active conductances (see below).

The postsynaptic response in the spine, parent dendrite, and soma, to the activation of the exponential synapse on a spine located either at 50 or 130 µm from soma is shown in Figure 3.3. Increasing values of g_{syn} and R_{neck} were simulated. At both spine locations, for synaptic conductances smaller than ~4 nS the spine EPSP amplitude positively correlated with R_{neck}, and larger R_{necks} always produced more attenuation in the dendrite and the soma. These results recapitulate the observations made in Chapter 2. However, when the synaptic stimulus exceeded 4 nS, nonlinearities in the postsynaptic response started to become evident for spines with small R_{necks} (80 and 200 MΩ) located 130 µm from soma. In these simulations, a dendritic spike of ~70 mV in amplitude occurred when the membrane voltage in the dendrite approached -30 mV, which is the half-activation voltage for the Na_v 1.2 voltage-gated Na^+ channels in L5 pyramidal neurons (*118*). This spike backpropagated into the spine but attenuated strongly at the soma. The nature and origin of this dendritic spike was further studied in simulations where the VGSC was deleted either from the spine or the parent dendrite (Figure 3.4). Deleting the VGSCs in the spine had no effect on the postsynaptic response to increasing stimulus intensities; however, deleting the VGSC in the dendrite completely abolished the dendritic spike, and the postsynaptic response to a distal synapse became very similar to that of a proximal synapse, where increasing stimulus intensities had a gradual increase

in the postsynaptic response in all compartments. It is important to note from these simulations that while the response was somewhat linear for small R_{necks}, it tended to asymptotically approach a plateau for increasing R_{neck} values (last two rows in Figure 3.4).

A question that arises from these simulations is why a spike does not seem to originate at spines when the EPSP amplitude in the spine reaches the activation threshold for VGSCs. A possible answer to this question is that even though the density of VGSCs in the spine and the parent dendrite are the same in Figures 3.3 and 3.4, 80 pS μm^{-2}, the current in the spine is negligible compared to that of the parent dendrite. Figure 3.5 shows that the simulated spine of 0.8 µm in diameter and R_{neck} of 1000 MΩ needs to have a VGSC density of about 2000 pS μm^{-2} in order to generate a sodium spike of ~80 mV in amplitude when the synaptic conductance reaches at least 1.8 nS.

In conclusion, local dendritic sodium spikes can occur at distal dendritic regions when the synaptic input on a single spine is large enough (~4 nS), and the spine R_{neck} is small enough, so that the depolarization in the parent dendrite reaches the activation threshold for VGSCs. This phenomenon does not occur for spines with R_{neck} greater than 400 MΩ, at least for spines up to 130 µm from soma, because the attenuation of the electrical signal through the spine neck is so large that the dendritic depolarization is not enough to reach the activation threshold for the VGSCs. Figure 3.6 shows the EPSP amplitude ratio between

the spine and the dendrite for increasing g_{syn} values; this plot shows that distal spines with R_{neck} of 200 and 80 MΩ are ~3x more isopotential with the dendrite when they receive synaptic input than proximal spines. Previous studies have suggested that local dendritic spikes serve as a mechanism whereby distal synapses overcome the increased attenuation at the soma (*129*). The bottom panel in Figure 3.6 shows the spine to soma EPSP amplitude ratio for proximal and distal synapses. Interestingly, instead of being smaller, this ratio increases when the dendritic spike occurs in distal spines, showing that the amount of attenuation at the soma is larger; this can be attributed to dendritic filtering of the spike as it fails to propagate the soma.

3.4 Clustered Synchronous Spines

In the previous simulations a single spine was activated by the exponential synapse, and this model was used to study how R_{neck} and R_{dend} combined can create nonlinearities in the postsynaptic response when the stimulus intensity is large, >4 nS. However, we saw in Chapter 2 that unitary EPSPs evoked by glutamate uncaging that resemble miniature EPSPs at the soma never exceeded ~1.5 nS. Thus it is unlikely that activation of a single synapse will cause a dendritic spike. At the same time, it is more realistic to consider a cell receiving input simultaneously from multiple synapses. In the simulations presented in this section, several synapses (up to four), clustered either at 50 µm or 130 µm from soma, will be activated simultaneously on spines with the same characteristics: spine head diameter, spine neck resistance, and density of active and passive

conductances (Figure 3.7). The distance between the spines will be 10 μm for the first set of simulations (Figure 3.7-3.10), and the last simulations will show the effect of decreasing this distance to 3 μm (Figure 3.11).

The postsynaptic response to the synchronous activation of the four spines is shown in Figure 3.8. This figure shows that when proximal spines receive coincident synaptic input with a synaptic conductance in each spine of at least ~3.3 nS, the summation of the individual EPSPs in the dendritic segment could lead to activation of a dendritic spike, unless the spine R_{neck} was very large, 1000 MΩ. This contrasts with Figure 3.3 where the EPSP from a single proximal spine never produced a dendritic spike. The minimum individual synaptic conductance required to generate the dendritic spike from coincident input on clustered distal spines was significantly smaller, 1.8 nS, which is much closer to the unitary synaptic conductance observed from EPSPs evoked by glu-uncaging. Moreover, the dendritic spike was triggered from these distal spines even when the R_{neck} was as large as 1000 MΩ.

Comparison of the EPSP amplitudes in the spine, parent dendrite and soma for simulations when 1, 2 and 4 spines were activated by the exponential synapse is shown in Figure 3.9. This figure shows that coincident synaptic input facilitates the generation of a dendritic spike by decreasing the amplitude of the unitary synaptic conductance needed to generate the spike. However, for distal spines, this also means saturation of the postsynaptic response; when four distal spines

are stimulated simultaneously, the EPSP amplitude in the spine and the parent dendrite saturate with very small synaptic conductances, thus, these compartments would not be able to distinguish between a small input intensity and a large one. Previous studies have suggested a decaying gradient of VGSCs along basal dendrites of L5 pyramidal neurons (*27, 116*). It is possible that this kind of gradient will prevent the saturation of the postsynaptic response to coincident input in distal dendritic regions. To test this, a decaying gradient of VGSCs was generated using the same values as those by Nevian et al (*27*), where the density of the VGSCs at the soma was 200 pS μm^{-2}, instead of 80 pS μm^{-2}, and decreased linearly with distance, reaching 0 pS μm^{-2} at the tip of the dendrite, 200 µm from soma. The results of these simulations are shown in Figure 3.10. For proximal clustered spines, a decreasing gradient of VGSCs had the effect of reducing the amplitude of the sodium spike, and increasing the amplitude of the unitary synaptic conductance required to generate the spike. This would also mean that more spines would have to be activated synchronously in order to generate the local sodium spike. Similar results were observed for clustered distal spines, where the decreasing VGSC gradient almost completely abolished the sodium spike that was generated when four spines received synaptic input synchronously. This gradient also meant less saturation of the spine and dendritic responses for coincident distal synapses, at least up to 2 nS of unitary synaptic conductance. Interestingly, spines with R_{neck} of 440 MΩ had a larger range of g_{syn} values that could generate responses of increasing amplitudes before reaching saturation.

It would be reasonable to expect that synchronous spines will be more likely to generate a sodium spike if the distance between the spines is small, or in other words, if the spines are more clustered together on a particular dendritic segment. This facilitation should be reflected as a decrease in the unitary synaptic conductance required to generate the dendritic sodium spike. Figure 3.11 shows the effect of spine clustering on the generation of sodium spikes. Surprisingly, decreasing the distance between the spines from 10 μm to 3 μm did not reduce the minimum unitary conductance required for a spike, but rather increased it, at least for synapses up to 160 μm from soma. The reason for this can be best seen in the snapshots of the simulations shown in the figure. The fact that more distant spines are more likely to generate a sodium spike, due to the smaller impedance mismatch between the spine and the dendrite, means that a set of synchronous spines is more likely to generate a spike if the set contains more distant spines. This is because the spikes generated in more distant regions will backpropagate into the proximal spines within the dendritic segment. When the spines are too clustered in space, this advantage is reduced because all spines will have a similar impedance mismatch between the spine and the dendrite. The panels comparing this effect for spines clustered either at 50 μm or 130 μm from soma show that this effect is more pronounced for proximal dendritic regions.

3.5 Discussion

Excitatory postsynaptic potentials in the spine head have to travel through the spine neck to reach the soma. The amount of attenuation of these EPSPs at the soma will not only depend on the spine neck resistance, but also on the dendritic resistance of the parent dendrite. We have used computer simulations to understand the mechanisms by which both, R_{neck} and R_{dend} influence the amplitude and attenuation of the EPSPs produced by a single spine, or by clustered synchronous spines. Simulations of a single spine showed that spines with small R_{neck} (80 to 200 MΩ) located in distal dendritic regions (~130 µm from soma), where R_{dend} is larger, could generate sodium dendritic spikes when the unitary synaptic conductance reached ~4 nS. These local dendritic spikes backpropagated into the spines, but were strongly attenuated at the soma. This phenomenon did not occur for spines with large R_{neck} because the amount of attenuation at the dendrite was so large that it prevented the dendrite from reaching the activation threshold of VGSCs. It did not occur either for proximal spines (~50 µm from soma) where R_{dend} was so small that the dendritic EPSP rapidly dissipated to adjacent dendritic compartments. However, simulations of clustered spines showed that proximal spines could generate local dendritic spikes if the synaptic input was synchronous. As expected, larger number of synchronous spines meant smaller unitary synaptic conductances required to generate the dendritic sodium spike.

Experimental evidence for the sodium spikes observed in these simulations exists. The first description of these spikes at 100-150 µm from soma in basal dendrites of L5 pyramidal neurons was by Milojkovic et al (*26*), where by using suprathreshold glutamatergic excitation, either by synaptic stimulation at 50 Hz or localized glutamate iontophoresis, they could observe a dendritic "spikelet" of ~80 mV in amplitude at the dendrite, and ~10 mV in amplitude at the soma. Larger glutamatergic excitation produced a sustained somatic depolarization superimposed with a burst of action potentials, which we did not observe in the simulations. Thus, this burst of action potentials probably resulted from the activation of a large number of synapses. Nevian et al (*27*) also reported local dendritic sodium spikes at 42-89 µm from soma that were evoked by dendritic current injection, and had a ~40 mV amplitude in the dendrite, but attenuated to ~5 mV at the soma. Fast glu-uncaging onto neighboring spines on oblique dendrites of hippocampal CA1 pyramidal neurons has also been shown to produce local dendritic spikes of ~60 mV in amplitude (*77*). Thus the sodium spikes that were studied here with the simulations do actually occur in real neurons under physiological conditions, and are likely to represent a fundamental mechanism for dendritic input integration.

Due to the difficulty of assessing R_{neck} experimentally, studies that discuss dendritic spikes have largely ignored the role of R_{neck} in their generation. Our simulations based on experimental estimates of R_{neck} from Chapter 2 provide insight on how R_{neck} combined with R_{dend} can facilitate/prevent the generation of

dendritic spikes within a plausible range of unitary synaptic conductances. While it is unlikely that a single spine will generate a sodium spike, synchronous synaptic input onto multiple spines with R_{neck} less than 1000 MΩ has a good chance of generating dendritic non-linearities that backpropagate into the spines. The minimum unitary synaptic conductance required to generate a sodium spike decreased with spine distance from soma, number of activated spines, and density of VGSCs, but it did not decrease when the distance between the activated spines decreased from 10 to 3 μm. Thus, even though spines do function as electrical compartments, each spine perceives the resulting summation of synaptic input at the parent dendritic. How this changes the individual spine physiology should be studied in more detail experimentally. Moreover, our simulations showed how these non-linearities depend strongly on the distribution and densities of voltage-gated channels, particularly sodium, along the dendritic cable. If these distributions change during development, then the mode of dendritic integration should be expected to be subject to developmental changes as well.

Figures

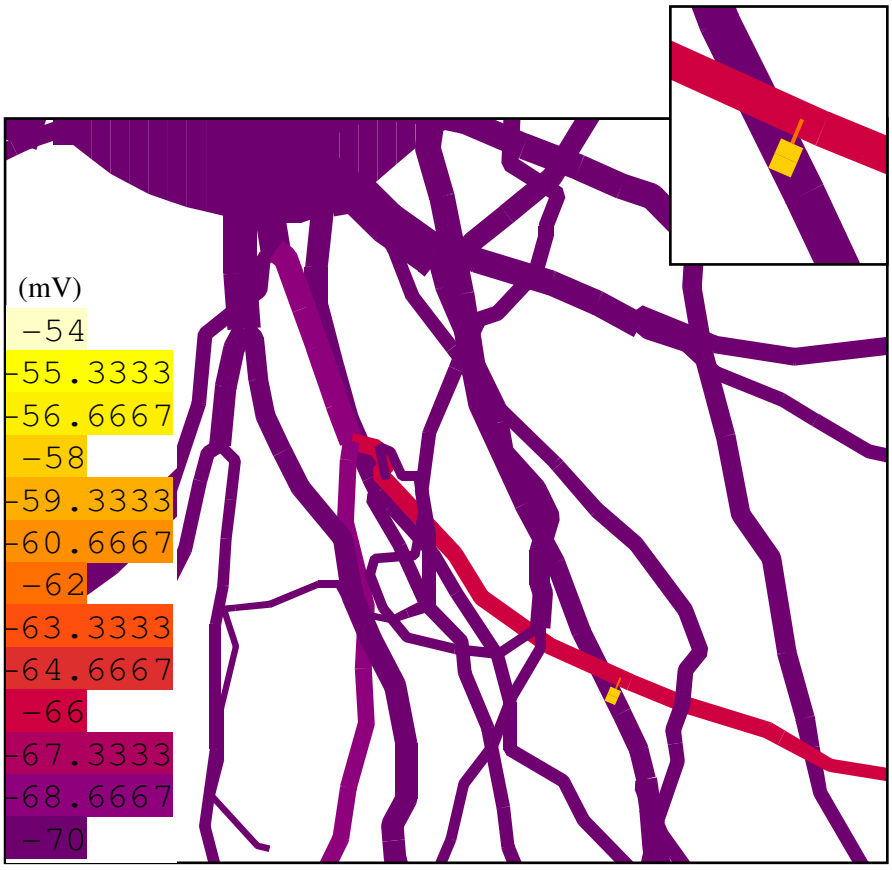

Figure 3.1. Modeling EPSPs in Single Spines. Example of a simulation showing the target spine (0.8 μm in diameter) connected through the spine neck to a basal dendrite in a morphologically realistic model of a L5 pyramidal neuron. The heat map corresponds to the membrane voltage in all compartments 2 ms after the activation of an exponential synapse of the spine head.

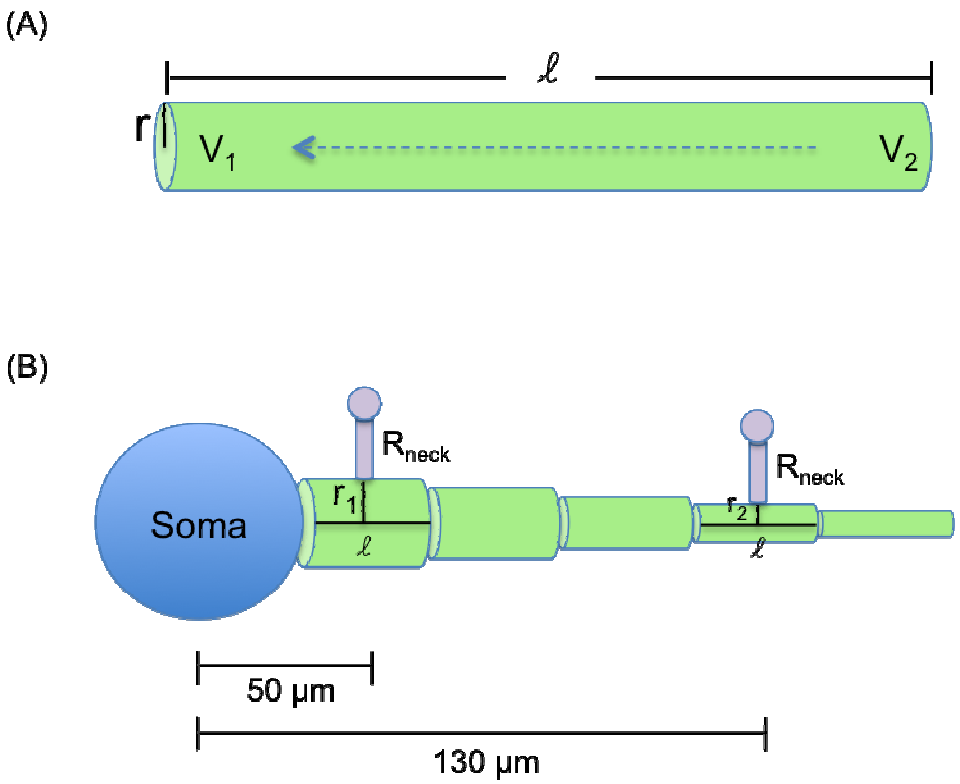

Figure 3.2. Spine Neck Resistance versus Dendritic Longitudinal Resistance. **(A)** Schematic diagram of a passive cylinder showing how the current flow from 2 to 1 will depend on the voltage difference (V_2 - V_1) and the longitudinal resistance of the cylinder, which is proportional to its length (l), and inversely proportional to its radius (r). **(B)** Schematic diagram of a basal dendrite showing the increased tapering of the dendrite with distance from soma. This cartoon represents the conditions that will be explored with the simulations. A spine with a given R_{neck} will be connected to the basal dendrite either 50 µm or 130 µm from soma. The dendritic longitudinal resistance at the base of the neck for each condition can be calculated based on the radius (r_1 or r_2) of the l = 10 µm long segment at the base of the neck.

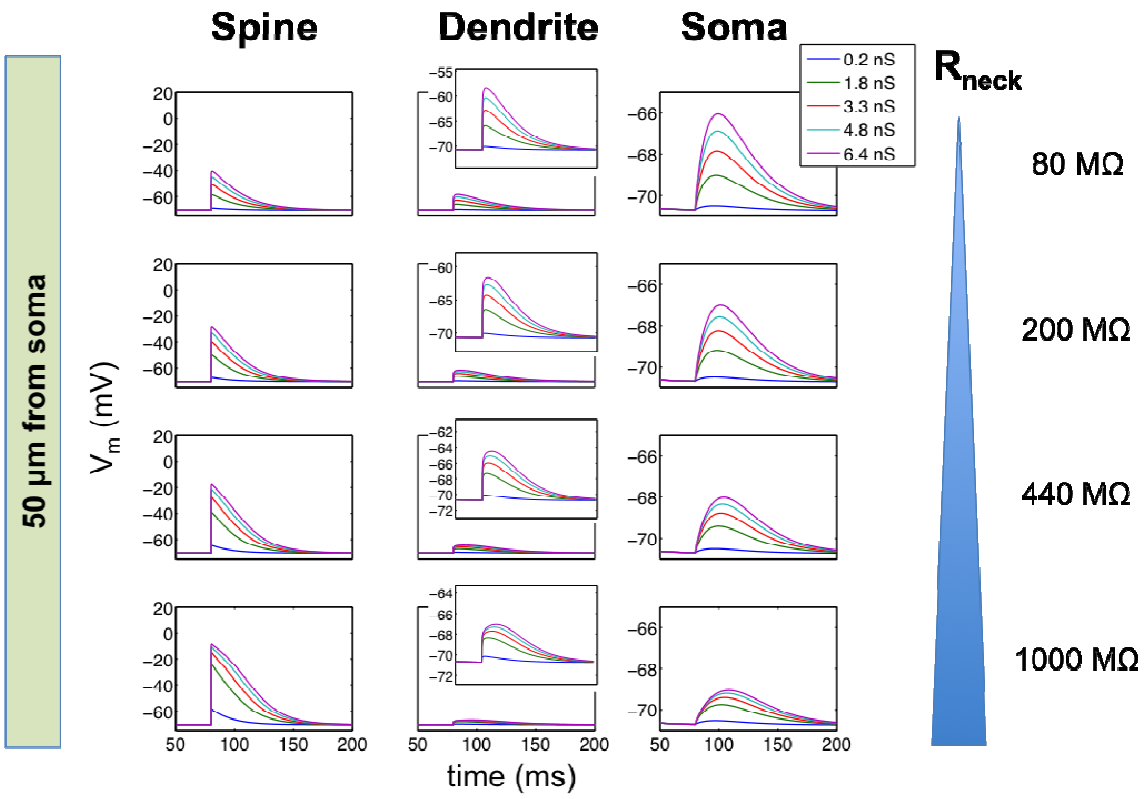
50 µm from soma
Spine
Dendrite
Soma
0.2 nS
1.8 nS
3.3 nS
4.8 nS
6.4 nS
R_{neck}
80 MΩ
200 MΩ
440 MΩ
1000 MΩ
V_m (mV)
time (ms)

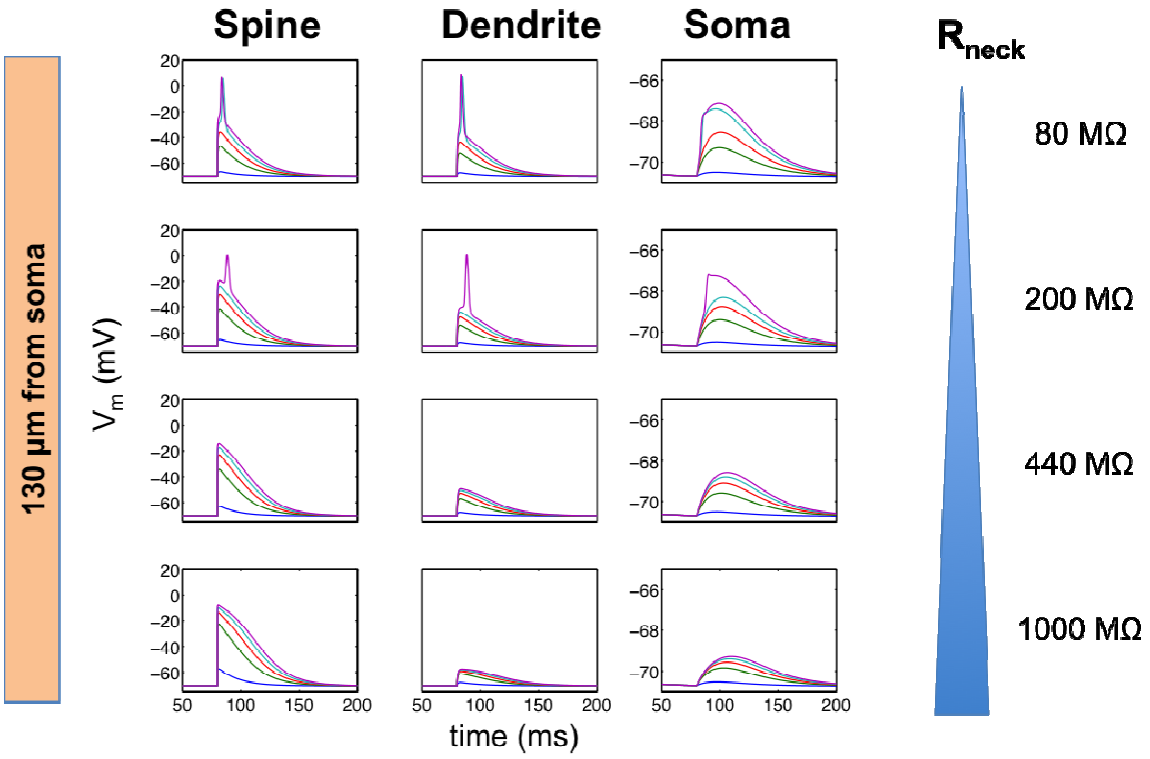
130 µm from soma
Spine
Dendrite
Soma
R_{neck}
80 MΩ
200 MΩ
440 MΩ
1000 MΩ
V_m (mV)
time (ms)

Figure 3.3. Effect of R_{dend} and R_{neck} on the postsynaptic response to a single synapse. Each panel shows the time series of membrane voltage in the spine, parent dendrite (at the base of the neck), and the soma, before and after activation of the exponential synapse on the spine head at 80 ms. Top and bottom panels correspond, respectively, to simulations where the spine was located at 50 and 130 μm from soma. The color of each trace corresponds to different values of g_{syn} as shown in the legend. Each row corresponds to simulations where the spine R_{neck} had the specified value shown on the right.

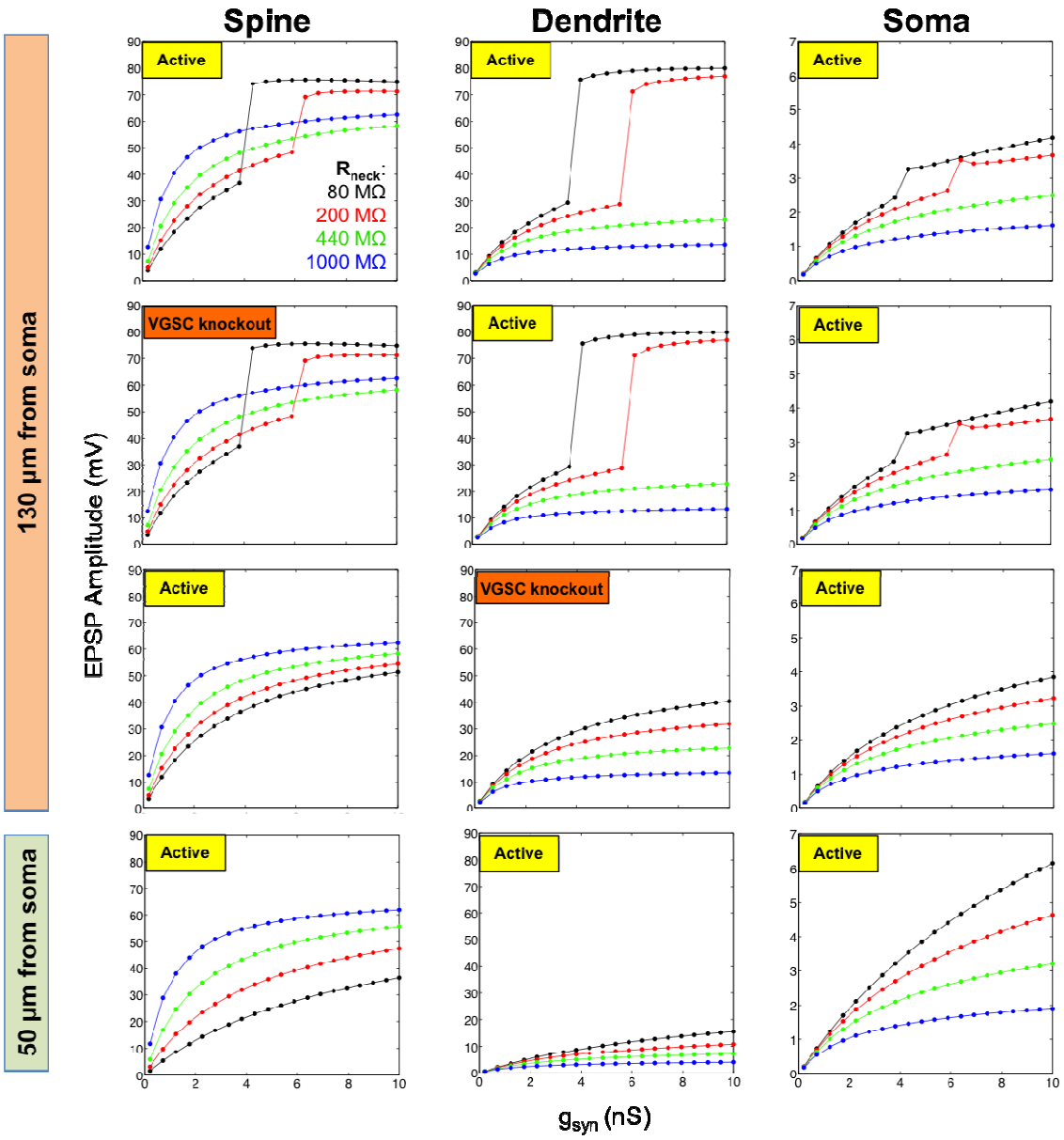

Figure 3.4. Role of VGSCs in the generation of dendritic spikes with large synaptic conductances. Each panel shows the EPSP amplitude in the spine, parent dendrite and soma for increasing values of g_{syn} and R_{neck}. The first three rows correspond to a spine located 130 µm from soma, and the last row to a spine 50 µm from soma for comparison. Panels labeled active indicate that the

given compartment had all active conductances mentioned in the text, such as VGSCs, VGKCs, VGCCs, and Ca^{2+}-dependent K^+ channels. Panels labeled VGSC knockout indicate that the VGSC conductance was deleted from that compartment.

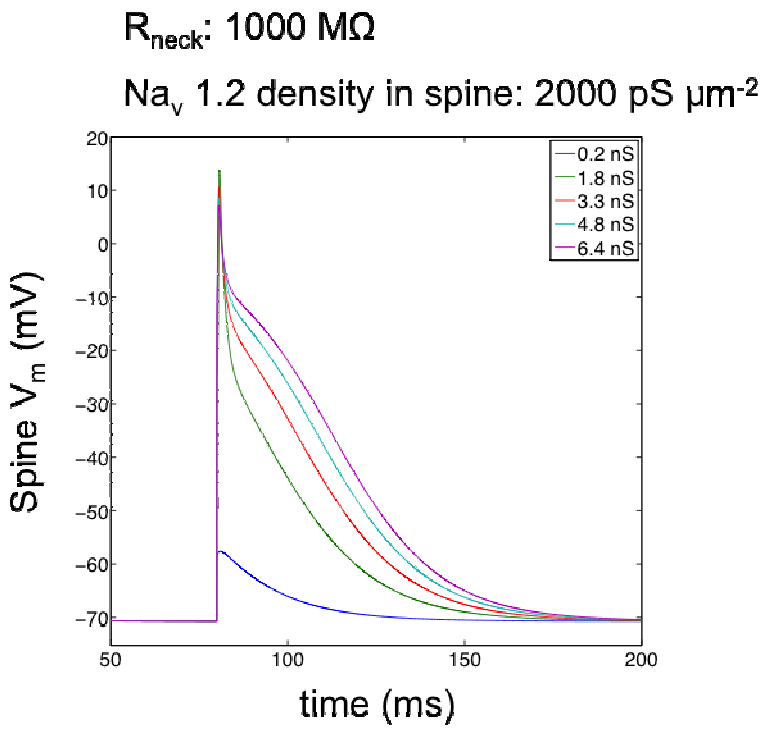

Figure 3.5. Sodium Spike in a Single Spine. Time series showing the membrane voltage in the spine before and after activation of the exponential synapse at 80 ms. Different traces correspond to different g_{syn} values shown in the legend. The spine is located 130 µm from soma, and has a spine head diameter of 0.8 µm, and R_{neck} of 1000 MΩ. The density of VGSC in the spine is 2000 pS µm^{-2}.

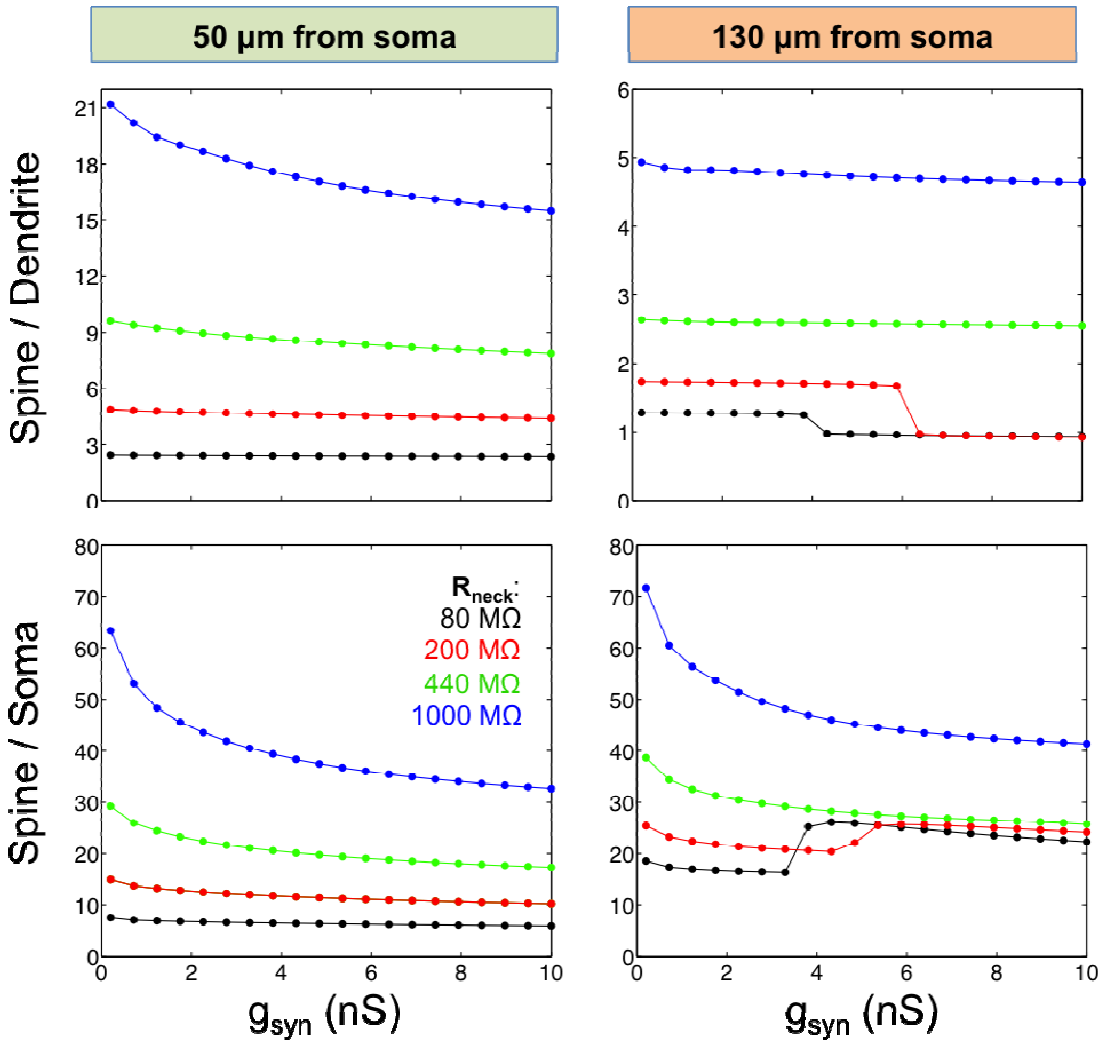

Figure 3.6. Distal spines with small R_{neck} are more isopotential with the parent dendrite. Plots showing the EPSP amplitude ratio between the spine and the dendrite *(top)*, and between the spine and the soma *(bottom),* for increasing gsyn values. Simulations for a spine 50 and 130 µm from soma are shown in the left and right panels, respectively.

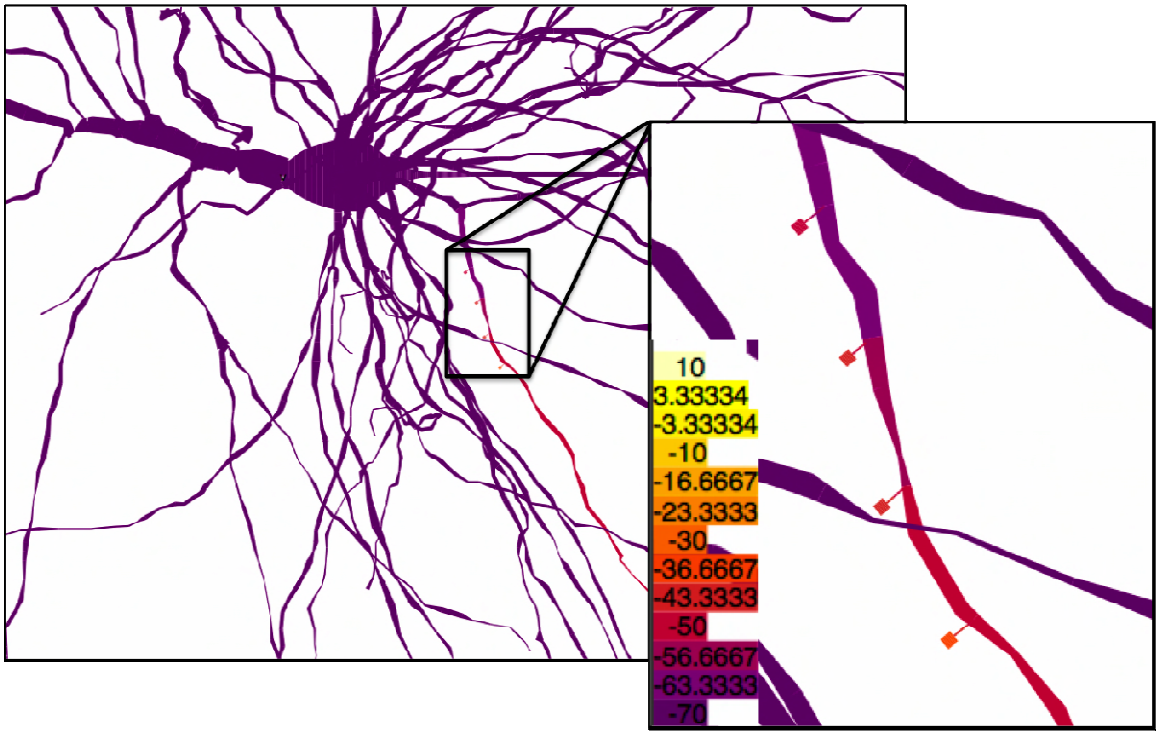

Figure 3.7. NEURON simulation of clustered synchronous spines. Example of a simulation showing four spines clustered on a dendritic segment 50 µm from soma (distance between spines: 10 µm). All the spines have the same characteristics: head diameter (0.8 um), R_{neck} (440 MΩ for this example), and density of passive and active conductances. Heat map corresponds to the membrane voltage 2 ms after activation of a 1.5 nS synaptic conductance (tau = 15 ms) on all the spines at the same time.

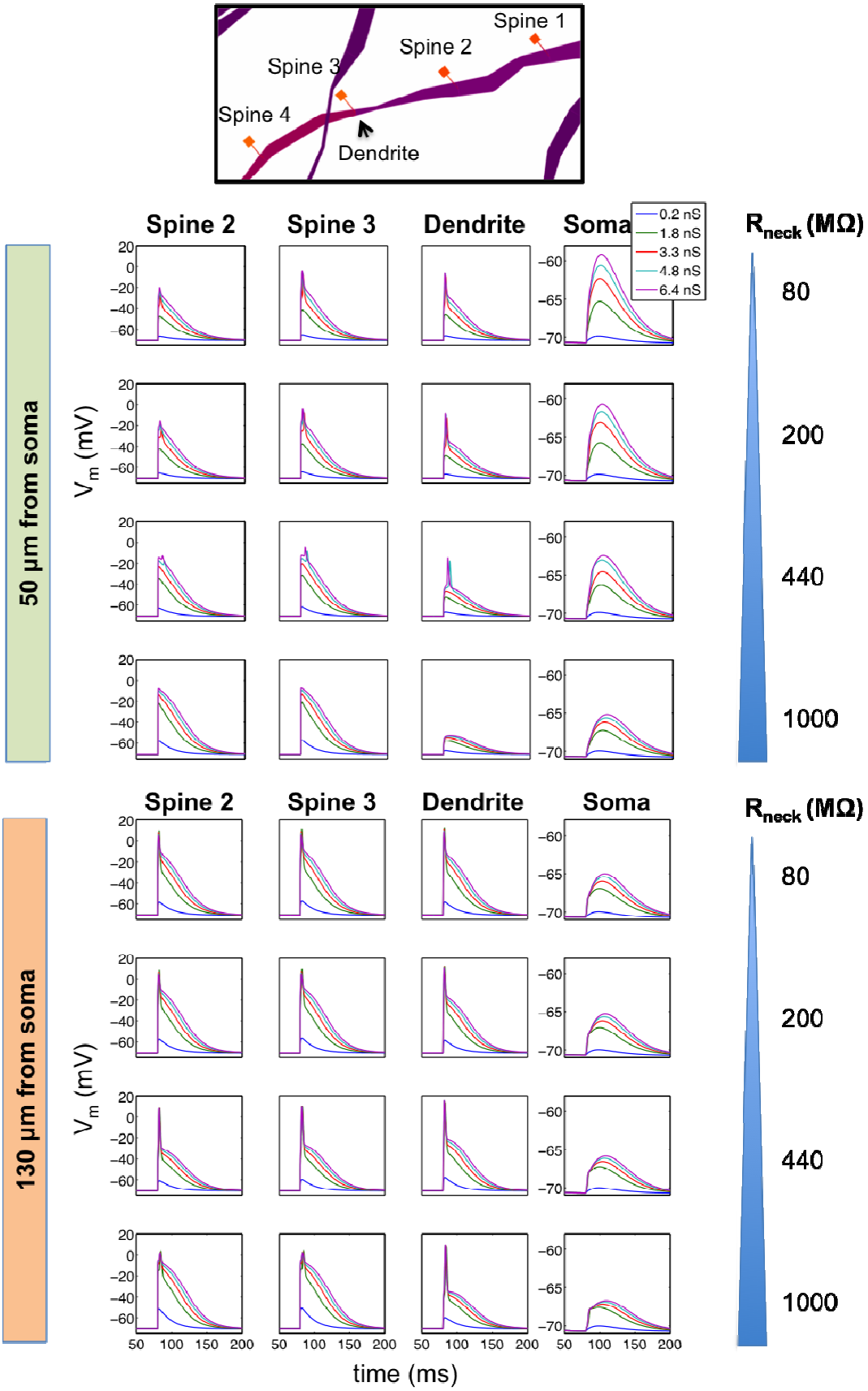
Spine 1
Spine 2
Spine 3
Spine 4
Dendrite
Spine 2
Spine 3
Dendrite
Soma
0.2 nS
1.8 nS
3.3 nS
4.8 nS
6.4 nS
R_{neck} (MΩ)
80
200
440
1000
50 µm from soma
130 µm from soma
V_m (mV)
time (ms)

Figure 3.8. Postsynaptic response to synchronous synaptic input. Panels correspond to membrane voltage before and after the synchronous activation of the exponential synapse in four spines, clustered either at 50 µm *(top panels)* or 130 µm *(bottom panels)* from soma. The recording locations for spine 2, spine 3, and dendrite are indicated in the diagram on top of the figure. Each row corresponds to simulations where all the four spines had the R_{neck} value indicated on the right.

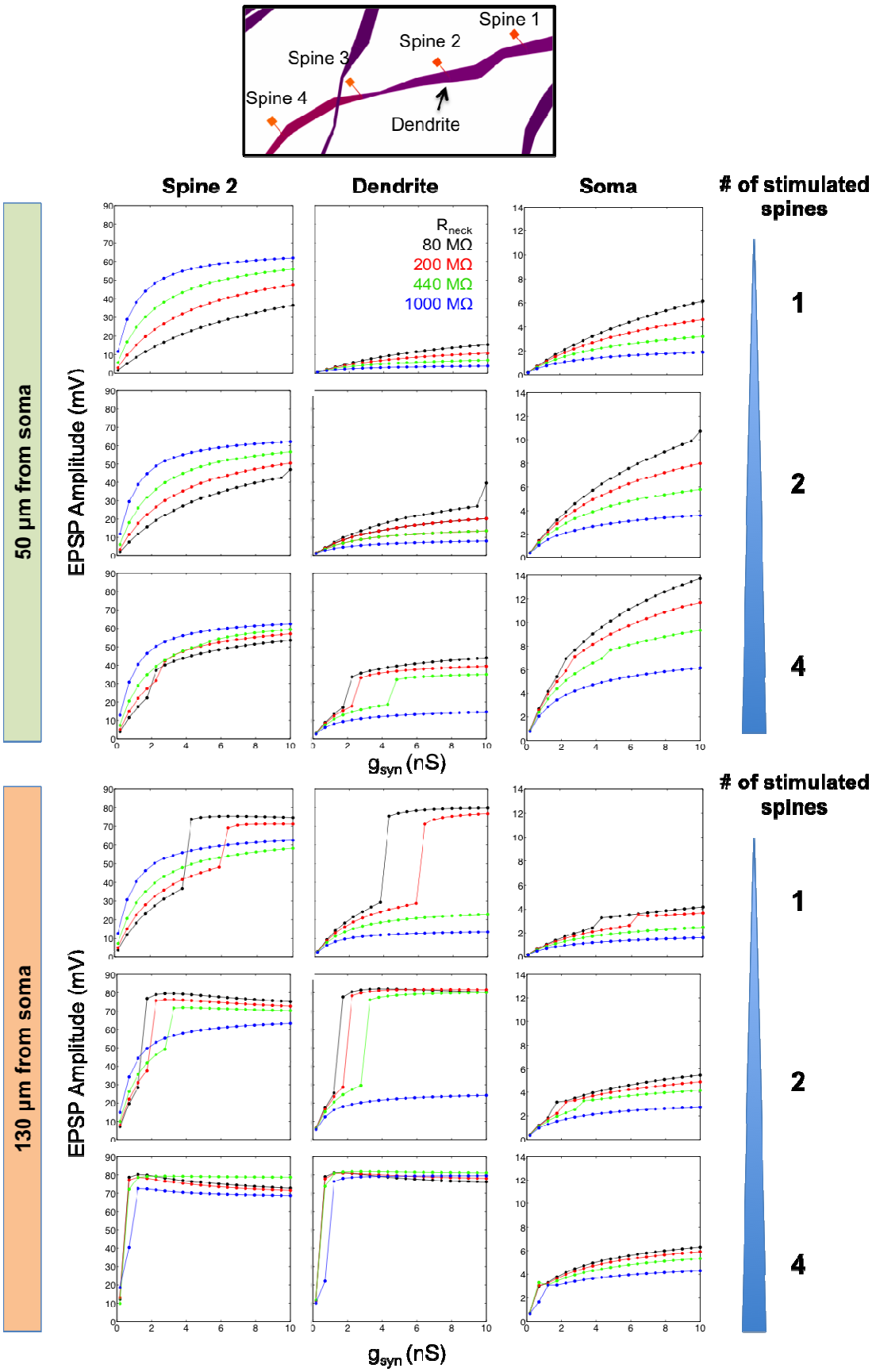
Spine 1
Spine 2
Spine 3
Spine 4
Dendrite
Spine 2
Dendrite
Soma
# of stimulated spines
50 µm from soma
130 µm from soma
EPSP Amplitude (mV)
R_{neck}
80 MΩ
200 MΩ
440 MΩ
1000 MΩ
1
2
4
g_{syn} (nS)

Figure 3.9. Cooperative synaptic input and small R_{neck} facilitate the generation of local sodium dendritic spikes. Panels show the amplitude of the EPSP in the spine, parent dendrite and soma, for increasing values of g_{syn}. The recording locations for the spine and the dendrite are indicated in the upper most figure. The first three rows correspond to spines 50 μm from soma, and the last three rows to spines 130 μm from soma. The number of stimulated spines for each row is shown on the right.

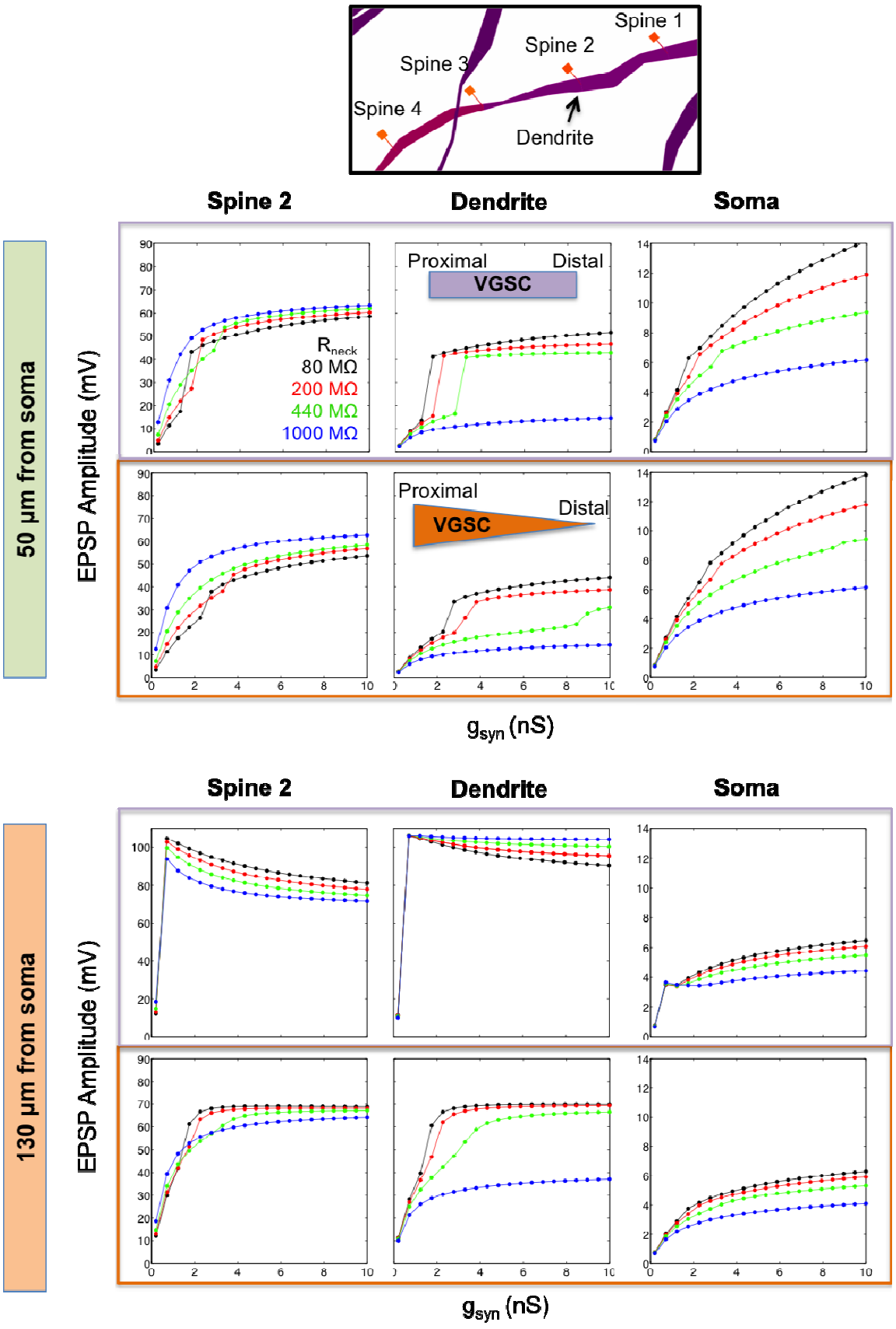
Spine 1
Spine 2
Spine 3
Spine 4
Dendrite
Spine 2
Dendrite
Soma
50 µm from soma
EPSP Amplitude (mV)
Proximal
Distal
VGSC
R_{neck}
80 MΩ
200 MΩ
440 MΩ
1000 MΩ
g_{syn} (nS)
130 µm from soma

Figure 3.10. Decaying gradient of VGSCs prevents the saturation of distal input summation. Panels show the EPSP amplitude in the spine 2, parent dendrite, and soma, for increasing values of g_{syn}, in simulations where four spines were activated by the exponential synapse simultaneously. The recording locations are shown in the upper most figure. The upper two rows correspond to spines clustered 50 µm from soma, and the bottom two rows to spines clustered 130 µm from soma. The panels enclosed by the purple rectangle correspond to simulations where the density of VGSCs was homogenous throughout the dendritic length (200 pS μm^{-2}), whereas panels enclosed by the orange rectangle correspond to simulations where the density of VGSCs decayed with a linear proximal-distal gradient (200 pS μm^{-2} and 0 pS μm^{-2} at the tip of the basal dendrite).

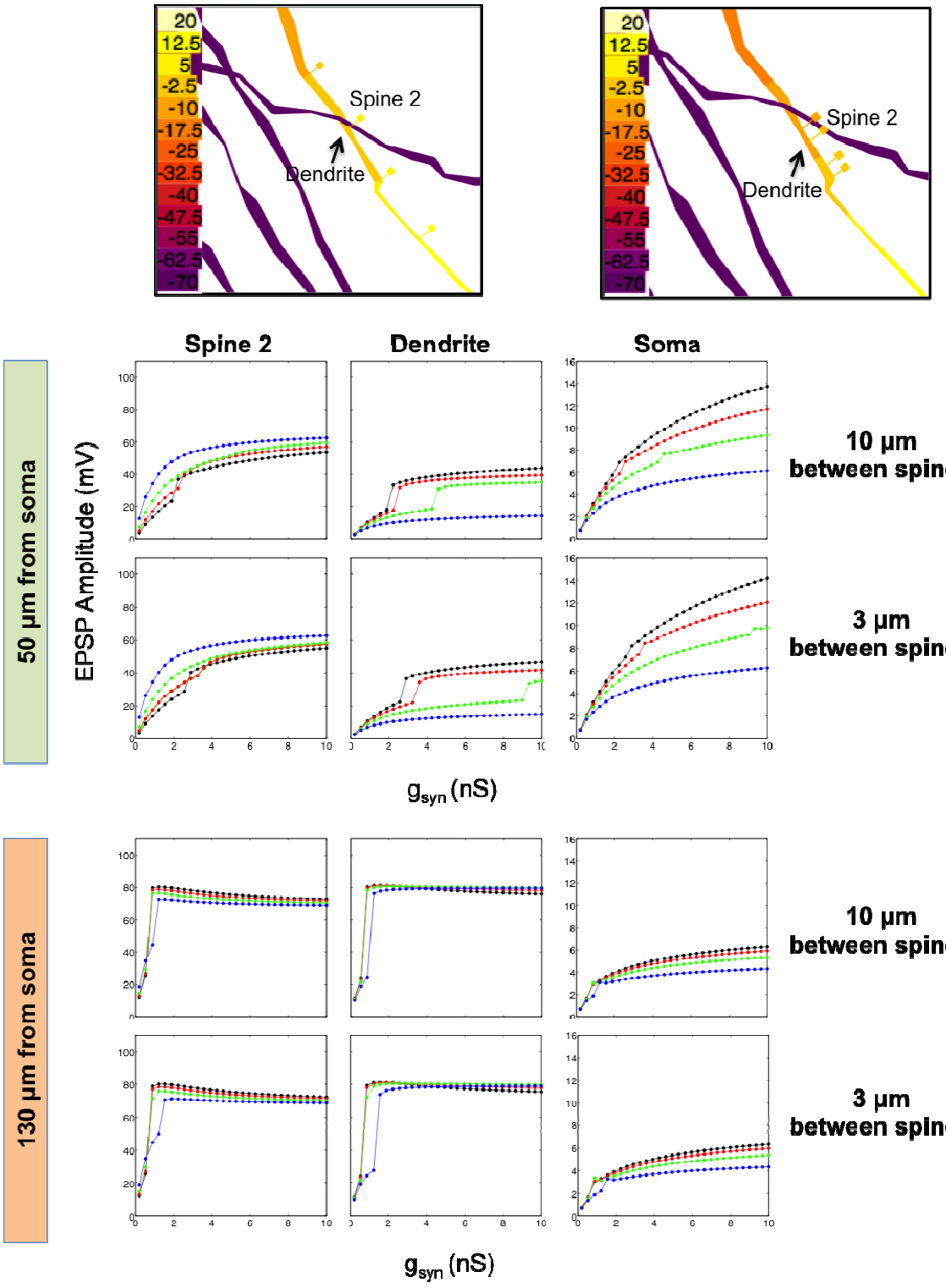
20
12.5
5
-2.5
-10
-17.5
-25
-32.5
-40
-47.5
-55
-62.5
-70
Spine 2
Dendrite
Spine 2
Dendrite
Spine 2
Dendrite
Soma
50 µm from soma
EPSP Amplitude (mV)
10 µm between spines
3 µm between spines
g_{syn} (nS)
130 µm from soma
10 µm between spines
3 µm between spines
g_{syn} (nS)

Figure 3.11. Effect of spine clustering in the generation of dendritic sodium spikes. Upper most figures show snapshots of two representative simulations 2 ms after the synchronous activation of the exponential synapse (g_{syn}=1 nS, tau=1ms) on the four different spines (R_{neck}=200 MΩ), located at ~130 µm from soma. The distance between spines is 10 µm (left) and 3 µm (right). Panels show the EPSP amplitude in the spine 2, parent dendrite, and soma for increasing values of g_{syn} in simulations where the four spines are synchronously activated. The upper two rows correspond to spines clustered 50 µm from soma, and the bottom two rows to spines clustered 130 µm from soma. The distance between the spines (either 10 µm or 3 µm) for each simulation is shown on the right.

Chapter 4

Conclusions and Suggestions for Future Research

The main conclusion from this study is that spines behave as electrical compartments capable of confining electrical synaptic signals. This has profound implications for neurotransmission. On one hand, the fact that the spine neck resistance is so variable, and at the same time large enough to act as an electrical resistor, means that synaptic signals from different spines can have different levels of attenuation at the soma, and at the dendrite. Therefore, when comparing multiple spines with different neck resistances, it should not be expected that larger EPSPs in the spine would necessarily produce larger somatic or dendritic EPSPs. Why would a synapse produce a large EPSP in the spine that does not necessarily translate into a large EPSP at the soma or the dendrite? It could be that this is an indirect consequence of exploiting the spine neck resistance to facilitate the activation of active conductances within the spine if the synaptic input is strong enough (see below), or it could be that a large local EPSP is translated into a long lasting biochemical signal that slowly propagates throughout the dendrite. Further studies that combine the techniques in this study with Ca^{2+} imaging, or imaging of other biosensors for molecular pathways, such as CAMKII, or Rho GTPases should elucidate these possibilities.

In addition, even though large spine neck resistances increase the amount of dendritic and somatic attenuation of the EPSP, they also enhance by passive mechanisms the EPSP amplitude within the spine. This would facilitate the activation of voltage-gated channels in the spine if the synaptic input were strong enough. Our measurements of the amplitude of glutamate-uncaging evoked EPSPs in the spine that resemble miniature EPSPs at the soma suggest that these unitary conductances are mainly mediated by the opening of AMPARs, without significant contributions from other voltage-gated channels. However, stimulation protocols that lead to synaptic plasticity, such as high frequency synaptic stimulation, do rely on the opening of NMDARs. Thus, the fact that the spine neck confines and enhances the EPSPs within the spine means that it facilitates the opening of these receptors, and therefore, facilitates the induction of synaptic plasticity. The techniques developed in this study: VSDI from single spines, FRAP and 3D volume reconstructions of the spine head, could be combined with high frequency synaptic stimulation to induce long-term potentiation (LTP) in the spine. This kind of experiment should not only measure the amplitude change in the spine EPSP before and after LTP, but should also demonstrate that spines with large neck resistances are more prone to undergo LTP. By estimating the spine neck resistance before and after LTP induction, this experiment should also demonstrate if the spine neck resistance is modulated by synaptic plasticity.

Finally, the simulations shown in the last chapter of this study show that the spine neck and the dendritic resistance combined, along with the dendritic distribution of voltage-gated sodium channels, could facilitate or prevent non-linearities in the dendritic integration of synaptic input, such as the generation of dendritic sodium spikes, which backpropagate into the spines without attenuation, but attenuate strongly at the soma. We showed that distal spines with small neck resistances are more prone to lead to sodium spikes if the synaptic conductance is large enough, or if enough number of spines are stimulated simultaneously. How the backpropagation of sodium spikes affects spine physiology is something that has not been studied experimentally. These spikes could facilitate the activation of NMDARs within the spine by releasing the Mg^{2+} block, and therefore, make spines more likely to undergo synaptic plasticity. Using fast glu-uncaging onto multiple spines clustered on a dendritic segment, either proximal or distal, and measuring the spine response through VSD and Ca^{2+} imaging should help elucidate whether these spikes open NMDARs in the spine, and whether this leads to an enchantment in the spine and somatic responses to further glutamate uncaging.

Even though in the simulations we only explored dendritic sodium spikes mediated by VGSCs in the basal dendrites of L5 pyramidal neurons, slow spikes mediated by NMDARs have also been observed in these dendrites (*69*). Using fast multisite glu-uncaging and VSDI from spines in the presence of VGSCs and NMDARs blockers should help elucidate the different effects of these spikes on

the spine electrophysiology. By performing this kind of experiment on animals at different developmental stages, one could also test whether the modes and the characteristics of dendritic integration vary with age. Since the generation of dendritic spikes will largely depend on the distribution of voltage-gated channels, this experiment should be combined with immunostaining for the channels involved.

In conclusion, in this study we developed experimental techniques to study directly the electrical behavior of spines undergoing excitatory synaptic input, and show how these behavior is governed by the spine morphology. Our experiments provide experimental evidence that spines behave as electrical compartments capable of isolating synaptic signals. By narrowing the spine neck spines can, by purely passive mechanisms, enhance the excitatory synaptic potentials within the spine, as well as increase the amount of attenuation at the soma. These results shed light on the physiological role of spines for proper neuronal function, and could be used as a reference point to investigate the malfunctioning of spines in different neurological disorders.

Bibliography

1. C. Koch, A. Zador, The function of dendritic spines: devices subserving biochemical rather than electrical compartmentalization. *J Neurosci* **13**, 413 (Feb, 1993).
2. C. Sala, M. Segal, Dendritic spines: the locus of structural and functional plasticity. *Physiol Rev* **94**, 141 (Jan, 2014).
3. K. M. Harris, F. E. Jensen, B. Tsao, Three-dimensional structure of dendritic spines and synapses in rat hippocampus (CA1) at postnatal day 15 and adult ages: implications for the maturation of synaptic physiology and long-term potentiation. *J Neurosci* **12**, 2685 (Jul, 1992).
4. D. Tsay, R. Yuste, On the electrical function of dendritic spines. *Trends Neurosci* **27**, 77 (Feb, 2004).
5. I. Segev, W. Rall, Computational study of an excitable dendritic spine. *J Neurophysiol* **60**, 499 (Aug, 1988).
6. D. H. Bhatt, S. Zhang, W. B. Gan, Dendritic spine dynamics. *Annu Rev Physiol* **71**, 261 (2009).
7. M. Miller, A. Peters, Maturation of rat visual cortex. II. A combined Golgi-electron microscope study of pyramidal neurons. *J Comp Neurol* **203**, 555 (Dec 20, 1981).
8. J. C. Fiala, M. Feinberg, V. Popov, K. M. Harris, Synaptogenesis via dendritic filopodia in developing hippocampal area CA1. *J Neurosci* **18**, 8900 (Nov 1, 1998).
9. M. E. Dailey, S. J. Smith, The dynamics of dendritic structure in developing hippocampal slices. *J Neurosci* **16**, 2983 (May 1, 1996).
10. N. E. Ziv, S. J. Smith, Evidence for a role of dendritic filopodia in synaptogenesis and spine formation. *Neuron* **17**, 91 (Jul, 1996).
11. B. Lendvai, E. A. Stern, B. Chen, K. Svoboda, Experience-dependent plasticity of dendritic spines in the developing rat barrel cortex in vivo. *Nature* **404**, 876 (Apr 20, 2000).

12. J. De Felipe, P. Marco, A. Fairen, E. G. Jones, Inhibitory synaptogenesis in mouse somatosensory cortex. *Cereb Cortex* **7**, 619 (Oct-Nov, 1997).
13. P. R. Huttenlocher, Morphometric study of human cerebral cortex development. *Neuropsychologia* **28**, 517 (1990).
14. P. Rakic, J. P. Bourgeois, M. F. Eckenhoff, N. Zecevic, P. S. Goldman-Rakic, Concurrent overproduction of synapses in diverse regions of the primate cerebral cortex. *Science* **232**, 232 (Apr 11, 1986).
15. T. F. Roberts, K. A. Tschida, M. E. Klein, R. Mooney, Rapid spine stabilization and synaptic enhancement at the onset of behavioural learning. *Nature* **463**, 948 (Feb 18, 2010).
16. Y. Zuo, A. Lin, P. Chang, W. B. Gan, Development of long-term dendritic spine stability in diverse regions of cerebral cortex. *Neuron* **46**, 181 (Apr 21, 2005).
17. A. J. Holtmaat *et al.*, Transient and persistent dendritic spines in the neocortex in vivo. *Neuron* **45**, 279 (Jan 20, 2005).
18. V. A. Alvarez, B. L. Sabatini, Anatomical and physiological plasticity of dendritic spines. *Annu Rev Neurosci* **30**, 79 (2007).
19. H. Kasai *et al.*, Learning rules and persistence of dendritic spines. *Eur J Neurosci* **32**, 241 (Jul, 2010).
20. B. L. Sabatini, T. G. Oertner, K. Svoboda, The life cycle of Ca(2+) ions in dendritic spines. *Neuron* **33**, 439 (Jan 31, 2002).
21. B. L. Bloodgood, B. L. Sabatini, Nonlinear regulation of unitary synaptic signals by CaV(2.3) voltage-sensitive calcium channels located in dendritic spines. *Neuron* **53**, 249 (Jan 18, 2007).
22. R. Araya, V. Nikolenko, K. B. Eisenthal, R. Yuste, Sodium channels amplify spine potentials. *Proc Natl Acad Sci U S A* **104**, 12347 (Jul 24, 2007).
23. Y. Yoshimura *et al.*, Molecular constituents of the postsynaptic density fraction revealed by proteomic analysis using multidimensional liquid chromatography-tandem mass spectrometry. *J Neurochem* **88**, 759 (Feb, 2004).

24. J. C. Magee, D. Johnston, Characterization of single voltage-gated Na+ and Ca2+ channels in apical dendrites of rat CA1 pyramidal neurons. *J Physiol* **487 (Pt 1)**, 67 (Aug 15, 1995).
25. J. C. Magee, D. Johnston, Synaptic activation of voltage-gated channels in the dendrites of hippocampal pyramidal neurons. *Science* **268**, 301 (Apr 14, 1995).
26. B. A. Milojkovic, J. P. Wuskell, L. M. Loew, S. D. Antic, Initiation of sodium spikelets in basal dendrites of neocortical pyramidal neurons. *J Membr Biol* **208**, 155 (Nov, 2005).
27. T. Nevian, M. E. Larkum, A. Polsky, J. Schiller, Properties of basal dendrites of layer 5 pyramidal neurons: a direct patch-clamp recording study. *Nat Neurosci* **10**, 206 (Feb, 2007).
28. K. Kerti, A. Lorincz, Z. Nusser, Unique somato-dendritic distribution pattern of Kv4.2 channels on hippocampal CA1 pyramidal cells. *Eur J Neurosci* **35**, 66 (Jan, 2012).
29. D. Allen *et al.*, The SK2-long isoform directs synaptic localization and function of SK2-containing channels. *Nat Neurosci* **14**, 744 (Jun, 2011).
30. I. M. Ethell, E. B. Pasquale, Molecular mechanisms of dendritic spine development and remodeling. *Prog Neurobiol* **75**, 161 (Feb, 2005).
31. L. A. Cingolani, Y. Goda, Actin in action: the interplay between the actin cytoskeleton and synaptic efficacy. *Nat Rev Neurosci* **9**, 344 (May, 2008).
32. O. L. Johnson, C. C. Ouimet, A regulatory role for actin in dendritic spine proliferation. *Brain Res* **1113**, 1 (Oct 3, 2006).
33. V. Tatavarty, E. J. Kim, V. Rodionov, J. Yu, Investigating sub-spine actin dynamics in rat hippocampal neurons with super-resolution optical imaging. *PLoS One* **4**, e7724 (2009).
34. V. Tatavarty, S. Das, J. Yu, Polarization of actin cytoskeleton is reduced in dendritic protrusions during early spine development in hippocampal neuron. *Mol Biol Cell* **23**, 3167 (Aug, 2012).

35. F. Korobova, T. Svitkina, Molecular architecture of synaptic actin cytoskeleton in hippocampal neurons reveals a mechanism of dendritic spine morphogenesis. *Mol Biol Cell* **21**, 165 (Jan 1, 2010).
36. E. Korkotian, M. Segal, Spike-associated fast contraction of dendritic spines in cultured hippocampal neurons. *Neuron* **30**, 751 (Jun, 2001).
37. O. Y. Bongmba, L. A. Martinez, M. E. Elhardt, K. Butler, M. V. Tejada-Simon, Modulation of dendritic spines and synaptic function by Rac1: a possible link to Fragile X syndrome pathology. *Brain Res* **1399**, 79 (Jul 5, 2011).
38. A. Tashiro, R. Yuste, Regulation of dendritic spine motility and stability by Rac1 and Rho kinase: evidence for two forms of spine motility. *Mol Cell Neurosci* **26**, 429 (Jul, 2004).
39. K. C. Vadodaria, C. Brakebusch, U. Suter, S. Jessberger, Stage-specific functions of the small Rho GTPases Cdc42 and Rac1 for adult hippocampal neurogenesis. *J Neurosci* **33**, 1179 (Jan 16, 2013).
40. I. H. Kim *et al.*, Disruption of Arp2/3 results in asymmetric structural plasticity of dendritic spines and progressive synaptic and behavioral abnormalities. *J Neurosci* **33**, 6081 (Apr 3, 2013).
41. K. Hayashi, T. Shirao, Change in the shape of dendritic spines caused by overexpression of drebrin in cultured cortical neurons. *J Neurosci* **19**, 3918 (May 15, 1999).
42. V. Biou, H. Brinkhaus, R. C. Malenka, A. Matus, Interactions between drebrin and Ras regulate dendritic spine plasticity. *Eur J Neurosci* **27**, 2847 (Jun, 2008).
43. A. Mammoto *et al.*, Interactions of drebrin and gephyrin with profilin. *Biochem Biophys Res Commun* **243**, 86 (Feb 4, 1998).
44. H. Hering, M. Sheng, Activity-dependent redistribution and essential role of cortactin in dendritic spine morphogenesis. *J Neurosci* **23**, 11759 (Dec 17, 2003).
45. E. Marcello, R. Epis, C. Saraceno, M. Di Luca, Synaptic dysfunction in Alzheimer's disease. *Adv Exp Med Biol* **970**, 573 (2012).

46. K. H. Ashe, K. R. Zahs, Probing the biology of Alzheimer's disease in mice. *Neuron* **66**, 631 (Jun 10, 2010).
47. J. C. Fiala, J. Spacek, K. M. Harris, Dendritic spine pathology: cause or consequence of neurological disorders? *Brain Res Brain Res Rev* **39**, 29 (Jun, 2002).
48. J. J. Hutsler, H. Zhang, Increased dendritic spine densities on cortical projection neurons in autism spectrum disorders. *Brain Res* **1309**, 83 (Jan 14, 2010).
49. C. E. Brown, K. Aminoltejari, H. Erb, I. R. Winship, T. H. Murphy, In vivo voltage-sensitive dye imaging in adult mice reveals that somatosensory maps lost to stroke are replaced over weeks by new structural and functional circuits with prolonged modes of activation within both the peri-infarct zone and distant sites. *J Neurosci* **29**, 1719 (Feb 11, 2009).
50. T. Keck *et al.*, Massive restructuring of neuronal circuits during functional reorganization of adult visual cortex. *Nat Neurosci* **11**, 1162 (Oct, 2008).
51. D. E. Feldman, Synaptic mechanisms for plasticity in neocortex. *Annu Rev Neurosci* **32**, 33 (2009).
52. M. Matsuzaki, N. Honkura, G. C. Ellis-Davies, H. Kasai, Structural basis of long-term potentiation in single dendritic spines. *Nature* **429**, 761 (Jun 17, 2004).
53. M. Fu, X. Yu, J. Lu, Y. Zuo, Repetitive motor learning induces coordinated formation of clustered dendritic spines in vivo. *Nature* **483**, 92 (Mar 1, 2012).
54. H. Makino, R. Malinow, Compartmentalized versus global synaptic plasticity on dendrites controlled by experience. *Neuron* **72**, 1001 (Dec 22, 2011).
55. J. Grutzendler, N. Kasthuri, W. B. Gan, Long-term dendritic spine stability in the adult cortex. *Nature* **420**, 812 (Dec 19-26, 2002).
56. H. Kasai, M. Matsuzaki, J. Noguchi, N. Yasumatsu, H. Nakahara, Structure-stability-function relationships of dendritic spines. *Trends Neurosci* **26**, 360 (Jul, 2003).

57. J. D. Shepherd, R. L. Huganir, The cell biology of synaptic plasticity: AMPA receptor trafficking. *Annu Rev Cell Dev Biol* **23**, 613 (2007).
58. S. Tomita, V. Stein, T. J. Stocker, R. A. Nicoll, D. S. Bredt, Bidirectional synaptic plasticity regulated by phosphorylation of stargazin-like TARPs. *Neuron* **45**, 269 (Jan 20, 2005).
59. M. Heine *et al.*, Surface mobility of postsynaptic AMPARs tunes synaptic transmission. *Science* **320**, 201 (Apr 11, 2008).
60. N. Matsuo, L. Reijmers, M. Mayford, Spine-type-specific recruitment of newly synthesized AMPA receptors with learning. *Science* **319**, 1104 (Feb 22, 2008).
61. R. Malinow, R. C. Malenka, AMPA receptor trafficking and synaptic plasticity. *Annu Rev Neurosci* **25**, 103 (2002).
62. H. K. Lee, M. Barbarosie, K. Kameyama, M. F. Bear, R. L. Huganir, Regulation of distinct AMPA receptor phosphorylation sites during bidirectional synaptic plasticity. *Nature* **405**, 955 (Jun 22, 2000).
63. Q. Zhou, K. J. Homma, M. M. Poo, Shrinkage of dendritic spines associated with long-term depression of hippocampal synapses. *Neuron* **44**, 749 (Dec 2, 2004).
64. W. Rall, Distinguishing theoretical synaptic potentials computed for different soma-dendritic distributions of synaptic input. *J Neurophysiol* **30**, 1138 (Sep, 1967).
65. S. Cash, R. Yuste, Linear summation of excitatory inputs by CA1 pyramidal neurons. *Neuron* **22**, 383 (Feb, 1999).
66. G. Tamas, J. Szabadics, P. Somogyi, Cell type- and subcellular position-dependent summation of unitary postsynaptic potentials in neocortical neurons. *J Neurosci* **22**, 740 (Feb 1, 2002).
67. R. Yuste, R. Urban, Dendritic spines and linear networks. *J Physiol Paris* **98**, 479 (Jul-Nov, 2004).
68. J. S. Nettleton, W. J. Spain, Linear to supralinear summation of AMPA-mediated EPSPs in neocortical pyramidal neurons. *J Neurophysiol* **83**, 3310 (Jun, 2000).

69. J. Schiller, G. Major, H. J. Koester, Y. Schiller, NMDA spikes in basal dendrites of cortical pyramidal neurons. *Nature* **404**, 285 (Mar 16, 2000).
70. K. D. Oikonomou, S. M. Short, M. T. Rich, S. D. Antic, Extrasynaptic glutamate receptor activation as cellular bases for dynamic range compression in pyramidal neurons. *Front Physiol* **3**, 334 (2012).
71. D. S. Wei *et al.*, Compartmentalized and binary behavior of terminal dendrites in hippocampal pyramidal neurons. *Science* **293**, 2272 (Sep 21, 2001).
72. M. E. Larkum, T. Nevian, M. Sandler, A. Polsky, J. Schiller, Synaptic integration in tuft dendrites of layer 5 pyramidal neurons: a new unifying principle. *Science* **325**, 756 (Aug 7, 2009).
73. P. Poirazi, B. W. Mel, Impact of active dendrites and structural plasticity on the memory capacity of neural tissue. *Neuron* **29**, 779 (Mar, 2001).
74. P. Poirazi, T. Brannon, B. W. Mel, Pyramidal neuron as two-layer neural network. *Neuron* **37**, 989 (Mar 27, 2003).
75. A. Polsky, B. W. Mel, J. Schiller, Computational subunits in thin dendrites of pyramidal cells. *Nat Neurosci* **7**, 621 (Jun, 2004).
76. A. Losonczy, J. C. Magee, Integrative properties of radial oblique dendrites in hippocampal CA1 pyramidal neurons. *Neuron* **50**, 291 (Apr 20, 2006).
77. S. Gasparini, J. C. Magee, State-dependent dendritic computation in hippocampal CA1 pyramidal neurons. *J Neurosci* **26**, 2088 (Feb 15, 2006).
78. J. Hao, X. D. Wang, Y. Dan, M. M. Poo, X. H. Zhang, An arithmetic rule for spatial summation of excitatory and inhibitory inputs in pyramidal neurons. *Proc Natl Acad Sci U S A* **106**, 21906 (Dec 22, 2009).
79. S. W. Jaslove, The integrative properties of spiny distal dendrites. *Neuroscience* **47**, 495 (1992).
80. M. T. Harnett, J. K. Makara, N. Spruston, W. L. Kath, J. C. Magee, Synaptic amplification by dendritic spines enhances input cooperativity. *Nature* **491**, 599 (Nov 22, 2012).

81. W. Muller, J. A. Connor, Dendritic spines as individual neuronal compartments for synaptic Ca2+ responses. *Nature* **354**, 73 (Nov 7, 1991).
82. R. Yuste, W. Denk, Dendritic spines as basic functional units of neuronal integration. *Nature* **375**, 682 (Jun 22, 1995).
83. J. C. Magee, D. Johnston, A synaptically controlled, associative signal for Hebbian plasticity in hippocampal neurons. *Science* **275**, 209 (Jan 10, 1997).
84. R. Yuste, A. Majewska, S. S. Cash, W. Denk, Mechanisms of calcium influx into hippocampal spines: heterogeneity among spines, coincidence detection by NMDA receptors, and optical quantal analysis. *J Neurosci* **19**, 1976 (Mar 15, 1999).
85. A. Majewska, E. Brown, J. Ross, R. Yuste, Mechanisms of calcium decay kinetics in hippocampal spines: role of spine calcium pumps and calcium diffusion through the spine neck in biochemical compartmentalization. *J Neurosci* **20**, 1722 (Mar 1, 2000).
86. B. L. Bloodgood, B. L. Sabatini, Neuronal activity regulates diffusion across the neck of dendritic spines. *Science* **310**, 866 (Nov 4, 2005).
87. A. Grunditz, N. Holbro, L. Tian, Y. Zuo, T. G. Oertner, Spine neck plasticity controls postsynaptic calcium signals through electrical compartmentalization. *J Neurosci* **28**, 13457 (Dec 10, 2008).
88. C. D. Harvey, R. Yasuda, H. Zhong, K. Svoboda, The spread of Ras activity triggered by activation of a single dendritic spine. *Science* **321**, 136 (Jul 4, 2008).
89. H. Murakoshi, H. Wang, R. Yasuda, Local, persistent activation of Rho GTPases during plasticity of single dendritic spines. *Nature* **472**, 100 (Apr 7, 2011).
90. T. M. Newpher, M. D. Ehlers, Spine microdomains for postsynaptic signaling and plasticity. *Trends Cell Biol* **19**, 218 (May, 2009).
91. S. Raghavachari, J. E. Lisman, Properties of quantal transmission at CA1 synapses. *J Neurophysiol* **92**, 2456 (Oct, 2004).

92. R. A. Nicoll, S. Tomita, D. S. Bredt, Auxiliary subunits assist AMPA-type glutamate receptors. *Science* **311**, 1253 (Mar 3, 2006).
93. C. Shelley, M. Farrant, S. G. Cull-Candy, TARP-associated AMPA receptors display an increased maximum channel conductance and multiple kinetically distinct open states. *J Physiol* **590**, 5723 (Nov 15, 2012).
94. G. E. Hardingham, Y. Fukunaga, H. Bading, Extrasynaptic NMDARs oppose synaptic NMDARs by triggering CREB shut-off and cell death pathways. *Nat Neurosci* **5**, 405 (May, 2002).
95. G. E. Hardingham, H. Bading, Coupling of extrasynaptic NMDA receptors to a CREB shut-off pathway is developmentally regulated. *Biochim Biophys Acta* **1600**, 148 (Nov 4, 2002).
96. W. Rall, Dynamic patterns of brain cell assemblies. II. Concept of dynamic patterns. Nonequilibrium steady states and nerve membrane biophysics. *Neurosci Res Program Bull* **12**, 27 (Mar, 1974).
97. R. Llinas, C. Nicholson, J. A. Freeman, D. E. Hillman, Dendritic spikes and their inhibition in alligator Purkinje cells. *Science* **160**, 1132 (Jun 7, 1968).
98. M. Kuno, R. Llinas, Enhancement of synaptic transmission by dendritic potentials in chromatolysed motoneurones of the cat. *J Physiol* **210**, 807 (Nov, 1970).
99. G. J. Stuart, B. Sakmann, Active propagation of somatic action potentials into neocortical pyramidal cell dendrites. *Nature* **367**, 69 (Jan 6, 1994).
100. J. P. Miller, W. Rall, J. Rinzel, Synaptic amplification by active membrane in dendritic spines. *Brain Res* **325**, 325 (Jan 28, 1985).
101. S. M. Baer, J. Rinzel, Propagation of dendritic spikes mediated by excitable spines: a continuum theory. *J Neurophysiol* **65**, 874 (Apr, 1991).
102. D. H. Perkel, D. J. Perkel, Dendritic spines: role of active membrane in modulating synaptic efficacy. *Brain Res* **325**, 331 (Jan 28, 1985).
103. K. F. Lee, C. Soares, J. C. Beique, Examining form and function of dendritic spines. *Neural Plast* **2012**, 704103 (2012).

104. R. Yuste, A. Majewska, K. Holthoff, From form to function: calcium compartmentalization in dendritic spines. *Nat Neurosci* **3**, 653 (Jul, 2000).
105. R. Yuste, Electrical compartmentalization in dendritic spines. *Annu Rev Neurosci* **36**, 429 (Jul 8, 2013).
106. B. L. Bloodgood, A. J. Giessel, B. L. Sabatini, Biphasic synaptic Ca influx arising from compartmentalized electrical signals in dendritic spines. *PLoS Biol* **7**, e1000190 (Sep, 2009).
107. L. M. Palmer, G. J. Stuart, Membrane potential changes in dendritic spines during action potentials and synaptic input. *J Neurosci* **29**, 6897 (May 27, 2009).
108. M. A. Popovic, X. Gao, N. T. Carnevale, D. Zecevic, Cortical dendritic spine heads are not electrically isolated by the spine neck from membrane potential signals in parent dendrites. *Cereb Cortex* **24**, 385 (Feb, 2014).
109. K. Svoboda, D. W. Tank, W. Denk, Direct measurement of coupling between dendritic spines and shafts. *Science* **272**, 716 (May 3, 1996).
110. C. D. Acker, P. Yan, L. M. Loew, Single-voxel recording of voltage transients in dendritic spines. *Biophys J* **101**, L11 (Jul 20, 2011).
111. C. D. Acker, L. M. Loew, Characterization of voltage-sensitive dyes in living cells using two-photon excitation. *Methods Mol Biol* **995**, 147 (2013).
112. W. Rall, “Cellular Mechanisms in Neuronal Activity” *3* (1974).
113. J. Diamond, Gray, EG., Yasargil, GM in *Excitatory synaptic mechanisms,* P. Andersen, Jansen, J, Ed. (Universitetsforlag, Oslo, 1970), pp. 212-222.
114. C. Koch, Poggio, T, Electrical properties of dendritic spines. *Trends Neurosci* **6**, 3 (1983).
115. P. Yan *et al.*, Palette of fluorinated voltage-sensitive hemicyanine dyes. *Proc Natl Acad Sci U S A* **109**, 20443 (Dec 11, 2012).
116. C. D. Acker, S. D. Antic, Quantitative assessment of the distributions of membrane conductances involved in action potential backpropagation along basal dendrites. *J Neurophysiol* **101**, 1524 (Mar, 2009).
117. T. Branco, B. A. Clark, M. Hausser, Dendritic discrimination of temporal input sequences in cortical neurons. *Science* **329**, 1671 (Sep 24, 2010).

118. W. Hu *et al.*, Distinct contributions of Na(v)1.6 and Na(v)1.2 in action potential initiation and backpropagation. *Nat Neurosci* **12**, 996 (Aug, 2009).
119. J. M. Nitsche, H. C. Chang, P. A. Weber, B. J. Nicholson, A transient diffusion model yields unitary gap junctional permeabilities from images of cell-to-cell fluorescent dye transfer between Xenopus oocytes. *Biophys J* **86**, 2058 (Apr, 2004).
120. M. L. Hines, N. T. Carnevale, The NEURON simulation environment. *Neural Comput* **9**, 1179 (Aug 15, 1997).
121. C. Fink, F. Morgan, L. M. Loew, Intracellular fluorescent probe concentrations by confocal microscopy. *Biophys J* **75**, 1648 (Oct, 1998).
122. J. M. Bekkers, G. B. Richerson, C. F. Stevens, Origin of variability in quantal size in cultured hippocampal neurons and hippocampal slices. *Proc Natl Acad Sci U S A* **87**, 5359 (Jul, 1990).
123. Y. V. Pankratov, O. A. Krishtal, Distinct quantal features of AMPA and NMDA synaptic currents in hippocampal neurons: implication of glutamate spillover and receptor saturation. *Biophys J* **85**, 3375 (Nov, 2003).
124. P. Jonas, G. Major, B. Sakmann, Quantal components of unitary EPSCs at the mossy fibre synapse on CA3 pyramidal cells of rat hippocampus. *J Physiol* **472**, 615 (Dec, 1993).
125. M. Matsuzaki *et al.*, Dendritic spine geometry is critical for AMPA receptor expression in hippocampal CA1 pyramidal neurons. *Nat Neurosci* **4**, 1086 (Nov, 2001).
126. S. R. Williams, G. J. Stuart, Dependence of EPSP efficacy on synapse location in neocortical pyramidal neurons. *Science* **295**, 1907 (Mar 8, 2002).
127. C. Koch, T. Poggio, A theoretical analysis of electrical properties of spines. *Proc R Soc Lond B Biol Sci* **218**, 455 (Jul 22, 1983).
128. W. Rall, Distributions of potential in cylindrical coordinates and time constants for a membrane cylinder. *Biophys J* **9**, 1509 (Dec, 1969).

129. M. Hausser, N. Spruston, G. J. Stuart, Diversity and dynamics of dendritic signaling. *Science* **290**, 739 (Oct 27, 2000).